

## Interfacial force measurements using atomic force microscopy

Chu, Liangyong

**DOI**

[10.4233/uuid:a4771e84-1f87-483f-8fce-c119df35b171](https://doi.org/10.4233/uuid:a4771e84-1f87-483f-8fce-c119df35b171)

**Publication date**

2017

**Document Version**

Final published version

**Citation (APA)**

Chu, L. (2017). *Interfacial force measurements using atomic force microscopy*. [Dissertation (TU Delft), Delft University of Technology]. <https://doi.org/10.4233/uuid:a4771e84-1f87-483f-8fce-c119df35b171>

**Important note**

To cite this publication, please use the final published version (if applicable).  
Please check the document version above.

**Copyright**

Other than for strictly personal use, it is not permitted to download, forward or distribute the text or part of it, without the consent of the author(s) and/or copyright holder(s), unless the work is under an open content license such as Creative Commons.

**Takedown policy**

Please contact us and provide details if you believe this document breaches copyrights.  
We will remove access to the work immediately and investigate your claim.

# **Interfacial force measurements using atomic force microscopy**

**Liangyong Chu**



# **Interfacial force measurements using atomic force microscopy**

Proefschrift

ter verkrijging van de graad van doctor  
aan de Technische Universiteit Delft,  
op gezag van de Rector Magnificus prof.dr.ir. T.H.J.J. van der Hagen,  
voorzitter van het College voor Promoties,  
in het openbaar te verdedigen op  
maandag 8 januari 2018 om 10.00 uur

door

**Liangyong CHU**

Master of Science in Physics, China University of Petroleum, China  
geboren te Shandong Province, China

This dissertation has been approved by the:

Promotor: Prof. Dr. E. J. R. Sudhölter and Prof. Dr. S. J. Picken

Composition of the doctoral committee:

Rector Magnificus	chairman
Prof. Dr. E. J. R. Sudhölter	Technische Universiteit Delft, promotor
Prof. Dr. S. J. Picken	Technische Universiteit Delft, promotor

Independent members:

Prof. Dr. U. Staufer	Technische Universiteit Delft
Prof. Dr. Ir. J. van der Gucht	Wageningen Universiteit en Research centrum
Prof. Dr. F. G. Mugele	Universiteit Twente in Enschede
Dr. E. Mendes	Technische Universiteit Delft
Prof. Dr. J. H. van Esch	Technische Universiteit Delft

The work described in this thesis was carried out in Organic Materials and Interfaces, Department of Chemical Engineering, Faculty of Applied Sciences, Delft University of Technology. The research was financed by China Scholarship Council (CSC).



ISBN: 978-94-6332-297-3

Cover designed by Liangyong Chu

Copyright © 2017 Liangyong Chu

All rights reserved. No part of the material protected by this copyright notice may be reproduced or utilized in any form or by any other means, electronic or mechanical, including photocopying, recording or by any information storage and retrieval system, without written permission from the author.

Printed in the Netherlands by GVO printers&designers B.V.

A digital copy is available at <http://repository.tudelft.nl>

*To my family*



# CONTENTS

<b>FUNDAMENTALS OF ATOMIC FORCE MICROSCOPY AND FORCE MEASUREMENTS</b>	<b>1</b>
1.1 FUNDAMENTALS OF ATOMIC FORCE MICROSCOPY	2
1.1.1 Structure of an AFM system	2
1.1.2 AFM working mode	4
1.2 NORMAL FORCE MEASUREMENTS USING AFM	5
1.3 LATERAL FORCE MEASUREMENT USING AFM	7
1.4 SCOPE AND OUTLINE OF THE THESIS	8
1.5 REFERENCES	9
<b>MIMICKING AN ATOMIC-THIN ‘VACUUM SPACER’ TO MEASURE THE HAMAKER CONSTANT BETWEEN GRAPHENE OXIDE AND SILICA</b>	<b>13</b>
2.1 INTRODUCTION	15
2.2 EXPERIMENTAL SECTION	16
2.2.1 Chemicals and materials	16
2.2.2 Sample preparation	17
2.2.3 Instrumentation and methods	17
2.3 RESULTS AND DISCUSSIONS	18
2.4 CONCLUSIONS	25
2.5 REFERENCES	25
SUPPORTING INFORMATION	28
<b>FAST AND CONTROLLED FABRICATION OF POROUS GRAPHENE OXIDE: APPLICATION OF AFM TAPPING FOR MECHANO-CHEMISTRY</b>	<b>43</b>
3.1 INTRODUCTION	45
3.2 EXPERIMENTAL SECTION	45
3.2.1 Chemicals and materials	45
3.2.2 Sample preparation	46
3.2.3 AFM imaging	47
3.3 FORMATION OF PORES DUE TO OXYGEN PLASMA	47
3.4 PORE-SIZE DISTRIBUTION	50
3.5 INFLUENCE OF THE PRESSURE OF OXYGEN PLASMA TREATMENT	52
3.6 DISCUSSION	58
3.7 CONCLUSIONS	61
3.8 REFERENCES	61



SUPPORTING INFORMATION	63
<b>CALIBRATING LATERAL FORCE MODE AFM AND MEASUREMENT OF THE LATERAL SPRING CONSTANT</b>	<b>79</b>
4.1 INTRODUCTION	81
4.2 MATERIALS AND METHODS	84
4.3 RESULTS AND DISCUSSIONS	84
4.4 CONCLUSIONS	88
4.5 REFERENCES	89
SUPPORTING INFORMATION	90
<b>AFM STUDY OF LUBRICATION OF GRAPHENE OXIDE BY WATER</b>	<b>103</b>
5.1 INTRODUCTION	105
5.2 EXPERIMENTAL SECTION	107
5.2.1 Chemicals and materials	107
5.2.2 Sample preparation	107
5.2.3 Instrumentation and methods	108
5.3 RESULTS AND DISCUSSIONS	108
5.4 CONCLUSIONS	114
5.5 REFERENCES	114
SUPPORTING INFORMATION	116
<b>ATOMIC ORIGIN OF THE ONSET OF SLIP OF FRICTIONAL MOTION AT SINGLE ASPERITY CONTACT</b>	<b>121</b>
6.1 INTRODUCTION	123
6.2 RESULTS AND DISCUSSIONS	124
6.2.1 Description of the continuous hold-relax-hold (HRH) SA experiments	124
2.2 Experimental results and analysis	126
6.3 CONCLUSION	134
6.4 MATERIALS AND METHODS	135
6.5 REFERENCES	135
SUMMARY	137
SAMENVATTING	139
ACKNOWLEDGEMENTS	143
CURRICULUM VITAE	145

LIST OF PUBLICATIONS

146



**Fundamentals of Atomic force  
microscopy and force  
measurements**

**1**

## 1.1 Fundamentals of Atomic force microscopy

Since 1980s, a series of scanning probe microscopes (SPM) has been developed for surface imaging.<sup>[1, 2]</sup> The key of these techniques is using a feedback loop to regulate the interfacial gap distance between probe and sample. The feedback loop works on various interfacial parameters which are relevant with interfacial distance, e.g. tunnel current, force, electric and magnetic fields.<sup>[1, 3, 4]</sup> Atomic force microscopy (AFM) is the one that is regulating the interaction force between a nanometer (nm) or micrometer ( $\mu\text{m}$ ) sized tip and the sample surface, thus realizing the imaging of the topography of surfaces at atomic resolution.<sup>[4]</sup> Moreover, using AFM, the interaction forces, including repulsive, adhesive and lateral forces, between an AFM tip and the sample surface can be measured. Based on AFM, various extended techniques have been developed such as colloidal probe AFM,<sup>[5]</sup> single molecule AFM,<sup>[6-11]</sup> bio-AFM,<sup>[12]</sup> Kelvin probe AFM<sup>[12, 13]</sup> and lateral force AFM (LFM).<sup>[14, 15]</sup> These make AFM a powerful tool to study the properties of surfaces and interfaces,<sup>[16]</sup> which are crucial for many disciplines, e.g. surface chemistry, polymer chemistry and physics, solid-state physics, cell biology and medicine.<sup>[10, 15, 17, 18]</sup>

### 1.1.1 Structure of an AFM system

As shown in Figure 1.1, the hardware of a typical AFM is composed by three main parts. The first part is a probe, composed by a cantilever and a tip at the end. The key element is the tip, which interacts with the sample surface during scanning. Various AFM probes with modified tips are fabricated for different applications and most of them are commercially available e.g. colloidal probe, Kelvin probe, diamond based probes. The backside of the cantilever is usually coated with a reflective layer. The second part is the laser system, as shown in Figure 1.1, the incoming laser light is reflected by the backside of the cantilever and is recorded by a position-sensitive photo detector (PSPD).<sup>[19]</sup> The bend and twist motions of the cantilever, as induced by the interactions with the scanned surface, are recorded by the current (or voltage) changes of the PSPD. As shown in Figure 1.1, the bend movement of the cantilever is proportional to the normal signal defined as  $I_n = (A + C) - (B + D)$ , while the twist movement of the cantilever is proportional to the lateral signal defined as  $I_x = (A + B) - (C + D)$ . The third part is the scanner, which can move in the x-

y-z directions. Obviously, the movement of the sample that is fixed on the scanner is equivalent to that of the scanner. The key element of the scanner is made of piezoelectric materials, which can expand with sub-nm resolution under the application of an electric field.<sup>[4]</sup>

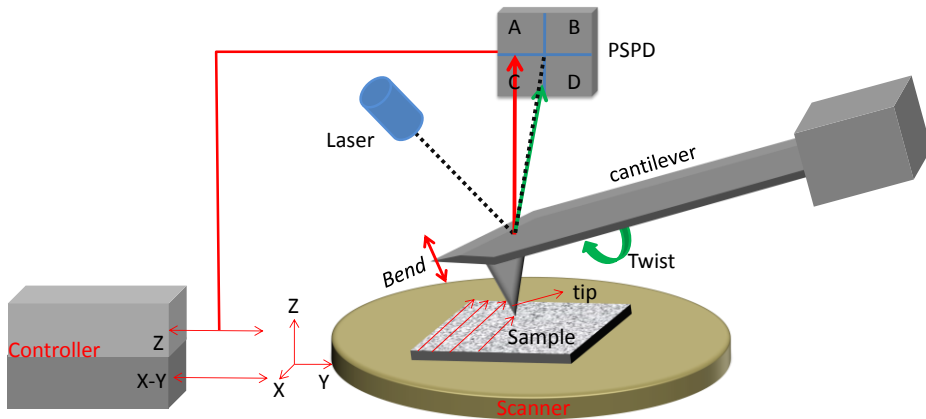


Figure 1.1 Schematic drawing of an AFM system. PSPD is the abbreviation of position-sensitive photo detector. The black dash line shows the laser path with no bend or twist. The cantilever bend and the change of the laser path is marked with red colour and the cantilever twist and the change of the laser path is marked with green colour.

In the AFM control system, the interaction force between tip and sample is used to sense the approaching movement of the sample towards the tip. During the scan, the scanner moves along an array of lines in the x-y plane while keeping the force between the tip and sample constant. This is realized by the z direction displacement of the sample as controlled by a feedback loop. Usually, a proportional–integral–derivative (PID) mechanism (controller) is used for the feedback loop.<sup>[20]</sup> The displacement of the scanner in z direction gives the height information of the sample surface. During the scan, the linearity of x-y direction displacement is crucial for the imaging quality. Nowadays, for most commercial AFM instruments, an independent capacitive position sensor is usually integrated with the scanner to detect the scanner displacement.<sup>[18]</sup> The linearity of the x-y displacement is realized by a closed loop controller, which can simultaneously correct the displacement of the scanner.

### 1.1.2 AFM working mode

There are two basic working modes for AFM, the contact mode and the semi-contact mode. In the contact mode (also called the static mode or repulsive mode), the tip of the probe is initially in contact with the sample surface, the applied force between the tip and sample is called the normal load force and is recorded by the change of the PSPD signal  $I_n$ . During the scan, the interaction force ( $\propto \Delta I_n$ ) is kept constant. This is realized by z direction displacement of the scanner as controlled by a feedback loop. Thus, the z direction displacement of the scanner describes the morphology of the sample. At contact mode, the tip also slides over the sample surface and the lateral signal  $I_x$  also varies. The friction force between the tip and sample under certain normal load force ( $\propto \Delta I_n$ ) is recorded and is proportional to the lateral signal change  $\Delta I_x$ . This is called the lateral mode signal.

In a semi-contact mode (also called the dynamic mode or tapping mode),<sup>[8]</sup> the cantilever is deliberately vibrating by a piezo mounted above it. When the tip is very close to the sample surface, the vibration amplitude or vibration frequency changes due to the very weak tip-sample interaction. During the scan, the vibration amplitude change or frequency shift is kept constant. This is also realized by z direction displacement of the scanner as controlled by a feedback loop. The z direction displacement of the scanner describes the morphology of the sample.

Based on these two basic modes, other modes are developed for various applications (complex study of polymers, electrical properties characterization and biological applications), *e.g.* HybriD mode (Pulsed force mode).<sup>[21]</sup> This method combines height imaging and tip-sample force tracking simultaneously. With HybriD mode AFM, a vertical oscillation of the sample is implemented at frequencies well below the resonances of the probe and the piezo-element in order to improve the signal to noise ratio. In the HybriD mode method, at each (x,y) point the tip performs a cycle of approaching and retracting. In the approaching movement, the tip goes from non-touching to the touching regime, and the deflection signal of the cantilever records the force that the tip experiences. In the retracting movement of the cycle, the tip experiences strong adhesive interactions as is reflected by a jump of the normal force signal as the tip detaches. This jump is proportional to the

magnitude of the adhesive force. As a result, besides the surface morphology height image, we also obtain the normal adhesion-force and stiffness images at the same time.

## 1.2 Normal force measurements using AFM

The core components of the probe are the cantilever and tip. Commercial probes are typically made of silicon or silicon nitride covered with a native oxide layer of 1-2 nm thickness. The mechanical parameters of the cantilever that we have to know for force measurement are the normal spring constant  $K_n$  and the resonance frequency  $\nu_0$ . These parameters can be calculated from the materials properties and the dimensions of the cantilever as shown in equation 1.1. <sup>[16, 22]</sup>

$$K_n = \frac{F}{Z_n} = \frac{Ewt_c^3}{4L^3}, \quad \nu_0 = 0.1615 \frac{t_c}{L^2} \quad (1.1)$$

Where  $F$  is the applied normal force (N),  $Z_n$  is the displacement of the tip due to the normal force (m),  $E$  is the Young's modulus (Pa),  $w$ ,  $t_c$  and  $L$  are the width, thickness and length of the cantilever (m), respectively, and  $\rho$  is the density of the cantilever material ( $\text{g/m}^3$ ).

It is found that experimentally determined spring constant differs significantly from the calculated ones. This is caused by the uncertainties of the cantilever thickness and inhomogeneous composition of the cantilever material which will affect the Young's modulus significantly. A more elegant and widely used method to determine the  $k_n$ , is by measuring the intensity of the thermal noise (the displacement of cantilever due to thermal fluctuations). When the cantilever is described as a harmonic oscillator, the mean square displacement of the cantilever due to the thermal fluctuations is given by<sup>[23]</sup>

$$\frac{1}{2} K_n \overline{\Delta x_t^2} = \frac{1}{2} k_B T \rightarrow K_n = \frac{k_B T}{\overline{\Delta x_t^2}} \quad (1.2)$$

So, when we know  $\overline{\Delta x_t^2}$  from a measurement of the (thermal) tip-position fluctuations, we also know the so far unknown spring constant  $K_n$ . As recognised by Hutter et al.,<sup>[7]</sup> thermal fluctuations are not the only factor that determines the tip displacement. Other factors, like instrument noise, also play a role.  $\overline{\Delta x_t^2}$  due to thermal fluctuations is best determined as the integral of the resonance peak in the power spectrum density (PSD), since the contributions of other factors have a different frequency. PSD shows the strength of the



variations (energy) as a function of frequency. Thus, the intergral of the PSD function equals to the driven energy. This method is used in most of the commercially available AFM instruments.

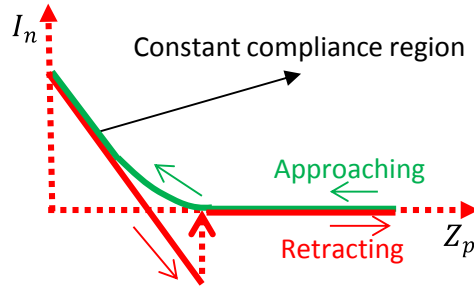


Figure 1.2 Typical curve of the PSPD current  $I_n$  versus height position of the piezoelectric scanner  $Z_p$ .

In the contact mode, the direct result of a force measurement is a curve of the PSPD current  $I_n$  versus height position of the piezoelectric scanner  $Z_p$ .<sup>[24]</sup> As shown in Figure 1.2, In the (green) approaching movement curve, before the tip and sample get into contact,  $I_n$  is constant (the horizontal line). After getting into contact, the tip starts to press the sample surface. The cantilever bends and also the sample surface deforms. At certain conditions, the sample deformation is maximal and the tip moves exactly the same as the scanner. This is called the constant compliance region. The red curve show the  $I_n$ , when the scanner retracts from the sample surface. Usually, a tip-sample jump is observed due to the mutual adhesive force between the two.

To obtain from these data a force-*versus*-distance curve,  $I_n$  has to be converted into force and  $Z_p$  has to be converted into the distance between the tip and sample surface. Therefore, two other parameters need to be known: the PSPD sensitivity and how to define the distance zero. Practically, the linear part of the constant compliance region is assumed to be zero distance and its slope is the PSPD sensitivity.

In the tapping mode, we can obtain qualitative information of the tip-sample interaction from the phase image that is simultaneously obtained with the height image.<sup>[6, 8]</sup> As shown in Figure 1.3, the cantilever is vibrating at its resonance frequency, when the tip approaches

and slightly touches the sample surface, the oscillation amplitude decreases and the feedback loop maintains this change to monitor the surface topology. At the same time, the phase of the oscillation changes compared to the driving oscillator as a result of the interaction between tip and sample surface. This phase change depends on the physical and chemical features of the contact region, *e.g.* stiffness, adhesion.

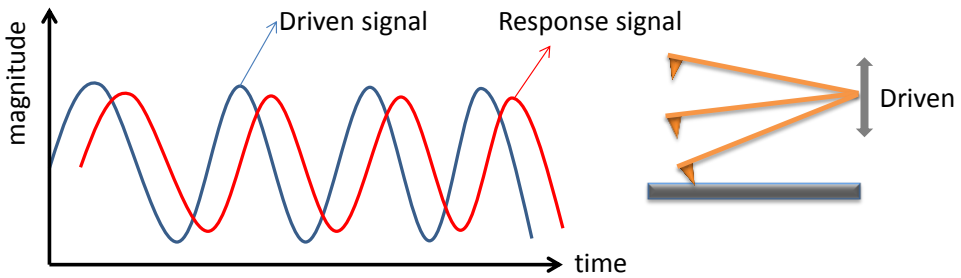


Figure 1.3 Phase response signal of the cantilever at the resonance frequency.

### 1.3 Lateral force measurement using AFM

In lateral force measurement, the AFM works in the contact mode with a certain chosen normal load force. The sample moves in the  $x$  direction and the tip slides over the sample surface. As a result we obtain a curve of the PSPD lateral signal  $I_x$  versus the scanner displacement  $\Delta_x$ . To derive the lateral force exerted between tip and sample at a certain position, we need to convert  $I_x$  into a friction force  $F_x$ . Obviously, the value of the friction force is equal to the force that twists the cantilever, with an opposite sign. To obtain the relation between lateral force  $F_x$  and  $I_x$ , we have to know additional two parameters. One is the so called lateral sensitivity ( $\sigma_x$ ), defined as the change of  $I_x$  per unit of cantilever twist (lateral displacement of the tip or twist angle). The other one is the lateral spring constant  $K_x$ , defined as the force that is needed to realize a unit of cantilever twist (corresponding to the definition of the sensitivity). As we will show in chapter 3, the conversion of the friction signal into the friction force is not as straightforward as it is in normal force calibration. The main reason is that in the lateral mode the force compliance region is not as clear defined compared to normal force measurement. <sup>[9, 12, 13, 25]</sup> Thus, the lateral force measurements using AFM is still not as good calibrated as for normal force measurements.

## 1.4 Scope and outline of the thesis

The work presented in this thesis describes normal and lateral mode AFM force measurements both on silicon and graphene oxide (GO) surfaces. Silicon surfaces with a native oxide layer are widely used model surfaces, due to its application in e.g. semiconductor industry. GO is an important 2D material, which has multi-faces and applications, e.g. surfactant, diblock copolymer, colloids.<sup>[26]</sup> The thesis is focused on the better understanding of the fundamental aspects of the interfacial interactions between these two materials.

The Hamaker constant between GO and silica, which describes the strength of the Van der Waals forces, is crucial for several applications, e.g. the fabrication of graphene based heterogenic structures. However, it is still not possible to determine the Hamaker constant due to several difficulties, including the precise control of the mutual separation distance and the elimination of other contributions, like capillary forces and electrostatic forces. In **Chapter 2**, we describe a new method to determine the Hamaker constant between GO and silica using AFM normal force measurements, solving the difficulties mentioned above.

Semi-contact mode AFM imaging is always assumed to have no influence on the investigated surfaces, in comparison with contact mode AFM. However, in **Chapter 3**, we will prove that it may not be always the case. Our experimental results show that semi-contact mode AFM imaging does influence the chemical composition/structure of oxygen-plasma exposed porous GO. This also lead to a new controlled way to fabricate 2D porous networks by applying AFM tapping.

A problem with lateral mode AFM (LFM), as opposed to normal mode AFM, is that LFM is not readily calibrated. This hampers the measurement of accurate absolute values for the lateral forces. In **Chapter 4**, a novel method is proposed and demonstrated to determine the lateral spring constant and to calibrate the LFM. It does not involve any damage or modification of the AFM probe, and works on typical commercially available AFM systems. We are convinced that this method will be very helpful for all those involved in this field of expertise.

Lubrication by water molecules is becoming of increasing important by its relevance in bio-nanoscience. To realize effective boundary lubrication by water, the surface needs to be atomically flat and hydrophilic and this is only reported for mica surfaces and for self-assembling surfactant layers. In **Chapter 5**, results will be described from lateral force experiments and demonstrate that GO surfaces can be effectively lubricated by only a few layers of water molecules. This may lead most likely to new applications of GO.

The onset of slip of frictional motion can be found in everyday processes and is dominant for proper fundamental understandings in various fields, e.g. earthquakes. Recent investigations show that at a macroscale contact, this slip can be described by a rupture mechanism, since a macroscale contact can be regarded as multiple contacts of single asperity contacts. In **Chapter 6**, results will show what happens at the onset of a SA contact frictional motion. This will help to understand the fundamentals of dynamics of the slip at atomic scale.

## **1.5 References**

- [1] G. Binnig, H. Rohrer, *Surface science* 1983, 126, 236.
- [2] R. Wiesendanger, *Scanning probe microscopy and spectroscopy: methods and applications*, Cambridge University Press, 1994.
- [3] U. Hartmann, *Annual Review of Materials Science* 1999, 29, 53; D. Rugar, H. Mamin, P. Guethner, S. Lambert, J. Stern, I. McFadyen, T. Yogi, *J. Appl. Phys.* 1990, 68, 1169.
- [4] G. Binnig, C. F. Quate, C. Gerber, *Physical review letters* 1986, 56, 930.
- [5] W. A. Ducker, T. J. Senden, R. M. Pashley, *Nature* 1991, 353, 239.
- [6] J. Cleveland, B. Anczykowski, A. Schmid, V. Elings, *Applied Physics Letters* 1998, 72, 2613.
- [7] J. L. Hutter, J. Bechhoefer, *Review of Scientific Instruments* 1993, 64, 1868.
- [8] S. Magonov, V. Elings, M.-H. Whangbo, *Surface science* 1997, 375, L385.
- [9] A. Feiler, P. Attard, I. Larson, *Review of scientific instruments* 2000, 71, 2746.
- [10] M. Rief, F. Oesterhelt, B. Heymann, H. E. Gaub, *Science* 1997, 275, 1295.
- [11] H. Li, M. Rief, F. Oesterhelt, H. E. Gaub, *Advanced Materials* 1998, 10, 316; F. Oesterhelt, M. Rief, H. Gaub, *New Journal of Physics* 1999, 1, 6; T. Hugel, N. B. Holland,

- A. Cattani, L. Moroder, M. Seitz, H. E. Gaub, *Science* 2002, 296, 1103; A. F. Oberhauser, C. Badilla-Fernandez, M. Carrion-Vazquez, J. M. Fernandez, *Journal of molecular biology* 2002, 319, 433.
- [12] C. P. Green, H. Lioe, J. P. Cleveland, R. Proksch, P. Mulvaney, J. E. Sader, *Review of Scientific Instruments* 2004, 75, 1988.
- [13] G. Meyer, N. M. Amer, *Applied physics letters* 1990, 57, 2089.
- [14] F. W. DelRio, M. P. de Boer, J. A. Knapp, E. D. Reedy, P. J. Clews, M. L. Dunn, *Nature materials* 2005, 4, 629; C. Li, T.-W. Chou, *Composites Science and Technology* 2003, 63, 1517.
- [15] H.-J. Butt, *Biophysical Journal* 1991, 60, 1438.
- [16] H.-J. Butt, B. Cappella, M. Kappl, *Surface science reports* 2005, 59, 1.
- [17] Q. Zhong, D. Inniss, K. Kjoller, V. Elings, *Surface science* 1993, 290, L688; B. Drake, C. Prater, A. Weisenhorn, S. Gould, T. Albrecht, *Science* 1989, 243, 1586; E. Henderson, P. Haydon, D. Sakaguchi, *Science* 1992, 257, 1944; P. Hinterdorfer, Y. F. Dufrêne, *Nature methods* 2006, 3, 347; W. A. Ducker, T. J. Senden, R. M. Pashley, *Langmuir* 1992, 8, 1831; C. D. Frisbie, L. F. Rozsnyai, A. Noy, M. S. Wrighton, C. M. Lieber, *SCIENCE-NEW YORK THEN WASHINGTON-* 1994, 2071; A. Milling, S. Biggs, *Journal of colloid and interface science* 1995, 170, 604; C. Argento, R. French, *J. Appl. Phys.* 1996, 80, 6081; A. Noy, D. V. Vezenov, C. M. Lieber, *Annual Review of Materials Science* 1997, 27, 381; S. S. Wong, A. T. Woolley, E. Joselevich, C. L. Cheung, C. M. Lieber, *Journal of the American Chemical Society* 1998, 120, 8557; J. A. Brant, A. E. Childress, *Environmental Engineering Science* 2002, 19, 413; M. Giesbers, J. M. Kleijn, M. A. C. Stuart, *Journal of colloid and interface science* 2002, 248, 88; Y. Gan, G. V. Franks, *Langmuir* 2006, 22, 6087; W. Knoben, N. Besseling, M. C. Stuart, *Physical review letters* 2006, 97, 068301.
- [18] S. Biggs, *Langmuir* 1995, 11, 156.
- [19] G. Meyer, N. M. Amer, *Applied physics letters* 1988, 53, 1045.
- [20] K. J. Åström, T. Hägglund, *Advanced PID control*, ISA-The Instrumentation, Systems and Automation Society, 2006.
- [21] L. Chu, A. V. Korobko, A. Cao, S. Sachdeva, Z. Liu, L. C. de Smet, E. J. R. Sudhölter, S. J. Picken, N. A. Besseling, *Advanced Materials Interfaces* 2017, 4.

- [22] G. Chen, R. Warmack, T. Thundat, D. Allison, A. Huang, *Review of Scientific Instruments* 1994, 65, 2532; J. E. Sader, J. W. Chon, P. Mulvaney, *Review of Scientific Instruments* 1999, 70, 3967.
- [23] H.-J. Butt, M. Jaschke, *Nanotechnology* 1995, 6, 1.
- [24] B. Cappella, G. Dietler, *Surface science reports* 1999, 34, 15.
- [25] NT-MDT; R. J. Cannara, M. Eglin, R. W. Carpick, *Review of Scientific Instruments* 2006, 77, 053701; J. M. Neumeister, W. A. Ducker, *Review of Scientific Instruments* 1994, 65, 2527.
- [26] J. Kim, L. J. Cote, J. Huang, *Accounts of Chemical Research* 2012, 45, 1356.



# Mimicking an Atomic-thin ‘Vacuum Spacer’ to Measure the Hamaker Constant between Graphene Oxide and Silica

# 2

---

The contents of this chapter have been published in:

Chu, L.; Korobko, A. V.; Cao, A.; Sachdeva, S.; Liu, Z.; de Smet, L. C.; Sudhölter, E. J.; Picken, S. J.; Besseling, N. A., Mimicking an Atomically Thin “Vacuum Spacer” to Measure the Hamaker Constant between Graphene Oxide and Silica. *Advanced Materials Interfaces* 2017, 4, 1600495.



## Abstract

In this chapter, the Hamaker constant between graphene oxide and silica, which quantifies the strength of the Van der Waals forces is determined, by mimicking a ‘vacuum spacer’ in an AFM force study. It is demonstrated that a graphene oxide (GO) 2D spacer yields an accurately defined separation compared with other dimensional spacers. This is due to the high atom density and mechanical strength in the planar direction. .

## 2.1 Introduction

In nanoscience, control of the separation between surfaces, with sub-nm accuracy, is often important. For instance, when studying Van der Waals (VdW) forces<sup>[1]</sup> or creating nanogaps for molecular detection and separation<sup>[2]</sup>. At nanometer scales, 1D or 3D spacers, such as nanotubes and nano-particles, are susceptible to shape deformation<sup>[3]</sup>. A 2D spacer is expected to yield a more accurately defined separation, owing to the high atom density and mechanical strength in planar direction. Herein, atomically thin 2D graphene oxide (GO) was used as a nanometer-scale spacer with sub-nm accuracy, to study VdW interactions. However, using such a physical spacer introduces additional interactions, obscuring the interactions of interest. We demonstrate how these contributions can be eliminated by effectively mimicking the use of a ‘vacuum spacer’. In this way, we obtain the effective Hamaker constant between GO and silica.

Following the excitement about graphene, GO is drawing more and more attention.<sup>[4]</sup> Using GO as a precursor, many graphene derivatives and heterostructures<sup>[1]</sup> have been made, and used in various areas such as composites,<sup>[5]</sup> energy storage and conversion,<sup>[6]</sup> bioscience, mechanical and electronic devices and sensors.<sup>[7]</sup>

In all these applications, graphene-based materials are used in combination with other materials. Hence, the relevance of interfacial forces such as VdW<sup>[1, 8]</sup>, capillary<sup>[9]</sup> and electrostatic<sup>[10]</sup> forces. The VdW forces, which are always present, can be quantified by the so-called Hamaker constant.<sup>[11]</sup> The VdW interaction energy  $U_{\text{VdW}}(d)$  between two material surfaces is<sup>[11, 12]</sup>

$$U_{\text{VdW}}(d) = -A_{12}/12\pi d^2 \quad (1)$$

where  $d$  is the separation distance, and  $A_{12}$  is the Hamaker constant.

Knowing the Hamaker constant between graphene-based materials and other materials (e.g. silicon (Si) with a native silicon oxide layer as used in electronic devices) is important for their application. However, the experimental determination of this constant is still challenging. According to Equation 1, to determine the Hamaker constant, the VdW interaction energy ( $U_{\text{VdW}}$ ) needs to be determined for a known separation distance ( $d$ ). Several investigations have been made to establish the strength of VdW interactions between graphene and Si by measuring the adhesion energy.<sup>[13]</sup> However, the effective distance between a graphene sheet and a Si surface could not be precisely determined in

these experiments. The effective separation distance of two ‘touching’ surfaces varies from one to two Ångstroms depending on the surface roughness.<sup>[14]</sup> At small separation distances, the limited accuracy of the distance measurement (typical error of  $\pm 1$  nm) leads to a huge error in the calculated value of the Hamaker constant. In principle, this problem could be solved by a spacer with a precisely known thickness of about 1 nm. At such distances, the magnitude of the VdW energy is sufficient for accurate measurement, and the retardation effect is unimportant.<sup>[15]</sup> Note: Considering the electromagnetic nature of the VdW interaction, the propagation interaction between two bodies needs a finite time. This retardation becomes more important when the separation is larger than a few nanometers. The ideal spacer would be one that ‘consists of vacuum’, so that it would not contribute to the interactions.

Capillary<sup>[9]</sup> and electrostatic<sup>[10]</sup> forces complicate determination of the VdW energy even further.

## 2.2 Experimental Section

### 2.2.1 Chemicals and materials

Graphene oxide (GO), synthesized using Hummer’s method, was purchased from Graphene Supermarket. The elemental composition of GO was characterized using X-ray photoelectron spectroscopy (XPS) (supporting information 5). A stable dispersion of 0.5 g GO in 1 L Milli-Q water was prepared using ultrasonication for 1 h, using an USC-TH ultrasonic bath from VWR Scientific. The dispersion was then centrifugation at 4000 rpm for 1 h, using a Megafuge 2.0R centrifuge from Heraeus Instruments with rotor radius of 20 cm. The supernatant was decanted and used for the sample preparation. Polyethylenimine (PEI,  $M_w = 25000$  g/mol) was purchased from Sigma-Aldrich and used as received. A 0.1 g/L PEI aqueous solution was prepared using milli-Q water. A chip of about of 1 cm  $\times$  1 cm was cut from a (100) Silicon wafer with a native oxide layer of about 2 nm obtained from Sil’Tronix Silicon Technologies. The silicon chip was first rinsed with demi-water and ethanol followed by sonication using ethanol and acetone for 5 min., respectively. Plasma treatments of samples were performed with oxygen plasma for 1 min. at a pressure of 1600 mTorr (2.1 mbar) using a Harrick plasma cleaner (Anadis Instruments). After plasma treatment, the silicon wafer was stored in milli-Q water for more than 24 h. to equilibrate.

### 2.2.2 Sample preparation

The Si surface was coated with a monolayer of Polyethylenimine (PEI) by dipping the Si chip in an aqueous PEI solution (0.1 g/L) for 15 min. The sample was then rinsed in milli-Q water for 5 min to remove non-adsorbed PEI. Subsequent coating by GO was done by immersing the sample for 15 min in the aqueous GO dispersion prepared as described above. To remove excess of GO, the sample was dipped in milli-Q water for 5 min. Due to present carboxylate groups, GO is negatively charged and adsorbs on the positively charged PEI layer. All these steps in the sample preparation were done while the solution was stirred.

After deposition, a Scotch tape treatment was performed. The tape was pressed onto the sample using a finger as shown in inset of Figure 2.2b, and then torn off. To remove the polymer (PEI and/or residue of the tape treatment, the sample was treated with oxygen plasma for 1 min. This completes the sample preparation.

### 2.2.3 Instrumentation and methods

A NTEGRA AFM instrument from NT-MDT was used in all AFM experiments. High sensitivity measurements were performed using the ‘HybriD Mode’ method, developed and implemented by NT-MDT. This method combines height imaging and tip-sample force tracking simultaneously.<sup>29</sup> With hybrid mode AFM, a vertical oscillation of the sample is implemented at frequencies well below the resonances of the probe and the piezo-element to improve the signal to noise ratio. In the HybriD Mode method, at each point the tip performs a cycle of approaching and retracting. The range of approaching and retracting was set at 20 nm. In the approaching phase, the tip goes from non-touching to the touching regime, and the deflection signal of the cantilever records the force that the tip experiences. In the retracting phase of the cycle, the tip experiences strong adhesive interactions reflected by a jump by which the tip detaches. The latter jump is proportional to the magnitude of the adhesive force  $F$ . As a result, we obtain the surface topology height image as well as the normalized adhesion-force image at the same time.

A NSG 03 silicon tip purchased from NT-MDT, with a nominal value for the tip radius of 7 nm (guaranteed < 10 nm) and a nominal spring constant of  $k_n = 0.4 - 2.7$  N/m was used with the hybrid mode measurements. Using high-resolution Scanning Electron Microscopy

(SEM), we determined that the tip radius equals to 10.6 nm (supporting information 6). The actual value of the spring constant was measured using the thermal noise method.<sup>30</sup> Scanning the surface topology, 512 x 512 points are recorded in a 4  $\mu\text{m}$  x 4  $\mu\text{m}$  area. HA\_NC AFM probes from NT-MDT with a silicon tip radii of about 10 nm were used for the standard tapping mode height scanning. The HybriD Mode images and standard tapping mode height images were all scanned with a rate of 0.5 Hz.

### 2.3 Results and discussions

Figure 2.1 illustrates the experiment that mimics the application of a vacuum spacer in an AFM force measurement, by measuring the adhesion force between an AFM tip and both mono- and bi- layers of GO on a Si/polymer substrate. From the difference between the measured adhesion force on GO monolayer and on GO bilayer (Figure 2.1.a, b respectively), capillary and electrostatic forces, and the VdW interactions between tip and underlying substrate cancel. Hence, we obtain the interaction force between a levitating GO nanosheet and the AFM tip, at a distance  $d$  corresponding to the thickness of the GO top layer, as if they were separated by a vacuum spacer with a thickness equal to that of the intervening GO top layer.

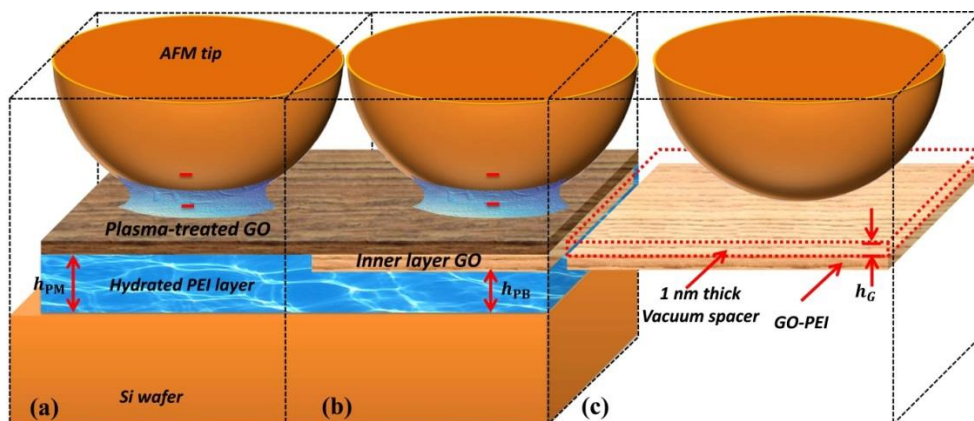


**Figure 2.1.** Schematic illustration of the performed experiment. (a) A silicon AFM tip in contact with Si wafer/PEI/GO monolayer. (b) A silicon AFM tip in contact with Si wafer /PEI/GO bilayer. The measured adhesion forces between the Si tip and the Si/PEI/GO layer in (a) and (b) are due to VdW forces, capillary forces, electrostatic forces and specific

interactions between chemical moieties such as hydrogen bonds. (c) The difference between situation (a) and (b) mimics the AFM tip interacting with a GO monolayer in vacuum at a distance  $d$ , equal to the thickness of a GO monolayer. The aqueous water bridge between AFM tip and plasma-treated GO is due to the hydrophilicity of the sample surface. Capillary, electrostatic, and other forces cancel out.

Sample preparation and morphology of the Si/PEI/GO structures depicted in Figure 2.1.a and b are summarised and illustrated in Figure 2.2, and described in the sample preparation part.

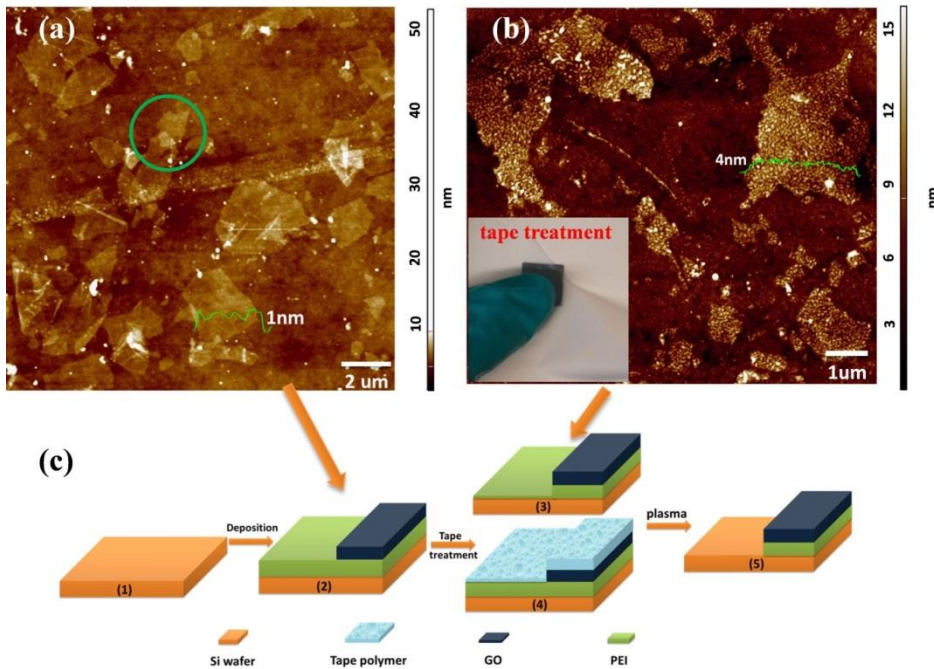


**Figure 2.2** (a) AFM height images of GO deposited on a Si/PEI surface. (b) AFM height images of the Si/PEI/GO sample after tape treatment. The inset of 2.b shows the sample being pressed on the tape. (c) Schematic illustration of the sample preparation. The tape polymer is only the adhesive part of the tape.

As shown in Figure 2.2a, GO flakes are clearly visible with thickness of about 1 nm, <sup>[28]</sup> as well as areas exhibiting a 2-fold increase of the height. The latter is interpreted as two GO nanosheets overlapping (indicated by the green circle). Clearly, GO flakes have remained at

the sample after tape treatment. Their height increased to 4 nm, the heights for monolayer and bilayer sections are now the same, this is observed from the AFM height morphology of the sample and is probably due to the pulling force of the tap applied on the surface. Furthermore, the surface roughness has increased. There are two possible explanations for the increased height of the GO-covered regions: (i) the tape/PEI interaction, as illustrated in Figure 2.2.c.3, is so strong that (part of) the PEI next to GO flakes was removed by the tape, and the tape/GO interaction is so much weaker that GO and PEI covered by it were not removed; and (ii) the (c.4) polymer adhesive molecules from the tape were left behind, and their quantity on GO was larger than that on PEI (see Figure 2.2.c.4). After plasma treatment, the sample has flakes of GO with PEI underneath on Si. The area not covered by GO is simply bare Si, as illustrated in Figure 2.2.c.5) The plasma treatment is expected to remove both the PEI and possibly present adhesive molecules, resulting in the same situation as indicated in Figure 2.2.c.5.

The surface morphology of the Si/PEI/GO sample as drawn in Figure 2.c.5, was characterized using Hybrid Mode AFM, <sup>[29]</sup> by which we obtain simultaneously a height image and an adhesive-force image (for details see Section 2.2.3, the instrumentation and methods part). In Figure 2.3 the results collected at different locations of the same sample are shown. Height images are depicted in Figure 2.3.a and d. GO flakes are identified by their larger height, by about 5 nm, relative to the silicon. This 5 nm represents the combined thickness of GO and underlying PEI. Features in the adhesion-force image coincide with features in the height counterpart. However, inspection of the adhesion-force image reveals features not visible in the height image. Folding and overlapping of GO, which forms a bilayer at some places, causes variations of the adhesion force. In adhesion-force images (Figure 2.3.b, 2.e) and profiles (Figure 2.3.c, 3.f) we recognise two distinct levels at the GO flakes. In Figure 2.3.d and 2.3.e we observe a straight edge, quite different from other more irregular edges of the GO flakes, which represents a fold of a flake. Adjoining this edge there must be a GO bilayer. Indeed, in the adhesion-force image (Figure 2.3e), and profile (Figure 2.3.f), we clearly recognise the bilayer patch adjoining this fold. The bilayer is characterised by a larger adhesive energy than the monolayer patches. Also in other places (e.g. image 2.3. e and profile 2.3. f) we recognise patches with this higher-level adhesive force. After the tape treatment, the sample surface is more rough and the height difference between mono- and bilayer GO becomes invisible(see supporting information part 3).

Figure 2.3.c and f represent typical single scan profiles along the white lines in Figure 2.3.a, 2.3.b and 2.3.d, 3e respectively. In Figure 2.3, S marks bare Si, M marks PEI/monolayer GO on Si wafer, and B marks PEI/bilayer GO on Si wafer. Values of normalised adhesion forces averaged over 5 points at a GO monolayer and at a bilayer are  $F_M/R = 76 \pm 3 \text{ mN/m}$  and  $F_B/R = 151 \pm 4 \text{ mN/m}$ , respectively, and the difference between these normalized forces is  $75 \pm 5 \text{ mN/m}$ . The results shown in Figure 2.3.d-f were obtained on another day, when temperature and humidity were somewhat different. Values  $F_M/R = 63 \pm 2 \text{ mN/m}$  and  $F_B/R = 136 \pm 3 \text{ mN/m}$  are quite different from the ones mentioned before, but the difference between these is the same within experimental accuracy ( $73 \pm 4 \text{ mN/m}$ ). The straight edge, indicated by the red circles represent a fold of the GO flake.



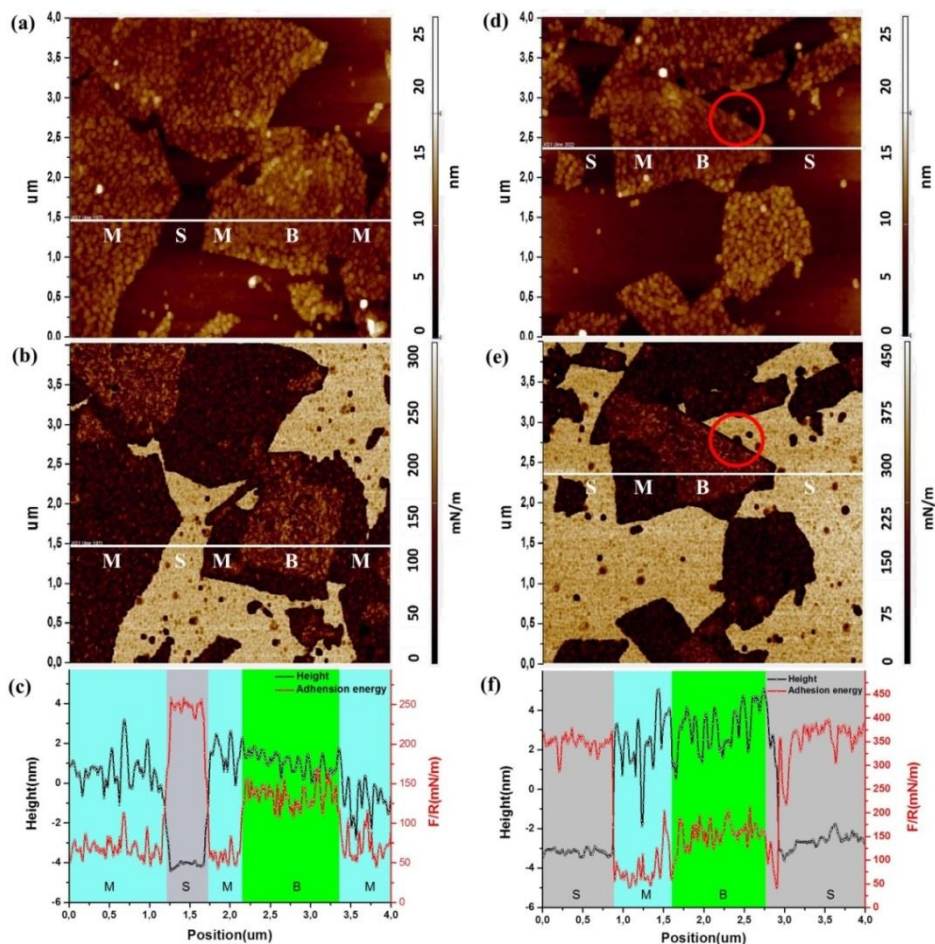


**Figure 2.3.** Surface morphology and adhesion-force images and profiles of Si/PEI/GO samples with a structure as illustrated in Fig. 2.2.5, obtained using HybriD Mode AFM. (a) Height image. (b) Normalized adhesion-force image of the same area. (c) Height and normalized adhesion-force profiles along the white line indicated in (a) and (b). (d) to (f) show the results of a repeated experiment at a different location of the same sample using the same AFM tip.

According to the Derjaguin approximation<sup>[16]</sup>, the interaction force  $F$  between a spherical surface of radius  $R$  (e.g. the AFM tip) and a flat surface (e.g. the Si/PEI/GO surface) is related to the interaction energy per unit area  $U$  between two planar surfaces via

$$\frac{F}{R} = 2\pi U \quad (2)$$

This relation applies to the VdW interactions and screened electrostatic interactions when the distance between the surfaces is considerably smaller than the radius  $R$ . It does not apply to interactions associated with capillary bridges. According to the Hamaker-de Boer approximation,<sup>[11, 17]</sup> the VdW interaction energy per unit area between a planar silica surface and a Si/PEI/GO surface at a distance  $D$ , with a GO thickness  $h_G$  and a PEI thickness  $h_p$ , is described by:

$$U_{\text{VdW}}(D, h_G, h_p) = -\left[ \frac{A_{\text{SG}}}{12\pi} \left( \frac{1}{D^2} - \frac{1}{(D + h_G)^2} \right) + \frac{A_{\text{SP}}}{12\pi} \left( \frac{1}{(D + h_G)^2} - \frac{1}{(D + h_G + h_p)^2} \right) + \frac{A_{\text{SSi}}}{12\pi} \left( \frac{1}{(D + h_G + h_p)^2} \right) \right] \quad (3)$$

where  $A_{\text{SG}}$ ,  $A_{\text{SP}}$ ,  $A_{\text{SSi}}$  are the Hamaker constants of Silica/GO, Silica/PEI and Silica/Si, respectively (see also supporting information, part 1).

The capillary force  $F_c$  ( $\frac{F_c}{R} \approx \sigma$ , the surface tension of water)<sup>[18]</sup> has a similar order of magnitude as the measured normalized force. However, its exact value is difficult to establish as it depends on humidity and the local surface morphology. Furthermore, the electrostatic force depends on the physical and chemical properties of the surface such as the surface charge densities, which are not known.

Assuming additivity rules, that all these forces can be added, the measured normalized force  $F/R$  is

$$F/R = 2\pi U_{\text{VdW}}(D, h_G, h_p) + F_c/R + F_e/R \quad (4)$$

where  $F_c$  and  $F_e$  represent the capillary and electrostatic forces, respectively.

It is not possible to obtain the Hamaker constant  $A_{\text{SG}}$  using separate values for  $F_M/R$  or for  $F_B/R$  as reported in Figure 2.3, because there are four unknown variables ( $A_{\text{SG}}$ ,  $D$ ,  $F_c$ ,  $F_e$ ). In order to obtain the Hamaker constant, the capillary and electrostatic forces have to be eliminated from analysis. Making some reasonable assumptions, it is possible to obtain the Hamaker constant from the difference between  $F_M/R$  and  $F_B/R$ . These assumptions are the additivity principle (Equation 4), and the assumption that the electrostatic and capillary forces are the same for GO monolayers and GO bilayers. This is reasonable as these contributions are largely determined by the nature of the outer surface, which is the same

for GO mono and bilayers. The capillary force  $F_c$  in AFM force measurement can be described as,<sup>[19]</sup>

$F_c = 2\pi\gamma R(\cos\theta_1 + \cos\theta_2)$ , where  $\gamma$  is surface tension of water,  $R$  is the radius of the AFM tip,  $\theta_1$  is the contact angle of AFM tip (silica),  $\theta_2$  is the contact angle of sample surface. In our case,  $\gamma$ ,  $R$ ,  $\theta_1$  can be regarded as constant, for monolayer and folded bilayer area.  $\theta_2$  can be different. As the tip and sample surface are all treated with oxygen plasma,  $\theta_1$  and  $\theta_2$  are all very small (close to zero, for plasma treated silica<sup>[20]</sup>). Thus, the folded underlayer has very limited effect on the water contact angle as well as the capillary force. For instance, contact angle decrease from 20 degree to 0 degree, on hydrophilic graphene oxide surface, only lead to about 3% change of capillary force.

The plasma treatment of the GO surfaces will probably induce some changes. However, this does not influence our final result, as the upper layer does not contribute to the final results and acts as a protecting layer for the second layer during the plasma treatment.

According to these assumptions, the normalised force for a levitating GO nanosheet positioned below the AFM tip at a distance  $d$  corresponding to the thickness of the GO top layer, equals to:

$$\begin{aligned} F_B/R - F_M/R &= [2\pi U(D, 2h_G, h_{PB}) + F_{B,c} + F_{B,e}] - [2\pi U(D, h_G, h_{PM}) + F_{M,c} + F_{M,e}] \\ &= \frac{A_{SG}-A_{SP}}{6} \left( \frac{1}{h_G^2} - \frac{1}{(2h_G)^2} \right) \\ &= \frac{1}{8} \frac{A_{SG}-A_{SP}}{d^2} \end{aligned} \quad (5)$$

Here, the separation distance  $d$  is equal to  $h_G$ . The second equality assumes that capillary and electrostatic forces are the same for the GO mono- and bilayer, so that these cancel. This relation enables us to calculate  $A_{SG}$  from the force difference, once  $R$ ,  $d$  and  $A_{SP}$  are known.

The value for  $d = h_G$  is  $0.89 \pm 0.06 \text{ nm}$  (see supporting information part 4). The radius  $R$  of the AFM tip is  $10.6 \text{ nm}$  (see supporting information part 6). To estimate  $A_{SP}$  we refer to Berthelot principle<sup>[16]</sup>

$$A_{SP} \approx (A_{SS}A_{PP})^{1/2} \quad (6)$$

For polymers such as e.g. PEI, the Hamaker constant is smaller than  $16 k_B T$ , that of water is  $10 k_B T$ . Thus, for  $A_{PP}$  the Hamaker constant of the hydrated PEI/PEI layer we use the

value  $13 \pm 3 k_B T$ .<sup>[16]</sup>  $A_{SS}$ , the Hamaker constant of Silica/Silica equals  $16.09 k_B T$ .<sup>[21]</sup> All Hamaker constants are expressed in units of  $k_B T$  at room temperature ( $= 4.07 \times 10^{-21} J$ ). Using the measured value for the force difference of  $75 \pm 5 mN/m$  (see Figure 2.3 and supporting information part 3), equations (5) and (6) yield the value of the Hamaker constant of GO/Silica of  $124.6 \pm 16.6 k_B T$  (supporting information part 7). This result is well reproduced when choosing different locations on the sample and when doing the experiment at different temperature and humidity as demonstrated in Figure 2.3(d-f).

## 2.4 Conclusions

In this chapter, on one hand, we found that 2D materials can be used as a nanometre-scale spacer, with sub-nm accuracy. On the other hand, we demonstrated that it is possible to mimick a ‘vacuum spacer’. This leads to an accurate determination of the Hamaker constant between GO and silica, which is crucial to many GO based applications. The measured Hamaker constant is slightly larger than that of graphite, this is reasonable due to the presence of the high polar groups on GO. This ‘vacuum-spacer method’, that was in this paper applied to GO, can in principle be applied to other 2D materials as well. We believe that this will open new applications of 2D materials in nanoscience and nanotechnology.

## 2.5 References

- [1] A. K. Geim, I. V. Grigorieva, *Nature* 2013, 499, 419.
- [2] D. R. Ward, N. K. Grady, C. S. Levin, N. J. Halas, Y. Wu, P. Nordlander, D. Natelson, *Nano letters* 2007, 7, 1396; D.-K. Lim, K.-S. Jeon, H. M. Kim, J.-M. Nam, Y. D. Suh, *Nature materials* 2010, 9, 60; H. Li, Z. Song, X. Zhang, Y. Huang, S. Li, Y. Mao, H. J. Ploehn, Y. Bao, M. Yu, *Science* 2013, 342, 95.
- [3] J. Sun, L. He, Y.-C. Lo, T. Xu, H. Bi, L. Sun, Z. Zhang, S. X. Mao, J. Li, *Nature materials* 2014, 13, 1007.

- [4] K. S. Novoselov, A. K. Geim, S. Morozov, D. Jiang, Y. Zhang, S. Dubonos, I. Grigorieva, A. Firsov, *Science* 2004, 306, 666.
- [5] S. Stankovich, D. A. Dikin, G. H. Dommett, K. M. Kohlhaas, E. J. Zimney, E. A. Stach, R. D. Piner, S. T. Nguyen, R. S. Ruoff, *Nature* 2006, 442, 282; T. Ramanathan, A. Abdala, S. Stankovich, D. Dikin, M. Herrera-Alonso, R. Piner, D. Adamson, H. Schniepp, X. Chen, R. Ruoff, *Nature nanotechnology* 2008, 3, 327; T. Kuilla, S. Bhadra, D. Yao, N. H. Kim, S. Bose, J. H. Lee, *Progress in polymer science* 2010, 35, 1350.
- [6] G. Eda, G. Fanchini, M. Chhowalla, *Nature nanotechnology* 2008, 3, 270.
- [7] A. Das, S. Pisana, B. Chakraborty, S. Piscanec, S. Saha, U. Waghmare, K. Novoselov, H. Krishnamurthy, A. Geim, A. Ferrari, *Nature nanotechnology* 2008, 3, 210; F. Schedin, A. Geim, S. Morozov, E. Hill, P. Blake, M. Katsnelson, K. Novoselov, *Nature materials* 2007, 6, 652.
- [8] S. F. Shi, F. Wang, *Nature Nanotechnology* 2014, 9, 664.
- [9] Y. Li, Y. Wu, *Journal of the American Chemical Society* 2009, 131, 5851.
- [10] D. R. Dreyer, S. Park, C. W. Bielawski, R. S. Ruoff, *Chemical Society Reviews* 2010, 39, 228.
- [11] H. Hamaker, *Physica* 1937, 4, 1058.
- [12] J. Visser, *Advances in Colloid and Interface Science* 1972, 3, 331.
- [13] S. P. Koenig, N. G. Boddeti, M. L. Dunn, J. S. Bunch, *Nature nanotechnology*, 6, 543; S. R. Na, J. W. Suk, R. S. Ruoff, R. Huang, K. M. Liechti, *Acs Nano* 2014, 8, 11234.
- [14] J. Rafiee, X. Mi, H. Gullapalli, A. V. Thomas, F. Yavari, Y. Shi, P. M. Ajayan, N. A. Koratkar, *Nature Materials* 2012, 11, 217.
- [15] J. Gregory, *Journal of Colloid and Interface Science* 1981, 83, 138.
- [16] J. Lyklema, 1991.
- [17] H. Hamaker, *Recueil des travaux chimiques des pays-bas* 1936, 55, 1015; H. Hamaker, *Recueil des travaux chimiques des pays-bas* 1937, 56, 3; J. De Boer, *Transactions of the Faraday Society* 1936, 32, 10.
- [18] S. Saito, T. Motokado, K. J. Obata, K. Takahashi, *Applied Physics Letters* 2005, 87, 234103.
- [19] X. Xiao, L. Qian, *Langmuir* 2000, 16, 8153.
- [20] S. Tamulevičius, I. Prosyčevs, A. Guobienė, J. Puišo, *Solid State Phenomena*, 2004.

- [21] R. Hunter, *Foundations of Colloid Science*, Oxford:Clarendon, New York 1987, 244.

Mimicking an Atomically-thin 'Vacuum Spacer' to Measure the Hamaker Constant between Graphene Oxide and Silica

Supporting information

## 1. Deduction of the Hamaker constant of Graphene oxide

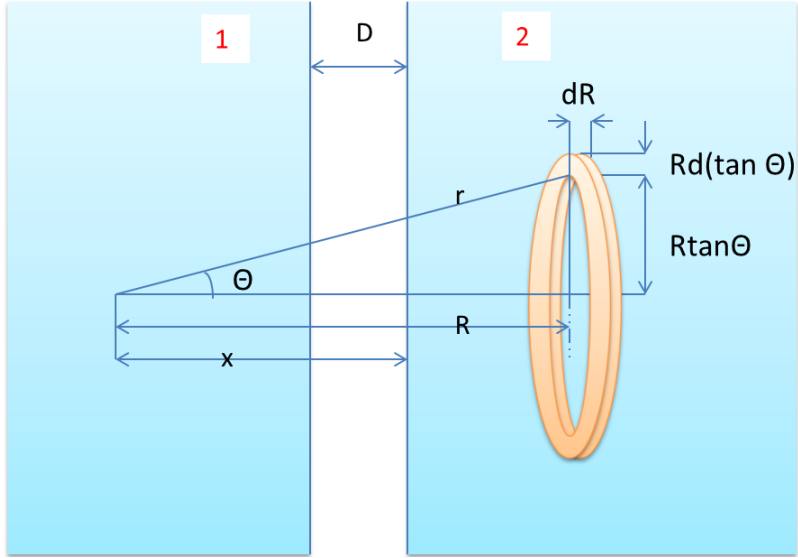


Fig S1. Derivation of the VdW interaction between flat surfaces, of two half-infinite bodies labelled phase 1 and 2.

According to the Hamaker-de Boer theory<sup>[1]</sup>, the VdW interaction energy between two plan-parallel surfaces of half-infinite bodies (see Fig. S1) can be calculated as follows<sup>[2]</sup>:

Firstly, the interaction between a single element in phase 1 and the whole phase 2 is calculated,

$$\begin{aligned}
 u_{1,\text{phase2}} &= - \int_x^\infty \int_0^\infty \frac{\beta_{12} \pi \rho_{N2} R^2 (d \tan \theta^2) dR}{r^6} \\
 &= - \pi \beta_{12} \rho_{N2} \int_x^\infty \int_0^\infty \frac{d(\tan \theta^2) dR}{R^4 (\tan \theta^2 + 1)^3} \\
 &= - \frac{\pi \beta_{12} \rho_{N2}}{6} \frac{1}{x^3} \tag{S1}
 \end{aligned}$$

Where  $-\frac{\beta_{12}}{r^6}$  describes the attractive energy between an element from phase 1 and one from phase 2, at a distance  $r$ . The parameter  $\beta_{12}$ , quantifying the strength of the interaction,



is related to the polarisibilities of the elements from 1 and 2.  $\rho_{N1}$  and  $\rho_{N2}$  are the number densities of such elements in phase 1 and in phase 2 respectively. The interaction energy between a column of unit cross section of phase 1 and the entire phase 2 is obtained by integration of  $u_{1,\text{phase2}}$  over  $x$  from  $D$  to  $\infty$ .

$$\begin{aligned}
 u_{\text{total}} &= \int_D^{\infty} u_{1,\text{phase2}} \rho_{N1} dx = \int_D^{\infty} -\frac{\pi\beta_{12}\rho_{N2}\rho_{N1}}{6} \frac{1}{x^3} dx \\
 &= -\frac{\pi\beta_{12}\rho_{N2}\rho_{N1}}{12D^2} \tag{S2}
 \end{aligned}$$

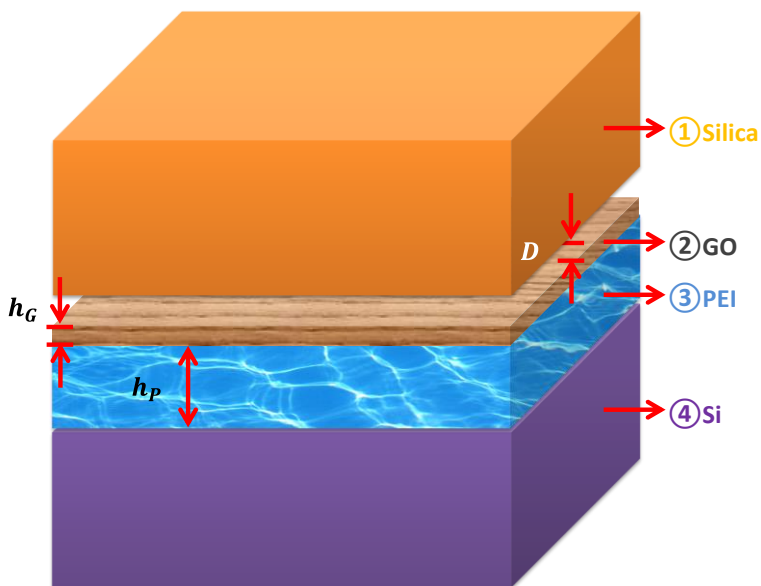


Fig S2. Schematic structure of a silica surface at distance  $D$  from a Si/PEI/GO surface.

In our experiment, we are measuring the interaction between a silica surface and a silicon surface covered by a layer of the polymer PEI and GO (indicated by Si/PEI/GO) as shown

in fig. S2. In fact the substrate is Silicon covered by a thin native Silica layer. We are in our paper interested in the difference between the interaction with areas where there is a monolayer of GO on the outside and areas where there is a bilayer of GO on the outside. In this difference the contributions due to the substrate cancel out anyway. The VdW interaction between a single element of phase 1 and phase 2-4 is described as follows, where  $D$  is the distance between the two flat surface,  $h_G$  is the thickness of GO and  $h_P$  is the thickness of the PEI layer.

$$\begin{aligned}
 u_{1,phase2} &= -\left[ \int_x^{x+h_G} \int_0^\infty \frac{\beta_{12}\pi\rho_{N2}R^2(d\tan\theta^2)dR}{r^6} \right. \\
 &\quad \left. + \int_{x+h_G}^{x+h_G+h_P} \int_0^\infty \frac{\beta_{13}\pi\rho_{N3}R^2(d\tan\theta^2)dR}{r^6} \right. \\
 &\quad \left. + \int_{x+h_G+h_P}^\infty \int_0^\infty \frac{\beta_{14}\pi\rho_{N4}R^2(d\tan\theta^2)dR}{r^6} \right. \\
 &= -\left[ \pi\beta_{12}\rho_{N2} \int_x^{x+h_G} \int_0^\infty \frac{d(\tan\theta^2)dR}{R^4(\tan\theta^2 + 1)^3} \right. \\
 &\quad \left. + \pi\beta_{13}\rho_{N3} \int_{x+h_G}^{x+h_G+h_P} \int_0^\infty \frac{d(\tan\theta^2)dR}{R^4(\tan\theta^2 + 1)^3} \right. \\
 &\quad \left. + \pi\beta_{14}\rho_{N4} \int_{x+h_G+h_P}^\infty \int_0^\infty \frac{d(\tan\theta^2)dR}{R^4(\tan\theta^2 + 1)^3} \right] \\
 &= -\left[ \frac{\pi\beta_{12}\rho_{N2}}{6} \left( \frac{1}{x^3} - \frac{1}{(x+h_G)^3} \right) + \frac{\pi\beta_{13}\rho_{N3}}{6} \left( \frac{1}{(x+h_G)^3} - \frac{1}{(x+h_G+h_P)^3} \right) \right. \\
 &\quad \left. + \frac{\pi\beta_{14}\rho_{N4}}{6} \left( \frac{1}{(x+h_G+h_P)^3} \right) \right] \tag{S3}
 \end{aligned}$$

The interaction energy between a column of unit cross section of phase 1 and the entire phase 2-4 is obtained by integration of  $u_{1,phase2}$  over  $x$  from  $D$  to  $\infty$ .

$$U(D) = \int_D^{-\infty} u_{1,phase2} \rho_{N1} dx$$

$$\begin{aligned}
&= -\left[\frac{\pi\beta_{12}\rho_{N2}\rho_{N1}}{12}\left(\frac{1}{D^2} - \frac{1}{(D+h_G)^2}\right) + \frac{\pi\beta_{13}\rho_{N3}\rho_{N1}}{12}\left(\frac{1}{(D+h_G)^2} - \frac{1}{(D+h_G+h_p)^2}\right)\right] \\
&+ \frac{\pi\beta_{14}\rho_{N4}\rho_{N1}}{12}\left(\frac{1}{(D+h_G+h_p)^2}\right) \quad (S4)
\end{aligned}$$

The Hamaker constant between phase 1 and phase 2 is defined as:  $A_{12} = \pi^2\beta_{12}\rho_{N1}\rho_{N2}$ ,

according to the Berhelot principle<sup>[2]</sup>,  $A_{12} \approx \sqrt{A_{11}A_{22}}$ ,

$$\begin{aligned}
U(D) &= -\left[\frac{A_{12}}{12\pi}\left(\frac{1}{D^2} - \frac{1}{(D+h_G)^2}\right) + \frac{A_{13}}{12\pi}\left(\frac{1}{(D+h_G)^2} - \frac{1}{(D+h_G+h_p)^2}\right)\right] \\
&+ \frac{A_{14}}{12\pi}\left(\frac{1}{(D+h_G+h_p)^2}\right) \quad (S5)
\end{aligned}$$

2. Contribution of Si in the total VdW energy between GO and Si surface with native silica layer

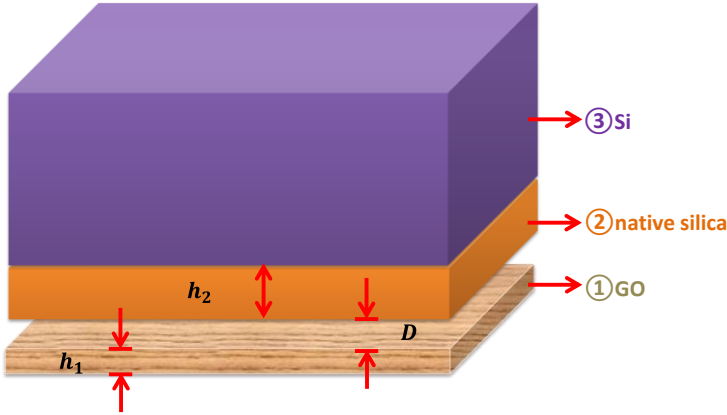


Fig S3. Schematic structure of a GO surface below a Si surface with native silica oxidized layer at distance  $D$ .

The AFM tip consists of Si (labelled by subscript 3 in subsequent equations) covered by a native oxide layer (Silica, Sa, labelled by subscript 2 in subsequent equations). According

to equation (s3), the VdW interaction between a single element of phase 1 and a phase 3 coated by a layer of 2 ( Si coated by Sa) is given by.

$$u_{1,phase23} = -\left[\frac{\pi\beta_{12}\rho_{N2}}{6}\left(\frac{1}{x^3} - \frac{1}{(x+h_2)^3}\right) + \frac{\pi\beta_{13}\rho_{N3}}{6}\left(\frac{1}{(x+h_2)^3}\right)\right]$$

(s6)

where  $D$  is the distance between the two flat surfaces, and  $h_2$  is the thickness of the native silica layer. The interaction energy between a column of unit cross section of phase 1 and the phase 3 coated by a layer of 2 is obtained by integration of  $u_{1,phase23}$  over  $x$  from  $D$  to  $D + h_1$ , where  $h_1$  is the thickness of GO.

$$\begin{aligned} U(D) &= \int_D^{D+h_{GO}} u_{1,phase23} \rho_{N1} dx \\ &= -\left\{\frac{\pi\beta_{12}\rho_{N2}\rho_{N1}}{12}\left[\left(\frac{1}{D^2} - \frac{1}{(D+h_1)^2}\right) - \left(\frac{1}{(D+h_2)^2} - \frac{1}{(D+h_2+h_1)^2}\right)\right]\right. \\ &\quad \left. + \frac{\pi\beta_{13}\rho_{N3}\rho_{N1}}{12}\left(\frac{1}{(D+h_2)^2} - \frac{1}{(D+h_2+h_1)^2}\right)\right\} \\ &= -\left\{\frac{A_{12}}{12\pi}\left[\left(\frac{1}{D^2} - \frac{1}{(D+h_1)^2}\right) - \left(\frac{1}{(D+h_2)^2} - \frac{1}{(D+h_2+h_1)^2}\right)\right]\right. \\ &\quad \left. + \frac{A_{13}}{12\pi}\left(\frac{1}{(D+h_2)^2} - \frac{1}{(D+h_2+h_1)^2}\right)\right\} \\ &= -(mA_{12} + nA_{13}) \end{aligned} \tag{s7}$$

Where  $A_{12} = \pi^2\beta_{12}\rho_{N1}\rho_{N2}$  and  $A_{13} = \pi^2\beta_{13}\rho_{N1}\rho_{N3}$ . The parameters  $m$  and  $n$  quantify the contributions to the total VdW interaction of the silica layer and of bulk silicon,

respectively. Using reasonable values  $D = h_1 = 0.9 \text{ nm}$  and  $h_2 = 2 \text{ nm}$ , we find that

$U(D) \approx 17A_{12} + A_{13}$ . So, the contribution of Si is relatively small and thus we neglect the effect of Si. Fig S4 shows the ratio  $m/n$  of the contributions from the silica layer and bulk

Si in the total VdW energy as a function of separation distance  $D$ , as calculated using

equation (s7). We see that neglecting Si becomes more accurate at small  $D$ , where the total VdW energy increases rapidly. When the surface separation distance  $D$  is small and VdW interaction is strong, the error is very small ( $<0.5\%$ ). When  $D$  increased to 1.5 nm, where the VdW interaction is 300 times decreased, the error is still less than 20%.

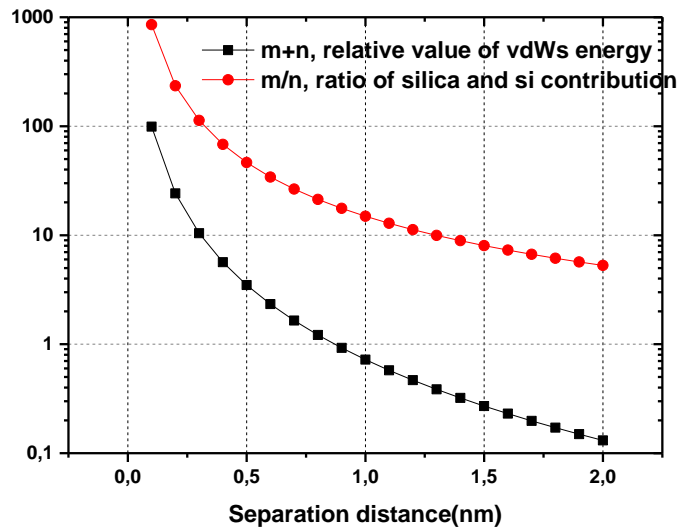


Fig S4. Evaluate the contribution from native silica layer and bulk silicon in the total VdW energy between GO and Si surface with 2 nm thick native oxidized silica layer.

### 3. Determination of the normalized adhesion force

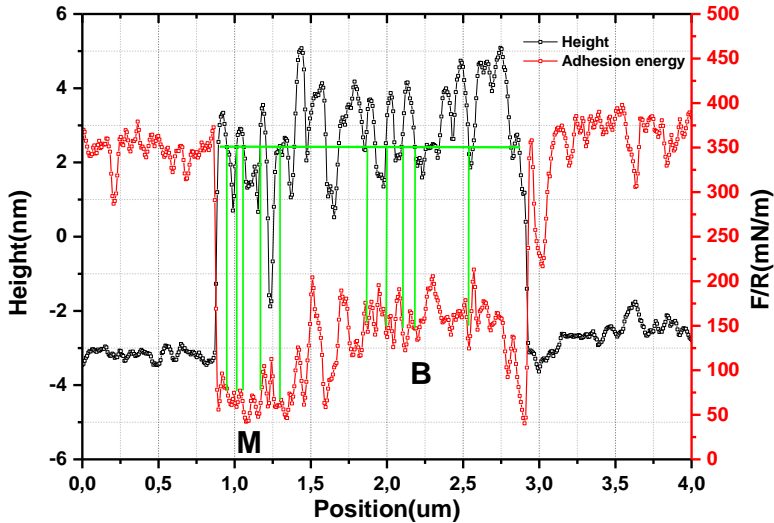


Fig S5. Illustration of the selection of measuring locations from the normalized force image of Fig.2.3c.

As explained in our letter's main text, and illustrated in Fig. 2.1a and 2.1b, in order to obtain the interaction between the AFM tip and the bottom layer of a GO bilayer we need to measure the adhesion force between the AFM tip and the Si/PEI/GO monolayer and between the AFM tip and Si/PEI/GO bilayer. Moreover, it is required that the thicknesses of the PEI/GO films at which these adhesion forces are measured are the same. The Hybrid Mode AFM method enables us to select Si/PEI/GO monolayer locations and Si/PEI/GO bilayer locations where the height is the same. Moreover, with this method the adhesion-force values at these locations are readily available. In Fig. S5, we see that there are considerable variations in the height of PEI/GO monolayer regions and PEI/GO bilayer regions, with an amplitude of about 2 nm. However, it is recognised as well that there are PEI/GO monolayer regions (marked as M) and PEI/GO bilayer regions (marked as B) with

similar height. Observe the regions where the height coincides with the green horizontal line. Ten locations are chosen; half of them are at a PEI/GO monolayer and the other half at PEI/GO bilayer. Thus, we have five separate experiments with the same situation as illustrated in Fig. 2.1a and 2.1b. The normalized adhesion force is  $76 \pm 3 \text{ mN/m}$  at the PEI/GO monolayer, and  $151 \pm 4 \text{ mN/m}$  at the PEI/GO bilayer. The difference is  $75 \pm 5 \text{ mN/m}$ .

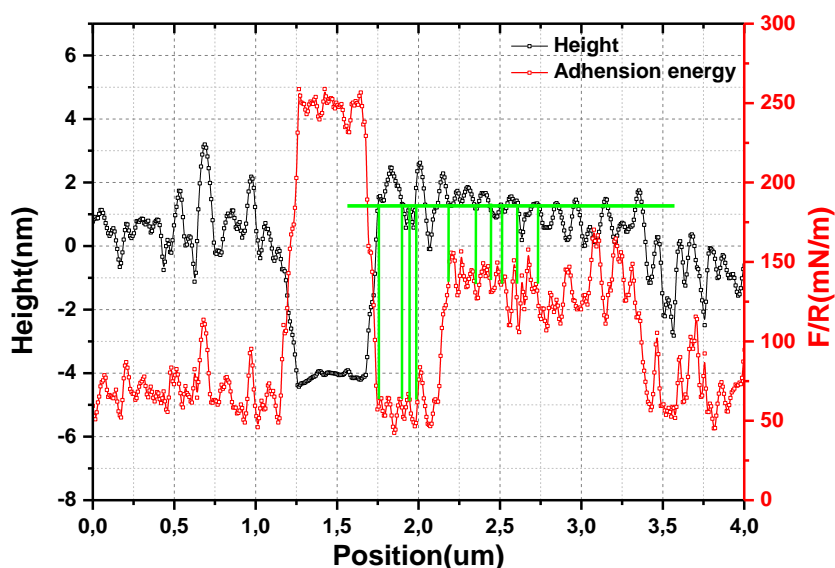


Fig S6. Illustration of the selection of measuring locations from the normalized force image of Fig. 2.3f.

The same approach to select measuring locations, was used for the repeated experiment (Fig. 2.3f, S6). Four PEI/GO monolayer locations were selected. There the normalized adhesion force was  $63 \pm 2 \text{ mN/m}$ . Six locations are selected at PEI/GO bilayer, at which the normalized adhesion force was  $136 \pm 3 \text{ mN/m}$ . The difference between these values is

$73 \pm 4 \text{ mN/m}$ . That this is the same, within experimental error, as with the first experiment, even though the separate forces at the monolayer and at the bilayer are different from the first experiment, confirms the soundness of our approach.

#### 4. Determination of the thickness of a single GO nanosheet



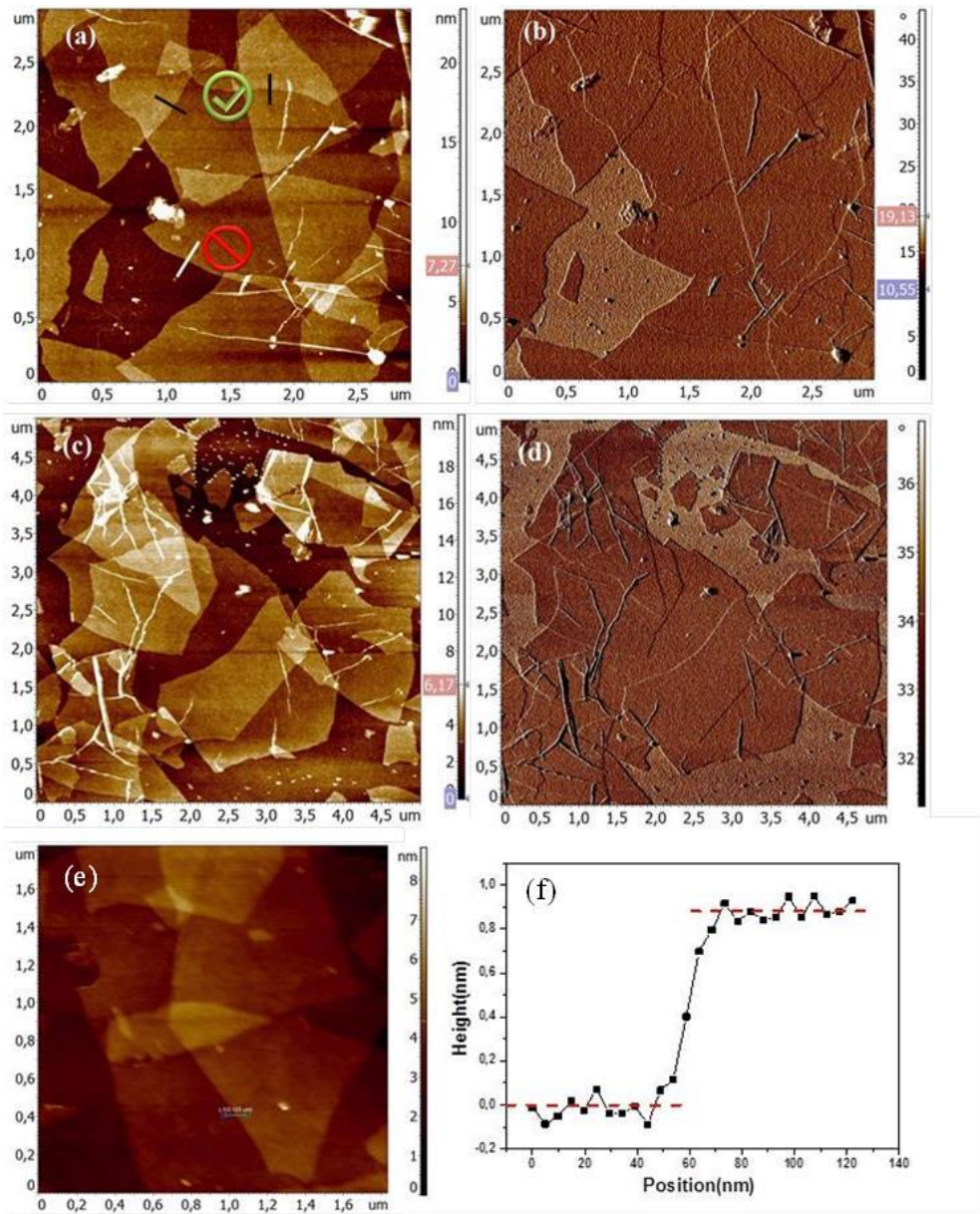


Fig S7. Measuring the thickness of a GO nanosheet. (a) and (c) show the height image at different locations of the Si/PEI/GO sample obtained by tapping mode AFM. The sample

has a similar structure as illustrated in Fig 2.2. The black lines in (a) show the data selection, where 2 GO layers overlapped. The white line in (a) shows the location that is not taken into account, where GO is on top of PEI. (b) and (d) are the AFM phase images corresponding with (a) and (b), respectively.<sup>[3]</sup> The PEI/GO patch and bare PEI patch can be easily differentiated from the phase images. (e) Height image obtained by contact mode AFM. (f) typical height profile from the height image (e).<sup>[4]</sup>

The thickness of a GO layer is determined as shown in Fig. S7. Fig S7.a and c show height images obtained by tapping mode AFM at different locations of a Si/PEI/GO sample with a similar structure as illustrated in Fig 2.2. In the phase image we recognize PEI patches and GO monolayer- or bilayer patches. The thickness of the upper layer of the GO bilayer was measured, by measuring the height difference along the edge between bilayer and monolayer, as marked by black lines in S7.a. Fig S7.e shows the height image obtained using contact mode AFM, the applied force is similar as used in Hybrid mode AFM scanning.

The average thickness of the GO upper layer of a PEI/GO bilayer patch measured over 30 points by means of tapping mode AFM is  $0.97 \pm 0.08 \text{ nm}$ . The average thickness of the GO upper layer measured over 10 points using contact mode is  $0.89 \pm 0.06 \text{ nm}$ . In Hybrid mode scanning, the AFM tip contacts with the surface. Thus, the later one was used to calculate the Hamaker constant here.

## 5. Characterization of GO

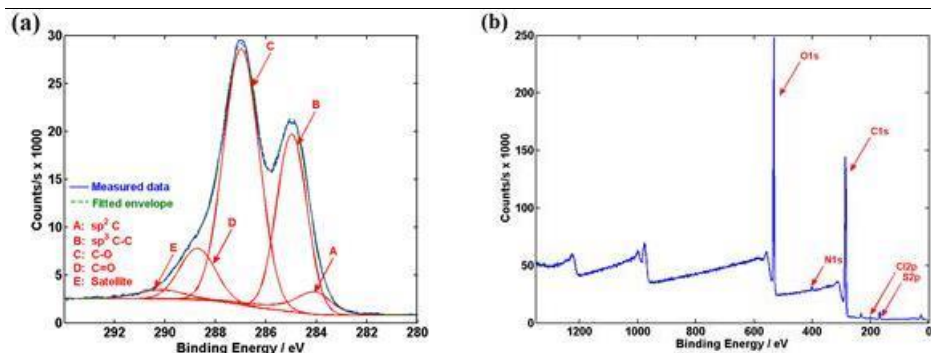


Fig S8. (a) High resolution C-1s-XPS spectrum of GO, and deconvoluted curves corresponding to C-C, C-O, and C=O moieties. (b) Survey spectrum of GO.

X-ray photoelectron spectroscopy (XPS) was used to characterise the elemental composition of the GO powder as received.<sup>[5]</sup> The C-1s-XPS spectrum of the GO is shown in Fig. S8, with the deconvoluted fitting curves. From the ratio of the peak areas, the molar ratio of C=O to C-O moieties is about 1:5. The atomic fraction of C and O is 67.5% and 30.4%, respectively. Besides C and O, XPS also revealed that the presence of S (1.6%) and Cl (0.6%), which must have been introduced into GO during manufacturing.

This elemental analysis was carried out using an X-ray Photoelectron Spectrometer (XPS, *Thermo Fisher Scientific, K Alpha* model). A monochromated Al  $K\alpha$  X-ray source was used. XPS measurements were taken in normal emission with a spot size of 100  $\mu\text{m}$  at a base pressure of  $10^{-8}$  mbar. During all XPS measurements, the flood gun was enabled to compensate for the potential charging of surfaces. Survey spectra and elemental region scans were taken at pass energy of 200 eV and 50 eV respectively and averaged over 10 scans. The spectra were analyzed using *Avantage* processing software. The XPS spectra were background corrected using the “Smart” base line function available in the software, and peak fitting was done using the Simplex peak fitting algorithm with a Gaussian (70%) – Lorentzian (30%) convolution function.

6. Determine the AFM tip radius using High-resolution SEM

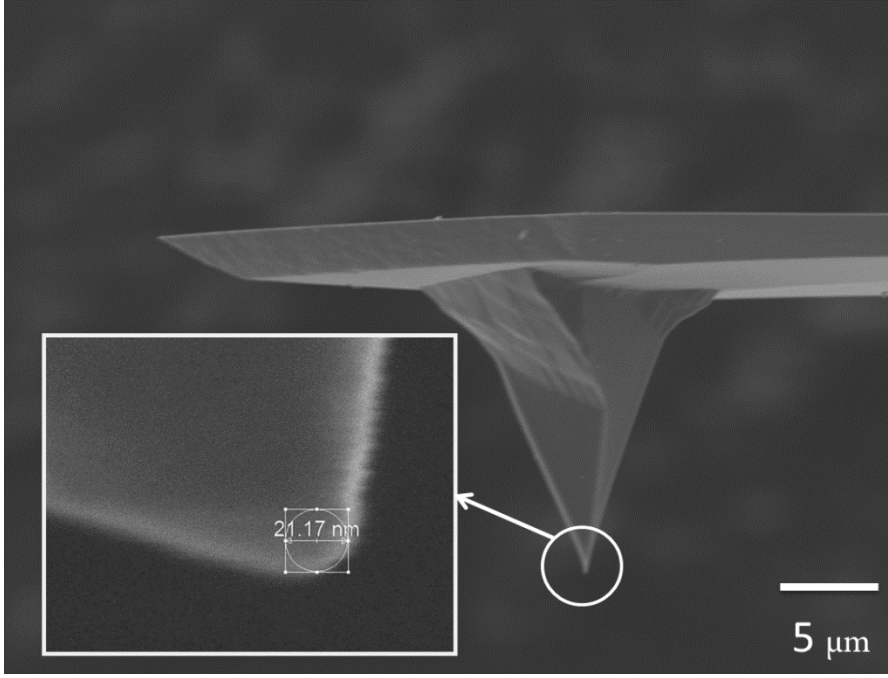


Fig S9. High-resolution SEM image of the AFM tip.

The Nova NanoSEM™ scanning electron microscope (SEM) was used to characterize the radius of the AFM tip. The radius of the AFM tip is determined as 10.6 nm. The AFM chip was glued on the substrate with its side face perpendicular to the substrate. The over view of the tip is recorded, at magnification of 3,500 (operated at 5 kV). The inset image is the high-resolution image of the tip, obtained at magnification of 650,000 (operated at 10 kV).

7. Calculation of the Hamaker constant between GO and silica

According to equation (5),  $A_{SG} = 8d^2 \frac{\Delta F}{R} + \sqrt{A_{SS}A_{PP}}$ , herein,  $d = 0.89 \pm 0.06 \text{ nm}$ ,

$A_{SS} = 16.09 k_B T$ ,  $A_{PP} = 13 \pm 3 k_B T$ . As shown in part 6, the tip radius is 10.6 nm. In the

Hybrid mode AFM, the tip radius was set as 10 nm, thus, the  $\frac{\Delta F}{R}$  is modified as  $70.75 \pm$

4.7 mN/m.  $A_{SG}$  was calculated as  $124.6 k_B T$ . According to the definition of error, the standard error for  $A_{SG}$  is

$$\sigma_{A_{SG}} = \sqrt{\left(\frac{\partial A_{SG}}{\partial \frac{\Delta F}{R}}\right)^2 \sigma_{\frac{\Delta F}{R}}^2 + \left(\frac{\partial A_{SG}}{\partial d}\right)^2 \sigma_d^2 + \left(\frac{\partial A_{SG}}{\partial A_{SP}}\right)^2 \sigma_{A_{SP}}^2} = 16.6 k_B T.$$

Thus, the Hamaker constant between GO and silica is determined as  $124.6 \pm 16.6 k_B T$ .

## 8. References

- [1] J. Visser, *Advances in Colloid and Interface Science* 1972, 3, 331.
- [2] J. Lyklema, 1991.
- [3] R. S. McLean, B. B. Sauer, *Macromolecules* 1997, 30, 8314; J. Tamayo, R. Garcia, *Langmuir* 1996, 12, 4430.
- [4] I. Schmitz, M. Schreiner, G. Friedbacher, M. Grasserbauer, *Analytical chemistry* 1997, 69, 1012.
- [5] S. C. Lee, S. Some, S. W. Kim, S. J. Kim, J. Seo, J. Lee, T. Lee, J.-H. Ahn, H.-J. Choi, S. C. Jun, *Scientific reports* 2015, 5.

# **Fast and Controlled Fabrication of Porous Graphene Oxide: Application of AFM Tapping for Mechano-chemistry**

# 3

---

The contents of this chapter are included in:

Chu, L.; Korobko, A. V.; Bus, M.; Besseling, N. A. M, Fast and Controlled Fabrication of Porous Graphene Oxide: Application of AFM Tapping for Mechano-chemistry, Manuscript submitted.

## Abstract

This chapter describes a novel method to fabricate porous graphene oxide (PGO) from graphene oxide (GO) by exposure to oxygen plasma. GO comprises of domains of graphene and of more polar, hydroxylated ones. When exposed to oxygen plasma, the different domains are etched with different rates, resulting in pore formation. Compared to other methods to fabricate PGO described so far, *e.g.* the thermal etching method, our method is about 100-1000 times faster. We studied the development of the pore formation with exposure time using atomic force microscopy (AFM). Surprisingly, we found that the development of PGO upon oxygen-plasma exposure is influenced by tapping mode AFM scanning method, using a Si tip. AFM tapping stops the growth of pores upon further plasma exposure at a level that coincides with the fraction of  $sp^2$  hybridised carbon atoms in the GO starting material. This constitutes the first report of AFM as a tool for application of local mechano-chemistry.

### **3.1 Introduction**

2D materials, with extremely high aspect ratio and high specific surface area, are promising for various applications, *e.g.* energy conversion and storage, sensors, composites, nano-mechanical and electrical devices.<sup>[1]</sup> Creating pores in 2D materials has become an increasingly crucial topic in these applications,<sup>[2]</sup> including hydrogen storage<sup>[3]</sup> and fuel cells,<sup>[4]</sup> molecular separation and ion recovery.<sup>[5, 6]</sup> For instance, for graphene and its derivatives, which are the most popular investigated 2D materials,<sup>[7]</sup> methods including bottom-up chemical approaches,<sup>[8]</sup> hydrothermal etching of graphene oxide (GO)<sup>[9]</sup> and high-energy physical techniques<sup>[6, 10]</sup> are used to fabricate porous 2D structures. Efficient fabrication of a 2D porous network structures by these methods knows many challenges that impede practical applications. For instance, the bottom-up approach and the high energy techniques are complex and operate at small scale.<sup>[6, 8, 10]</sup> Thermal etching of GO, which is low cost method and applicable on a large scale,<sup>[9, 11]</sup> is complex and time consuming (from hours to several days).<sup>[9, 11]</sup> As other compounds are added and by-products are fabricated during the etching, thus, post-etching purification, and transfer of the products are also challenging for these methods.<sup>[9, 11]</sup> Moreover, among all these methods, precise tuning and control of the formation of porous structures has not been reported so far.

In this chapter we study the formation of porous graphene oxide (PGO) by oxygen-plasma etching of GO, which is deposited on a Si wafer (with a thin native oxide layer) modified with an interlayer of polydiallyldimethylammonium chloride (PDADMAC). This positively charged interlayer strongly enhances the deposition of the negatively charged GO from an aqueous dispersion under the applied conditions of pH (6.5). We denote this layered system by GO/PDADMAC/Si.

### **3.2 Experimental Section**

#### **3.2.1 Chemicals and materials**

Graphene oxide (GO), synthesized using Hummer's method, was purchased from Graphene Supermarket. The elemental composition of GO was determined by using X-ray photoelectron spectroscopy (XPS).<sup>[14]</sup> A stable dispersion of 0.5 g GO in 1 L of Milli-Q



water was prepared using ultrasonication for 1 h, using an USC-TH ultrasonic bath from VWR Scientific. The dispersion was then centrifuged at 4000 rpm for 1 h, using a Megafuge 2.0R centrifuge from Heraeus Instruments with rotor radius of 20 cm. The supernatant was decanted and used for the sample preparation. Poly(diallyldimethylammonium chloride, PDADMAC,  $M_w = 200,000\sim 350,000$  g/mol, 20 wt% in water) solution and polyethylenimine (PEI,  $M_w = 25000$  g mol<sup>-1</sup>) were purchased from Sigma-Aldrich and used as received. 0.1 g/L aqueous polyelectrolyte solutions were prepared using milli-Q water. A chip of about of 1 cm × 1 cm was cut from a (100) Silicon wafer with a native oxide layer of about 2 nm thickness obtained from Sil'Tronix Silicon Technologies. The silicon chip was firstly rinsed with demi-water and ethanol followed by sonication using ethanol and acetone for 5 min., respectively. Oxygen plasma treatments of a silicon chip was performed for 1 min. at a pressure of 1600 mTorr (2.1 mbar), using a Harrick plasma cleaner (Anadis Instruments). After plasma treatment, the silicon chip was stored in milli-Q water for at least 24 h to equilibrate.

### 3.2.2 Sample preparation

Four different types of samples are prepared: GO/Si, hydrated & dried GO/PDADMAC/Si and dried GO/PEI/Si. GO/PEI/Si and GO/PDADMAC/Si samples were prepared by first coating the Si surface with a monolayer of polycations by dipping it in an aqueous PEI or PDADMAC solution (0.1 g L<sup>-1</sup>) for 15 min. The sample was then rinsed in milli-Q water for 5 min to remove non-adsorbed polyelectrolyte. GO solutions were then spin-coated onto the polycation/Si surfaces using an IBIS spincoater from Intersens Instruments B.V. Spin-coating was done at 2000 rad min<sup>-1</sup>. Due to the present carboxylic groups, GO is negatively charged at about neutral pH, and adsorbs readily on the positively charged PEI or PDADMAC layer. For GO/Si samples, GO solutions were directly spin-coated onto the Si surface. To remove excess of GO, the sample was rinsed in milli-Q water for 5 min. To prepare the dried samples they were kept in an oven for 3 h at 70°C. For obvious reasons, the Si surface and GO are both negatively charged, the GO coverage of GO/Si samples is much lower than for GO/PEI/Si and GO/PDADMAC/Si samples. All the dipping steps were done while the solution was stirred.

For the oxygen plasma treatments of the GO coated samples, we used the same instrument as used with the cleaning of the silicon chips. For each treatment, the samples are put on a glass disk and the disk was put at the same position in the plasma chamber. For the first GO/PDADMAC/Si sample 3 s, 9 s (12 s in total), 6 s (18 s in total) and 6 s (24 s in total) of oxygen (air) plasma treatments were performed at  $1500 \pm 100$  mTorr ( $2.0 \pm 0.1$  mbar). The second GO/PDADMAC/Si sample was treated for 3 s, 6 s, 9s, 12s, 15s, 18s, 21s, 24s, 27s and 30s (in total) at 700 mTorr (0.93 mbar). This sample received further treatments of 6 sec. at 700 mTorr (0.93 mbar) (so for in total 36 s, 42 s, 48 s, 54 s, 60 s, 66 s, 72 s, 78 s, 84 s and 90 s). Then, this sample receives further plasma treatments of 12 s at 700 mTorr (0.93 mbar), (so that the total plasma-treatment duration becomes 102 s, 114 s, 126 s, 138 s and 150 s). Then, this sample receives further plasma treatments of 24 s at 700 mTorr (0.93 mbar), (so that the total plasma durations become 174 s and 198 s). After that, 2 mins of plasma treatment is further performed followed by 24 s treatment under  $1500 \pm 100$  mTorr ( $2.0 \pm 0.1$  mbar).

### **3.2.3 AFM imaging**

A SOLVER NEXT AFM instrument from NT-MDT was used in all our AFM experiments. A HA-NC silicon tip, purchased from NT-MDT, with a nominal value for the tip radius of 7 nm (guaranteed < 10 nm) was used in tapping mode AFM measurements. A sharp AFM tip (diamond-like carbon tip, with a tip curvature radius of 1-3 nm) from NT-MDT is used to characterize the formed small pores. For the images for which the latter sharp tip was used this is explicitly indicated in the text and the figure captions. In all other cases, a HA-NC tip was used. For the repeated tapping-mode AFM scanning at the same area (enclosed by the red square in Fig 3.4.a), 2000 by 2000 points are obtained for a 2  $\mu$ m by 2  $\mu$ m area, using a tapping frequency of 0.5 Hz.

### **3.3 Formation of pores due to oxygen plasma**

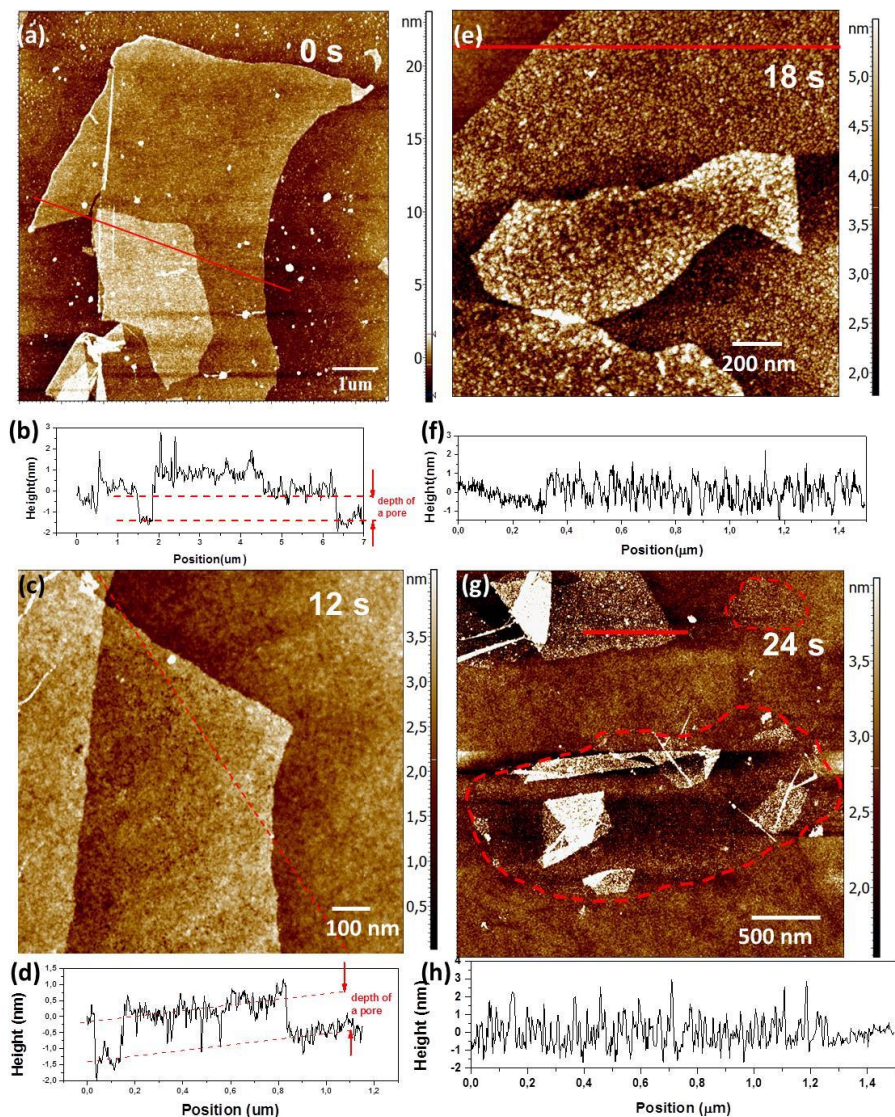


**Figure 3.1.** (a) AFM height image of an untreated GO/PDADMA/Si sample. (b) Height profile along the red line in (a). (c) AFM height image of a different region of the same sample as in (a), after treatment with oxygen plasma for 12 sec. at  $1500 \pm 100$  mTorr ( $2.0 \pm 0.1$  mbar). A larger-area scan including this region is shown in Fig S1.a (in the supporting information 1). (d) Height profile along the red line in (c). (e) AFM height image of again a different region of the same sample, after treatment with oxygen plasma

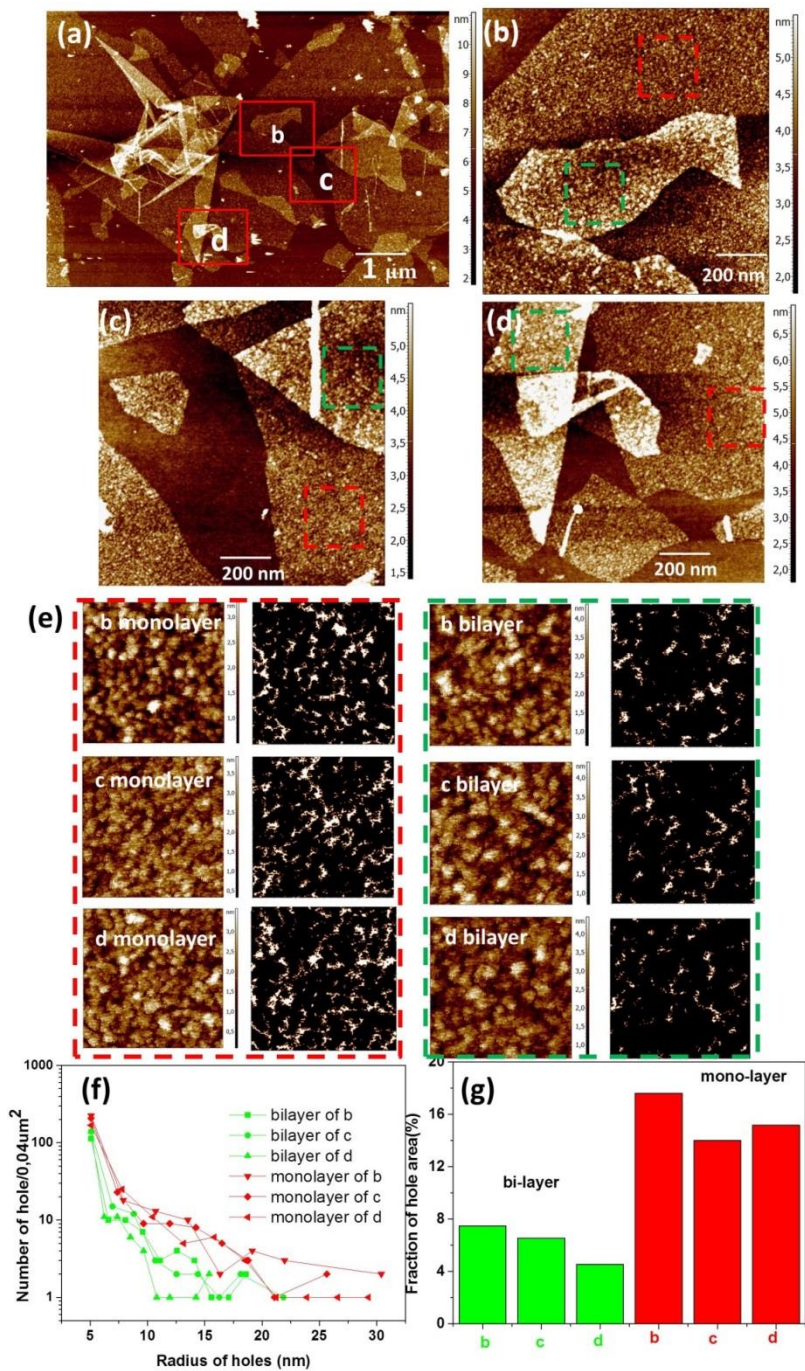
for an additional 6 sec. (18 sec. in total). (f) Height profile along the red line in (e). (g) AFM height image of another region of the same sample, after treatment with oxygen plasma for an additional 6 sec. (24 sec. in total). The red dashed lines show the edges of the monolayer GO. The larger-area scan including this region is shown in Fig S1.b. (Appendix) (h) Height profile along the red line in (g).

Figure 3.1 shows the tapping-mode AFM height images of a GO/PDADMAC/Si sample, when treated with oxygen plasma at a pressure of  $1500 \pm 100$  mTorr ( $2.0 \pm 0.1$  mbar) for 0, 12 s, 18 s and 24 s, respectively. As shown in Figures 3.1.a and 3.1.b, the thickness of single layer GO nano-sheet deposited on PDADMAC is  $1.5 \pm 0.3$  nm, which is consistent with the results in the literature.<sup>[12, 13]</sup> The thickness of an additional GO layer deposited on top of GO/PDADMAC/Si, forming an overall GO bilayer on top of the PDADMAC, is slightly thinner (is about  $1.0 \pm 0.3$  nm).<sup>[13]</sup> So, a GO bilayer is thinner than twice a GO monolayer. It was found by others as well that a GO nano-sheet fits the roughness of another GO surface better than with other surfaces at dry condition.<sup>[13]</sup> Along the red line in Figure 3.1.a, a rupture in the GO flake is clearly recognized, at the position 1.5-1.8  $\mu\text{m}$  shown in Figure 3.1.b. When the depth of a ‘well’ in a GO surface is comparable to that of the rift, the ‘well’ is concluded to completely perforate the GO layer, and is denoted as a pore (Appendix 2). As shown in the height profile in Figure 3.1.b, along the red line in Figure 3.1.a, an untreated GO flake has a continuous 2D structure with a roughness of about  $0.6$  nm<sup>[13]</sup>, and no pores are detected. After treatment with oxygen plasma for 3 sec. at  $1500 \pm 100$  mTorr ( $2.0 \pm 0.1$  mbar), still no pores are detected (supporting information part 3). This may however be due to the resolution, which is limited by the AFM-tip size. For AFM height-morphology scanning, the lateral resolution is largely determined by the radius of the AFM tip. The radius of the AFM tip we used for most experiments was about 10 nm.<sup>[14]</sup> For 1 nm thick GO, only pores with a radius larger than 4.3 nm can be detected by a 10 nm tip (Appendix 4). Figure 3.1.c shows the height morphology of the same sample, after another 9 sec. of plasma treatment at the same pressure (12 sec. in total). Pores are now clearly recognised as dark spots on the GO flakes. At the position of around 0.1  $\mu\text{m}$  along the dashed red line (see the axis of Figure 3.1.c), it crosses a gap between two partly overlapping GO flakes. We found that the depth of the above-mentioned pores is similar to

that of the gap, which confirms that the pores are indeed pores piercing the GO nano-sheets. The porosity of this PGO is quantified by analysing the size distribution of the pores (supporting information 5).<sup>[15]</sup> As shown in Figure 3.1.e, after further plasma treatment for another 6 sec. (18 sec. in total), the number density of pores has significantly increased, both on the monolayer and bilayer patches. The pores start to connect with each other to form larger pores. Figure 3.1.g shows the height morphology of the sample after further treatment with oxygen plasma at the same pressure for another 6 sec. The dashed red lines indicate the circumferences of areas of present monolayers of GO. We can clearly see that the monolayer GO flakes in these areas are largely etched away. The bilayer patches are still partially left (Figure 3.1.h) and form a similar porous network structure as the monolayer of PGO obtained after 18 sec. of plasma treatment (Supporting information 1).

### 3.4 pore-size distribution

As it is important for most applications, we analysed the pore-size distribution after the sample was treated with oxygen plasma for 18 s in total (Figure 3.2). Figure 3.2.a shows a large area of the sample, where several PGO flakes are clearly seen. We can distinguish between monolayer (P)GO and regions covered by two layers of (P)GO. In Figure 3.2.e, enclosed by the dashed red box, three zoomed-in images of monolayer PGO are shown. Images of bilayer PGO are enclosed by the dashed green box. The pore-size distributions, obtained using the grain method,<sup>[15]</sup> reveal that the number densities of small pores (diameter of 5 nm) are similar for monolayer GO and for GO that forms the top layer of a GO bilayer. However, larger pores are considerably more numerous for monolayer GO than for the GO toplayer of a bilayer. This indicates that the substrate below a GO flake influences its sensitivity to oxygen-plasma etching. GO deposited on PDADMAC/Si is more sensitive to oxygen plasma than GO deposited on top of another GO layer. This is probably related to the finding mentioned above, that GO fits better with other GO than on other substrates. The pore-size distributions of different PGO regions at the same substrate are roughly the same. The small variation that does occur might be due to slight variations in the chemical composition of GO.



**Figure 3.2.** (a) AFM height image of GO/PDADMAC/Si, the same sample as in Figure 3.1, after treatment with oxygen plasma for 18 sec. in total. 2.b, 2.c and 2.d show more detailed AFM height morphologies of the red-boxed areas in 2.a. In 2.b, 2.c and 2.d. Squares marked with dashed red boxes are at monolayer GO and squares marked with dashed green boxes at bilayer GO. These areas of  $200 \times 200 \text{ nm}^2$  are studied quantitatively using the grain method.<sup>17</sup> (e) The left images in the dashed red box are the selected monolayer areas and the right images show the porous structures analysed using the grain method. In the latter images, the white color corresponds to pores. The dashed green box in (e) illustrates the grain method analysis for bilayer areas. (f) The pore-size distributions of the selected areas in (e), as obtained by the grain method, (g) Percentages of pore area of the total GO surface area of the areas shown in (e).

### 3.5 Influence of the pressure of oxygen plasma treatment

In order to quantify the evolution of PGO, a new GO/PDADMAC/Si sample is prepared (see 3.2.2 Sample preparation) and treated with oxygen plasma at 700 mTorr (0.93 mbar). The etching rate at 700 mTorr (0.93 mbar) is expected to be slower than at  $1500 \pm 100$  mTorr ( $2.0 \pm 0.1$  mbar), enabling us to better follow the evolution of pores. Using a ultra-sharp AFM tip (a diamond-like carbon tip, with tip curvature radius of 1-3 nm), pores with radii of 2 to 5 nm are detected, after the sample is treated with oxygen plasma at 700 mTorr (0.93 mbar) for 24 sec., as shown in Figure 3.3.b and c. When treated for 3 to 21 sec., no pores are detected yet (Appendix 7).

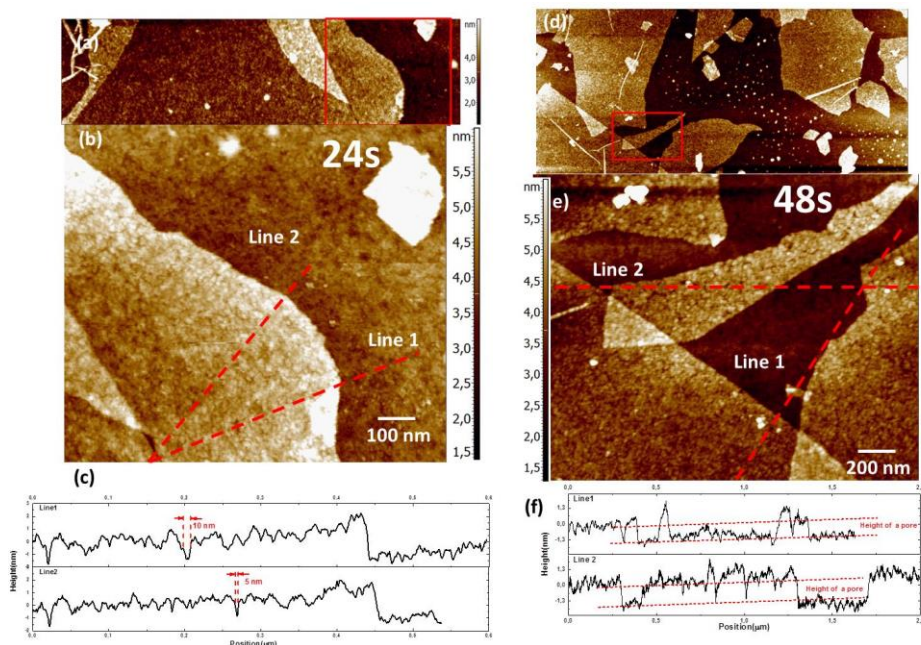
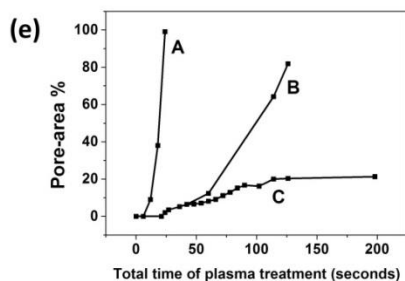
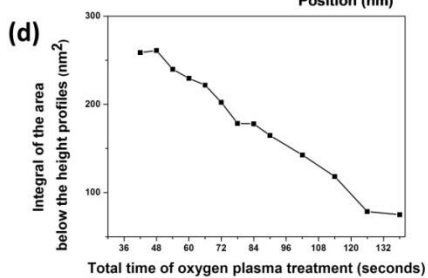
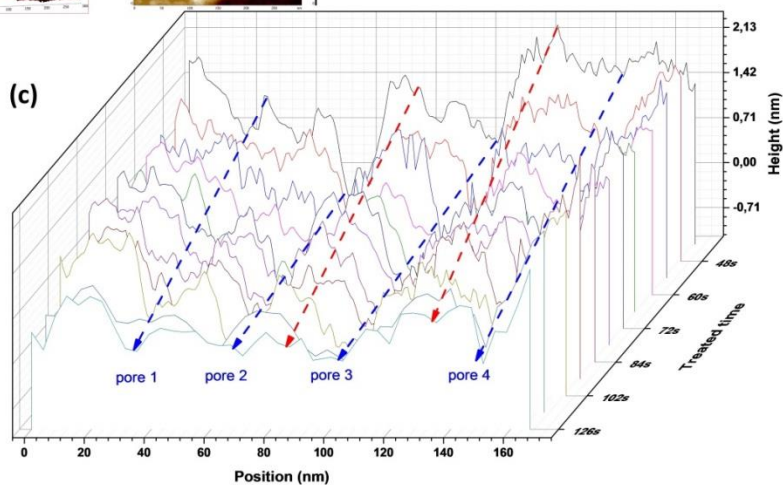
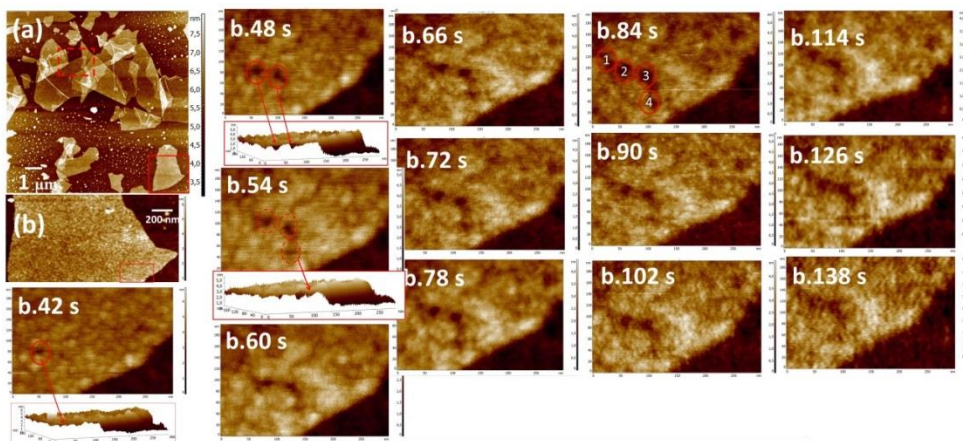


Figure 3.3. (a) Height morphology of 24 sec. treated GO/PDADMAC/Si sample characterized using sharp AFM tip (see the experimental part). (b) High resolution scan of the area in the red box of (a). (c) Height profiles of the sample along the red lines in (b). (d) 48 sec. treated GO/PDADMAC/Si sample with normal AFM tip (see the experimental part). (e) High resolution scan of the area in the box of (e). The pressure of all the oxygen plasma treatment here is 700 mTorr (0.93 mbar). (f) Height profiles of the sample along the red lines in (f).





**Figure 3.4.** (a) Height morphology of a GO/PDADMAC/Si sample treated for 42 sec. with oxygen plasma at 700 mTorr (0.93 mbar), characterized using AFM. (b) Detailed scan of the area marked as solid red box. Sequence of AFM images of the area enclosed by the red box of (b), recorded after each subsequent 6 sec. plasma treatment, named as (b.42 sec.) to (b.138). In this area ( $200 \times 300 \text{ nm}^2$ ), 4 pores are formed as shown in (b.84). (c) Height profiles taken along the line through the centres of the four pores. (d) Integral of the area under the height profile lines in (c) vs. plasma-exposure time. (e) Development of the pore-area; the effect of plasma pressure and of AFM tapping. The curves labelled A and B are for  $1500 \pm 100 \text{ mTorr}$  ( $2.0 \pm 0.1 \text{ mbar}$ ) and  $700 \text{ mTorr}$  (0.93 mbar), respectively. The curve labelled C shows the stalling of pore growth at 700 mTorr (0.93 mbar) for an area that undergoes repeated AFM tapping-mode imaging.

After plasma treatment at 700 mTorr (0.93 mbar) for 42 s, pores are clearly visible in the AFM images Figure 3.4.a and b (using the normal tip). The area enclosed by a red box in Figure 3.4.a was investigated in more detail. After each subsequent 6-second plasma treatment an image was recorded by tapping mode AFM. The sequence of images illustrates the emergence, growth and clustering of pores (labeled 1 - 4 in the b.84s image). These four pores gradually get connected and finally form one large pore. Height profiles along a line through the centres of these four pores are shown in Figure 3.4.c. Figure 3.4.d shows the evolution of the integral of the area under the height profiles in Figure 3.4.c. We assume that the depth of pore 2 is constant after 48 s treatment and the level at the bottom of that pore is chosen as the zero height level. This integral corresponds to the amount of material that is still left. We observe a linear decrease of this area, which indicates that the etching rate along this line is constant. At other positions, where no pores were formed after the first 42 sec., no new pores are formed later on, and there is no material loss upon plasma exposure. These observations indicate GO has domains that are susceptible to oxygen plasma, where pores arise already after brief plasma exposure, and domains that are more stable with respect to plasma treatment, where no pores arise even after prolonged exposure time.

With the investigations described above, a region on a GO flake (the area enclosed by the red box in Figure 3.4.a) was repeatedly investigated by tapping-mode AFM. During those

investigations we got indications that this AFM tapping procedure itself influences the evolution of the pore morphology upon plasma exposure. In order to if AFM tapping procedure influences the evolution of the pore morphology upon plasma exposure, we also investigated the morphology after different durations of plasma exposure at randomly selected locations, that had not been imaged before. Comparing the results of the latter measurement with those of the repeated measurements at the red-boxed area clearly demonstrates that the AFM tapping procedure significantly reduces the etching rate. More AFM characterizations at 700 mTorr (0.93 mbar) (curve B) are included in Fig S6. As shown in Figure 3.4.e (and also in Fig S6), the etching rate at the red-boxed area was significantly lower. Especially after about 50 sec., when pore development in the red-boxed area started to levelled off. After about 120 sec. of plasma treatment with intermittent tapping-mode AFM scans, further pore development has ceased completely, and the total pore area reaches a plateau.

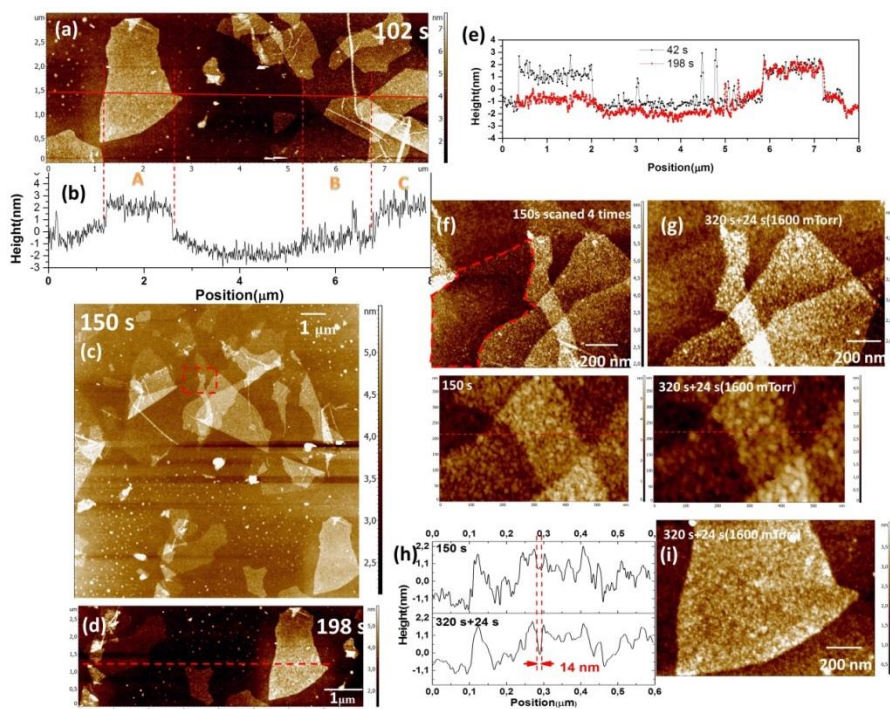


**Figure 3.5.** (a) Height morphology of the sample treated with oxygen plasma for 102 s at 700 mTorr (0.93 mbar). (b) Height profile along the red line in (a). (c) Height morphology of the sample treated with oxygen plasma for 150 s at 700 mTorr (0.93 mbar). The area is

the same as in Figure 3.3.a. (d) Height morphology of the sample treated with oxygen plasma for 198 s at 700 mTorr (0.93 mbar). (e) Height profiles along the dashed red line in (d) after 42 s and 198 s, respectively. (f) Detailed scans of the area enclosed by the dashed red box of (c) after 150 s of plasma treatment (in total). (g) Height profiles of the same area as (f), after 320 s of plasma treatment (in total) at 700 mTorr (0.93 mbar) followed by an additional 24 s at  $1500 \pm 100$  mTorr ( $2.0 \pm 0.1$  mbar). (i) Height profiles after the same treatments as with (g), of the area, where we performed AFM imaging after every plasma treatment.

In Figure 3.5.a and b, measured after 102 sec. of plasma treatment, interval A of the red trajectory is across the red-boxed area of Figure 3.4.a, which was repeatedly scanned by tapping-mode AFM. Interval B, which runs across another GO monolayer (a long wrinkle is clearly recognized), was scanned for the first time when image 4.a was obtained. We clearly observe that at B, GO has eroded much more than at A. In fact, at B it is almost completely etched away. As shown in Figure 3.5.d and 5.e, after 198 s of plasma treatment, the red-boxed GO that was repeatedly scanned by tapping-mode AFM is still largely preserved, while the surrounding GO is almost completely etched away. So, it turns out that tapping mode AFM influences the evolution of PGO upon oxygen-plasma exposure: that AFM tapping protects PGO against the effect of oxygen plasma. This implies that we can use AFM tapping as a method of localised control of the porosity of PGO. In order to verify this, we made some further tests on the sample that had been treated with oxygen plasma at 700 mTorr (0.93 mbar) for 150 s. We scanned the area enclosed by the dashed red box in Figure 3.5.c for 4 times (see the sample preparation part). This is the same area as in the dashed red box in Figure 3.4.a. We found that after these 150 sec. of plasma exposure, the monolayer area (enclosed by a dashed red contour in 5.f) is almost completely removed, similarly as the other areas, shown in Fig S6.n and S6.o. Then the sample is further treated with oxygen plasma for a further 120 s under 700 mTorr (0.93 mbar) and 24 s at  $1500 \pm 100$  mTorr ( $2.0 \pm 0.1$  mbar). We found that the area that was scanned after every plasma treatment does not change significantly as compared to what is seen in Figure 3.5.i, and in the dashed red box in Figure 3.5.c. The morphology of this area is similar to that shown in Figure 3.5.h, which was obtained after 150 s treatment. This demonstrates that our

fabrication method of PGO can be controlled by AFM tapping as patches with various porosities are fabricated on one sample.

### 3.6 Discussion

We will now try to formulate a comprehensive interpretation of the observations described above: the generation and growth of pores in GO due to oxygen plasma, and the effect of AFM tapping on the retardation of that process. This interpretation is schematically illustrated in Figure 3.6. First we need to consider that GO has graphene domains and more polar hydroxylated domains as shown in Figure 3.6.0. It is known that apolar compounds and moieties are more reactive to oxygen-plasma than polar ones.<sup>[16]</sup> For GO, this implies that the graphene domains are more reactive than the hydroxylated ones, as the latter oxygenated carbon moieties have lower free energy. So, pores arising in the early stages of plasma treatment are formed most likely in the graphene domains, as illustrated in Figure 3.6.1. Upon prolonged exposure to oxygen plasma, additional pores are formed, most likely in the graphene domains, and existing pores grow larger. When the edge of a pore in a graphene domain reaches the boundary between the graphene and a hydroxylated domain, the pore can grow further because at the edge of a pore the backbone carbons of the hydroxylated domains are exposed to attack by high-energy oxygen species (e.g.  $O^+$ ). So ultimately GO is completely etched away, as illustrated in the sequence 1 to 6 in Figure 3.6. This corresponds to the experimental observations shown in Figure 3.1.a to d, where we see increase of pores both in numbers and in size, and for the region B in Figure 3.4.a and b, where GO is almost completely etched away upon prolonged plasma treatment. This unbounded etching is quantified in curves A and B in Figure 3.4.d. **However, we observed in Figure 3.4 that this does not happen for GO that is repeatedly scanned by tapping mode AFM.** These images show that expansion of pores does not occur equally in all directions. Some pores become long and narrow rather than spherical. Moreover, the total pore area does not increase. Rather, the increase of the total pore area levels off and reaches a plateau, as quantified by curve C in Figure 3.4.d.

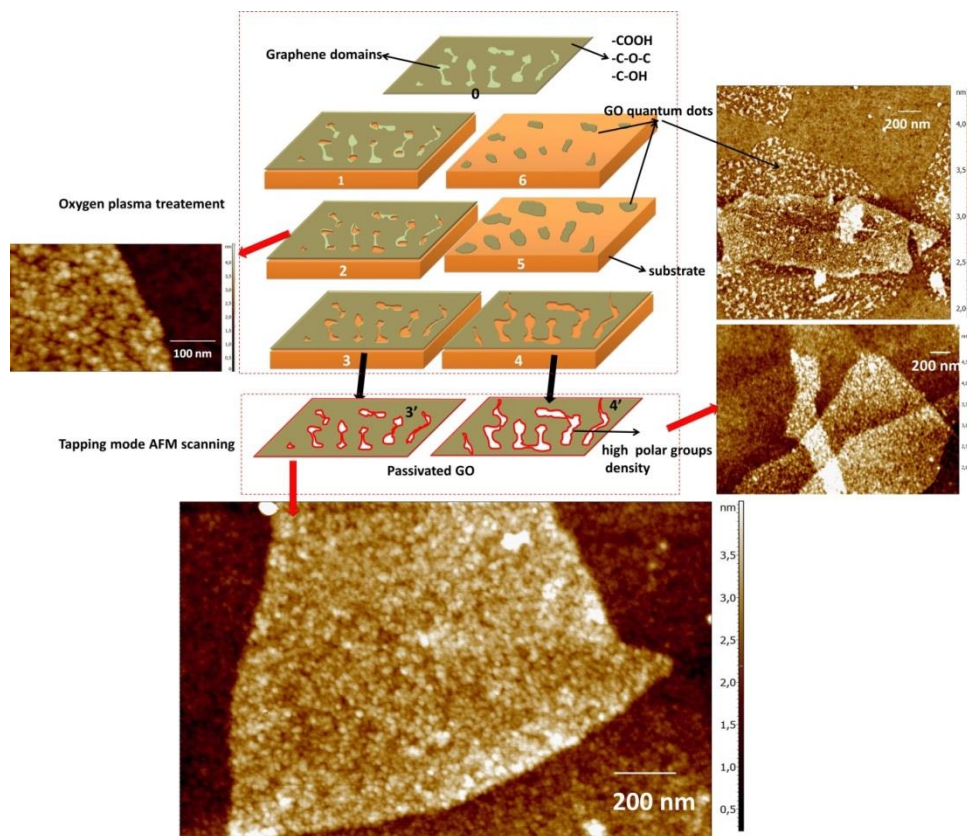


**Figure 3.6.** Schematic drawing of the evolution of PGO upon treatment by oxygen plasma and AFM tapping. Picture 0 shows the structure of GO, composed of graphene and hydroxylated domains. Structures 1 - 6 illustrate the evolution of PGO under oxygen plasma treatment.

How to explain what is going on? A clue is offered by the finding that the total pore area of GO that has undergone repeated AFM tapping reaches a plateau at about 20% of the total area. This percentage corresponds to the percentage of  $sp^2$  hybridised carbon atoms in the GO starting material, as found by XPS.<sup>[14]</sup> Obviously, the  $sp^2$  hybridised carbons correspond to graphene domains, whereas  $sp^3$  hybridised carbons correspond to the hydroxylated ones in the polar domains of GO. Hence, we infer that in some way AFM tapping has the effect that pore growth beyond the graphene domains is prevented, and that the sizes and shapes of the pores, as obtained by the combination of plasma treatment and AFM tapping corresponds to the sizes and shapes of the graphene domains in the original

GO starting material. This is illustrated in Figure 3.6.2 and 3.6.3. It is still puzzling how AFM tapping brings about the effect of stabilising the edges of hydroxylated domains, and leads to protection against further attack by high-energy oxygen species. As a first step of etching at the atomic level, high-energy oxygen species attack and forming reactive oxygen radical intermediates. Subsequently, C-C bonds are expected to break and small volatile organic molecules, like CO, CO<sub>2</sub>, are formed. It seems that in some way AFM tapping interferes with this process. In order to obtain an AFM image, the sample is taken out of the plasma chamber. This allows for the exposed C atoms and their formed reactive oxygen radical species to react with water molecules present in the air. The highly reactive radicals are converted to less reactive hydroxylated groups, similar as already present in the hydroxylated domains. On return of the sample in the plasma chamber, these parts have become now less reactive. This interpretation also explains our finding that the etching rate observed at 700 mTorr (0.93 mbar) is significantly slower compared to the rate observed at  $1500 \pm 100$  mTorr ( $2.0 \pm 0.1$  mbar), than the expected decrease of 700/1500. In the former case (700 mTorr (0.93 mbar)) the sample was taken out of the plasma chamber more often. Only at regions that have undergone AFM tapping, etching levels off and reaches a plateau value. Apparently, at those regions, intermediate polar moieties at the edges of hydroxylated domains are stabilized by AFM tapping in a way that leads to protection against further plasma etching (24 s at  $1500 \pm 100$  mTorr ( $2.0 \pm 0.1$  mbar); Figure 3.5.g and 5.i). This is illustrated in Figure 3.6.3' and 4'. This effect of AFM tapping constitutes an interesting example of mechano-chemistry.<sup>[17]</sup> Current researches show that lateral force microscopy is a powerful tool for local mechano-chemistry.<sup>[18]</sup> Our work constitutes the first example of AFM tapping as a tool for local mechano-chemistry. Another interesting feature of the observed mechano-chemical effect observed here is that it involves stabilisation of chemical structures, whereas most other known mechano-chemical effects involve breaking of, often macromolecular, bonds. Meanwhile, our observations constitute a warning that tapping-mode AFM imaging is not always as inconsequential for the investigated surfaces as is usually assumed.

According to the hypothetical mechanism described above, the size and shape of the pores after plasma treatment in combination with AFM tapping correspond to those of the

graphene domains of the GO starting material, as illustrated by Figure 3.5.3' evolving from Figure 3.5.0.

### **3.7 Conclusions**

We report a fast and controlled method to fabricate PGO and GO nano-flakes. A hypothetical mechanism is proposed. GO comprises of graphene domains ( $sp^2$  C atoms) and more polar, hydroxylated ones ( $sp^3$  C atoms). When GO is deposited on Si/PDADMAC surface and is exposed to oxygen plasma, the different GO domains are etched with different rates. The graphene domains are more reactive with oxygen plasma. Firstly, PGO with pore diameter of several nanometers is fabricated in a few sec. When the pores are all connected, GO nano-flake are fabricated. GO will be all etched away in a few min. Compared to other methods to fabricate PGO described so far, e.g. the thermal etching method, our method is faster by a factor of  $10^2$ - $10^3$ . Moreover, we demonstrate an effective approach to control the process by applying AFM tapping in between subsequent plasma treatments. This constitutes the first example where tapping mode AFM is used as a tool for mechano-chemistry.

### **3.8 References**

- [1] A. Gupta, T. Sakthivel, S. Seal, *Progress in Materials Science* 2015, 73, 44.
- [2] H. Zhang, I. Hussain, M. Brust, M. F. Butler, S. P. Rannard, A. I. Cooper, *Nature materials* 2005, 4, 787.
- [3] A. Du, Z. Zhu, S. C. Smith, *Journal of the American Chemical Society* 2010, 132, 2876.
- [4] Y. Zhu, S. Murali, M. D. Stoller, K. Ganesh, W. Cai, P. J. Ferreira, A. Pirkle, R. M. Wallace, K. A. Cychoz, M. Thommes, *Science* 2011, 332, 1537.
- [5] D.-e. Jiang, V. R. Cooper, S. Dai, *Nano letters* 2009, 9, 4019; S. Blankenburg, M. Bieri, R. Fasel, K. Müllen, C. A. Pignedoli, D. Passerone, *Small* 2010, 6, 2266; K. Huang, G. Liu, Y. Lou, Z. Dong, J. Shen, W. Jin, *Angewandte Chemie International Edition* 2014, 53, 6929.
- [6] S. P. Koenig, L. Wang, J. Pellegrino, J. S. Bunch, *Nature nanotechnology* 2012, 7, 728.



- [7] A. K. Geim, K. S. Novoselov, *Nature materials* 2007, 6, 183.
- [8] M. Bieri, M. Treier, J. Cai, K. Ait-Mansour, P. Ruffieux, O. Gröning, P. Gröning, M. Kastler, R. Rieger, X. Feng, *Chemical communications* 2009, 6919.
- [9] D. Zhou, Y. Cui, P.-W. Xiao, M.-Y. Jiang, B.-H. Han, *Nat. Commun.* 2014, 5.
- [10] R. Zan, Q. M. Ramasse, U. Bangert, K. S. Novoselov, *Nano letters* 2012, 12, 3936.
- [11] T. H. Han, Y.-K. Huang, A. T. Tan, V. P. Dravid, J. Huang, *Journal of the American Chemical Society* 2011, 133, 15264.
- [12] D. R. Dreyer, S. Park, C. W. Bielawski, R. S. Ruoff, *Chemical Society Reviews* 2010, 39, 228.
- [13] K. A. Mkhoyan, A. W. Contryman, J. Silcox, D. A. Stewart, G. Eda, C. Mattevi, S. Miller, M. Chhowalla, *Nano letters* 2009, 9, 1058.
- [14] L. Chu, A. V. Korobko, A. Cao, S. Sachdeva, Z. Liu, L. C. de Smet, E. J. Sudhölter, S. J. Picken, N. A. Besseling, *Advanced Materials Interfaces* 2016.
- [15] Q. Guan, B. Norder, L. Chu, N. A. Besseling, S. J. Picken, T. J. Dingemans, *Macromolecules* 2016, 49, 8549.
- [16] G. Taylor, T. Wolf, *Polymer Engineering & Science* 1980, 20, 1087.
- [17] C. R. Hickenboth, J. S. Moore, S. R. White, N. R. Sottos, J. Baudry, S. R. Wilson, *Nature* 2007, 446, 423.
- [18] E. Barrena, S. Kopta, D. F. Ogletree, D. H. Charych, M. Salmeron, *Physical review letters* 1999, 82, 2880; R. W. Carpick, T. D. Jacobs, *Microscopy and Microanalysis* 2014, 20, 1542; R. W. Carpick, M. Salmeron, *Chemical reviews* 1997, 97, 1163; T. D. Jacobs, R. W. Carpick, *Nature nanotechnology* 2013, 8, 108; R. Overney, E. Meyer, J. Frommer, D. Brodbeck, R. Lüthi, L. Howald, H.-J. Giintherodt, M. Fujihira, H. Takano, Y. Gotoh, *Nature* 1992, 359, 133.

Fast and Controlled Fabrication of Porous Graphene Oxide: Application of AFM Tapping for Mechano-chemistry

Supporting information

## 1. Large area scan of the sample in Figure 3.1.

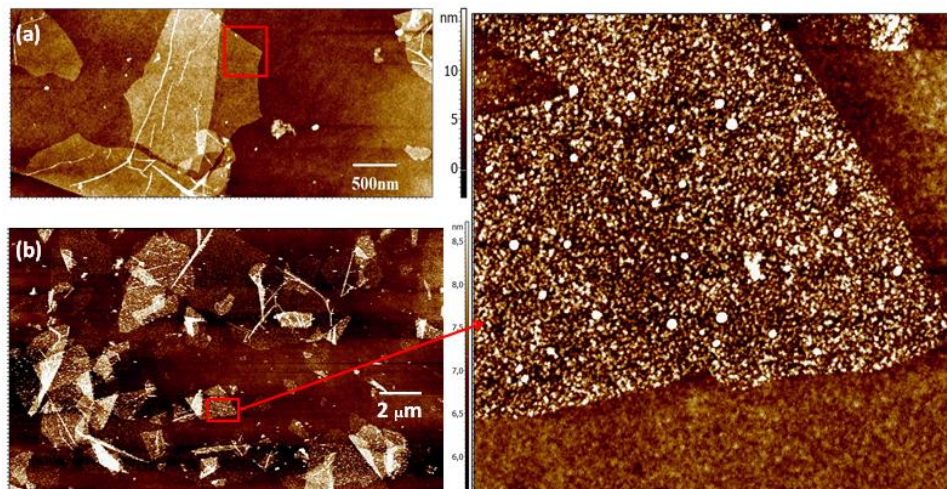
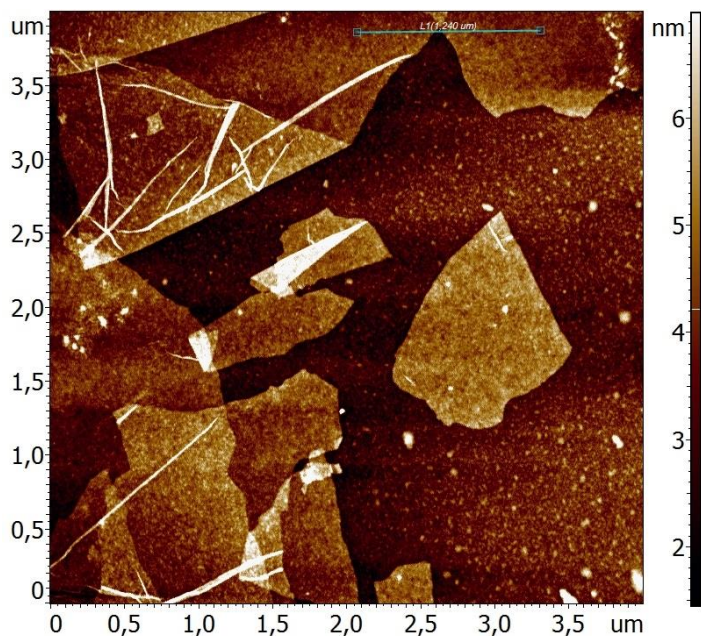


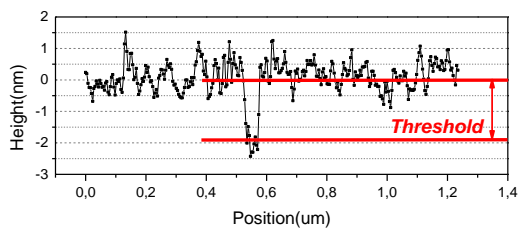
Figure S1. Additional information for Figure 3.1. A larger-area scan including Figure 3.1.c is shown in (a). A larger-area scan including Figure 3.1.g is shown in (b).

## 2. Determination the presence of pores on GO

Throughout our work, when the height of a certain area of imaged GO is lower than the height of the surrounding, we call it a well. When the height of the well is larger than a threshold value as determined by the edge height, this well is called a pore. This edge height is equal to the thickness of a GO nanosheet. However, when measured by AFM, the height of GO nanosheets varies from  $1.0 \pm 0.3 \text{ nm}$  to about  $1.5 \pm 0.3 \text{ nm}$  depending on the substrate on which the GO is deposited.<sup>[1]</sup> This is further demonstrated in chapter 2.<sup>[2]</sup> Since the number and size distribution of pores are depended on the value of the chosen threshold, this should be done with care.



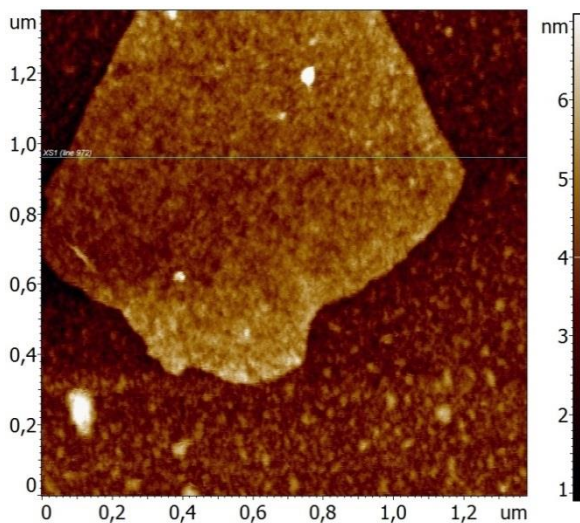
(a)



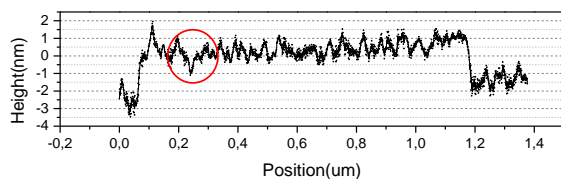
(b)

Fig S2.1 (a) AFM height image of PDADMAC/GO surface after treatment with an oxygen plasma for 9 sec. with 700 mTorr (0.93 mbar). (b) The height profile along the blue line drawn in (a).

As shown in Fig S2.1(a), a rift is created by the overlap of two GO nano-sheets and its height is used as the threshold to determine the formation of pores on GO nano-sheets. Its height profile shown in Fig S2.b clearly shows a height well with a thickness of 1.8 nm. Thus, the threshold used in the pore size analysis is calibrated to be 1.8 nm. Only when the thickness of the well on the surface of GO is equal to 1.8 nm, this specific well will be counted as a pore.



(a)



(b)

Fig S2.2. (a) AFM height image of PDADMAC/GO surface after treatment with an oxygen plasma for 9 sec. with 700 mTorr (0.93 mbar). (b) The height profile along the green line indicated in (a).

As another example, in Fig S2.2, the area that seems like to be lower than the surroundings on the height image is not counted as a pore, because the height of the well is less than the threshold. The same determination method is used in the entire work.

3. Height morphology of GO without plasma treatment and after 3sec. under  $1500 \pm 100$  mTorr ( $2.0 \pm 0.1$  mbar)

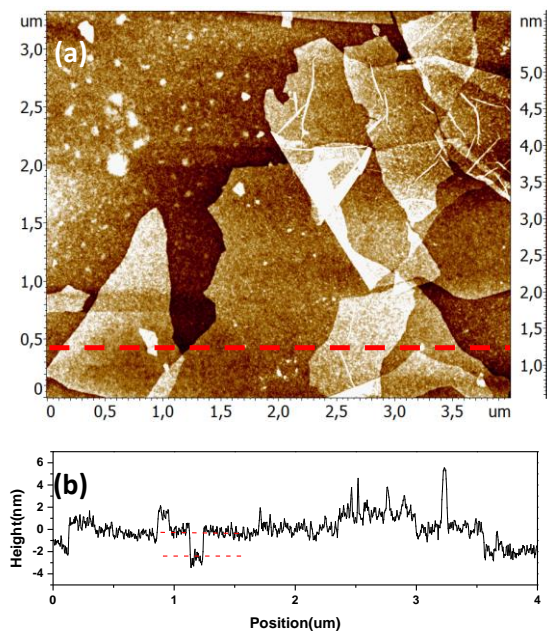


Fig S3.1. (a) AFM height image of GO/PDADMAC/Si surface without oxygen plasma treatment. (b) The height profile along the red dotted line of (a).

In Fig S3.1, we demonstrate another example showing that the non plasma treated GO surfaces do not show pores. Pores are only formed after the sample is treated by an oxygen plasma during a period longer than a certain threshold time. We conclude that these pores are formed due to the etching by the oxygen plasma rather than are already present from the original structure.

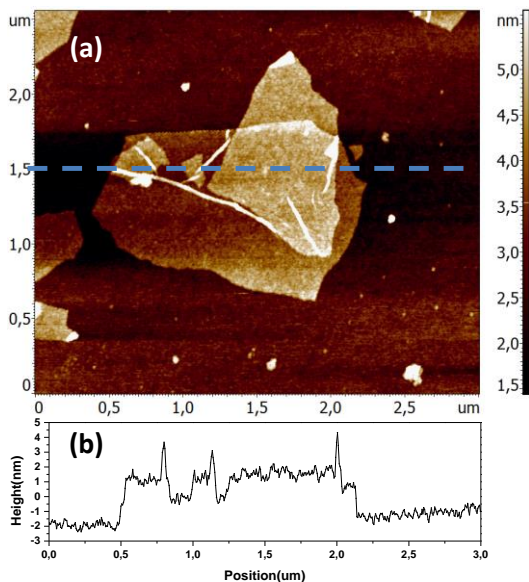


Fig S3.2. (a) AFM height image of GO/PDADMAC/Si surface after treated by an oxygen plasma for 3 sec. under  $1500 \pm 100$  mTorr ( $2.0 \pm 0.1$  mbar). (b) The height profile along the blue dotted line of (a).

In Fig S3.2 is shown that after treated with an oxygen plasma for 3 sec. under  $1500 \pm 100$  mTorr ( $2.0 \pm 0.1$  mbar) , no pores are detected on GO surface.

#### 4. Minimum of the pore size when characterized using AFM

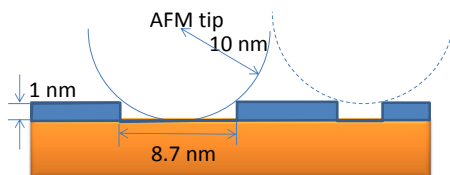


Figure S4.1. Schematic drawing of minimum pore size measured by AFM.

As shown in Fig S4.1, using AFM, only pores that are larger than a threshold size can be detected by using a tip of given dimensions. The threshold  $R_{min}$  depends on the radius of the AFM tip  $R_{tip}$  via,

$$R_{min} = \sqrt{(R_{tip})^2 - (R_{tip} - h_{GO})^2}$$

Where  $h_{GO} \approx 1$  nm is the thickness of GO. For a typical AFM tip with a radius of around 10 nm,  $R_{min}$  is about 4.3nm, for ultra-sharp AFM tip with a radius of about 2 nm, the minimum pore size is about 1.7 nm. This is consistent with our results that only pores with sizes larger than 10 nm are measured using the typical AFM tip. And with the ultra-sharp tip, smaller pores can be determined.

We notice that if the size of a pore is less than this minimum value, it will be detected as a well as shown in Figure S3.1. When its size is larger than the minimum value, the value of the size measured by AFM is the true value of its size and no correction needs to be done by taking account of the shape of the AFM tip. All the pores that are detected by normal AFM tip are larger than 9 nm, this enhances our discussion.

When scanning using a sharp tip, small pores with a radius of 2.5 nm are detected as shown in Fig 3b and c.

### 5. Details of analysing the pore size distribution using the ‘Grain method’

The pore sizes fabricated using oxygen plasma treatments are quantified using the ‘Grain method’.<sup>[3]</sup>

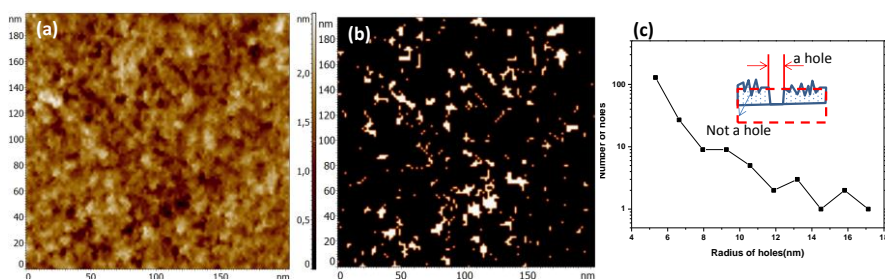


Fig S5.1 Typical pore size distribution analysis using the ‘Grain method’. (a) AFM height morphology of GO surface after being treated with oxygen plasma for 12 sec. The height of the dark areas are lower than the bright areas, which are coincident with pores. After analysis with ‘Grain method’, the areas which represent pores in (a); are shown as bright spots in (b); and their size information is recorded by the software as shown in (c).

In the ‘Grain method’, the areas that are lower than a certain threshold value are distinguished and quantified by the software. The set point is set as a depth of 1.5 nm, which means all the areas related to depths of lower than 1.5 nm are counted as pores. This is not



correct as shown in the inner figure of Fig S5.1c. According to the supporting information part 4, for a thickness of 1.5 nm, the minimum radius is calculated as 5.3 nm. Thus, all these areas related to a smaller depth than the threshold are not counted in Fig S5.1c. We should mention that this is a very rough method to calculate the area of pores.

6. Larger scan area of GO/PDADMAC/Si sample treated with an oxygen plasma during 24 sec at  $1500 \pm 100$  mTorr ( $2.0 \pm 0.1$  mbar)

As shown in the red box of Fig S6.1b, a rift is created by the overlap of two GO nanosheets and its height has been determined and is used to establish the formation of pores through GO surfaces. This is the same method as we used above for the determination of pores on GO surface in S2. The height profiles along the dashed red lines 1 and 2 show that pores are created through the nanosheets. After treatment for another 24 sec. (3 sec. oxygen plasma treatment followed by AFM characterization and equilibrium for 1 day, repeated in total by 8 times), the height morphology of the sample is shown in Figure 3.3, and the detailed scan of the area marked with red box is shown in Figure 3.3.f. The porous structure of a 48 sec. oxygen plasma treated GO sample under a pressure of 700 mTorr (0.93 mbar) (XX bar) is found to have a similar structure compared to a sample treated during 12 sec. of oxygen plasma at  $1500 \pm 100$  mTorr ( $2.0 \pm 0.1$  mbar). This demonstrates our expectation that the reaction rate depends on the pressure of oxygen plasma. After the GO surfaces are treated with an oxygen plasma at 700 mTorr (0.93 mbar) for 60 sec, more wells are developed into pores and they started to connect with each other as shown in Fig S6.2a. More detailed information is shown in Fig S8, which clearly shows the connection between the individual pores. When pores are connected with each other, GO 'peninsulas' will form. As shown in Fig S6.2d to S6.2h, after further oxygen plasma treatment, they develop into GO islands and the size of the GO islands decrease from 80 to 10 nm with increasing time. The similar evolution also occurs on bilayer GO area although with a lower speed. All these characterizations are done on different GO nano-sheets.

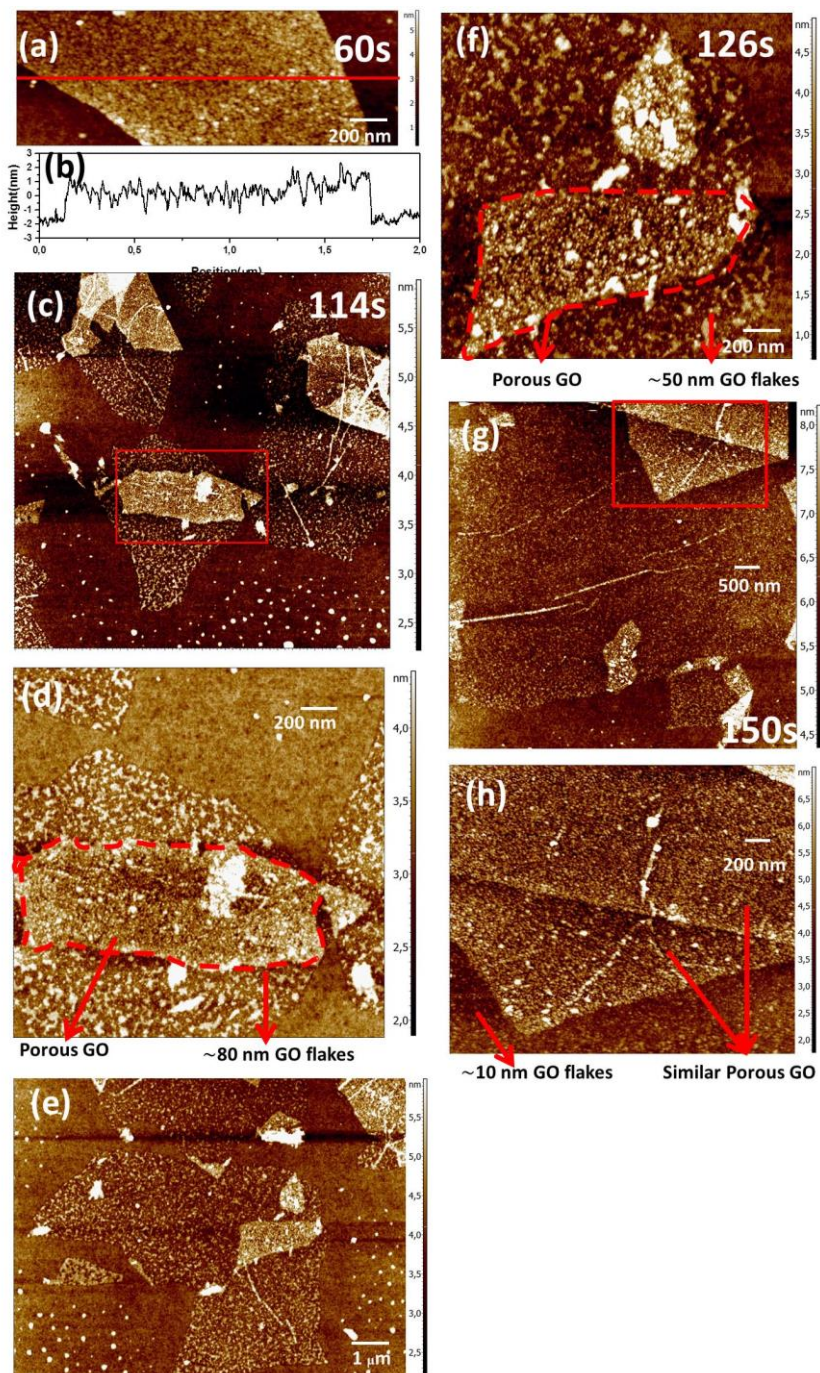


Fig S6. (a) Height morphology of a GO/PDADMAC/Si sample treated during 60 sec. by an oxygen plasma, and imaged with a normal AFM tip. (b) Height profiles of the sample along the red lines in (h). (c) Height morphology after 114 sec. oxygen plasma treatment of GO/PDADMAC/Si sample using a normal AFM tip. (d) Detailed scan of the area in the red box of (c). (e) Height morphology after 126 sec. oxygen plasma treatment of GO/PDADMAC/Si sample with a normal AFM tip. (f) Detailed scan of the area in the red box of (e). (g) Height morphology of 150 sec. treated GO/PDADMAC/Si sample with normal AFM tip. (h) Detailed scan of the area in the red box of (g).

#### 7. Height morphologies of GO/PDADMAC/Si sample characterized using sharp AFM tip

The height morphologies of GO/PDADMAC/Si sample imaged using a sharp AFM tip. We notice that before treated with oxygen plasma for 27 sec., no pores are detected on GO surface.

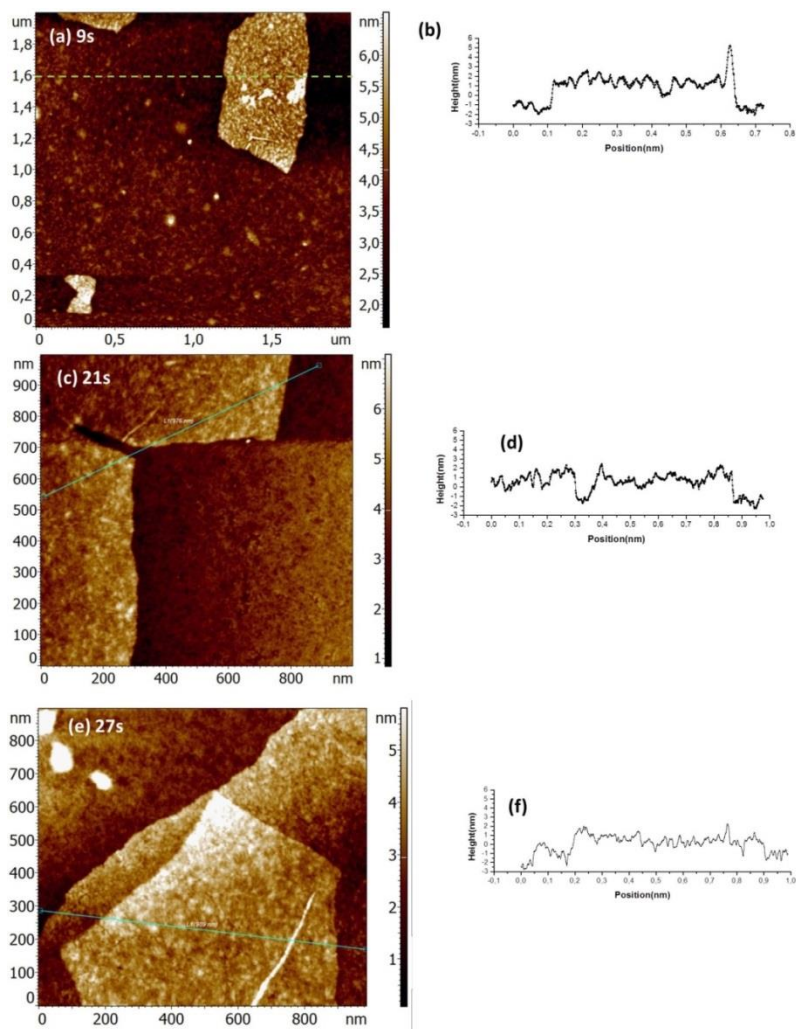


Fig S7. Height morphologies of GO/PDADMAC/Si sample imaged using a sharp AFM tip.

#### 8. Connection of pores after 60 sec oxygen plasma treatment at 700 mTorr (0.93 mbar)

As shown in Fig S8, we can see that after 60 sec oxygen plasma treatment at 700 mTorr (0.93 mbar), the pores started to connect with each other.

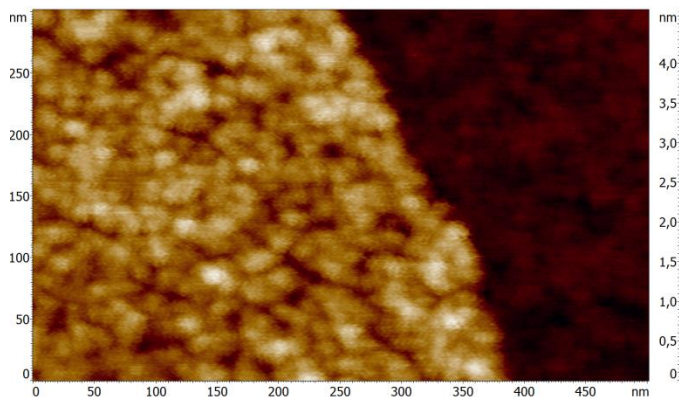


Fig S8. Detailed scan in Fig S6.a. Height morphology of a GO/PDADMAC/Si sample treated during 60 sec. by an oxygen plasma, and imaged with a normal AFM tip.

#### 9. The influence of tapping mode AFM treatment before oxygen plasma treatment.

We found that if tapping mode AFM scanning is performed before oxygen plasma treatment, no influence on the formation of PGO is detected as shown in Fig S9.

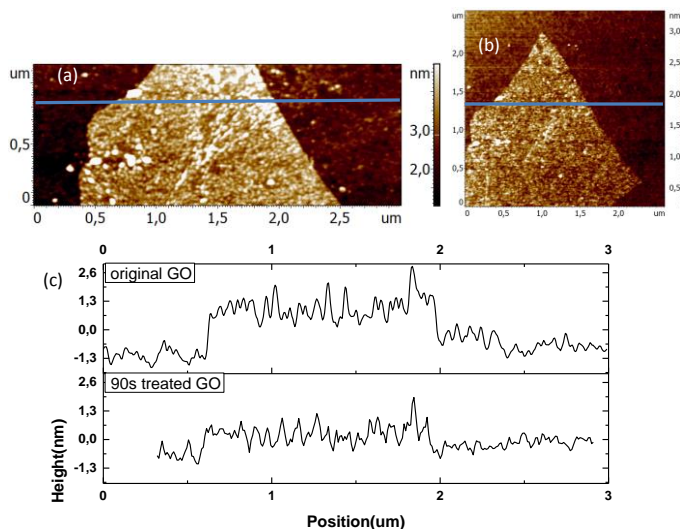


Fig S9. (a) Height morphology of GO/PDADMAC/Si sample without any oxygen plasma treatment. The area is scanned by tapping mode AFM for 3 times. On this specific GO nano-sheet, only this area in (a) is scanned. (b) Height morphology of GO/PDADMAC/Si sample after 90 sec of oxygen plasma treatment under 700 mTorr (0.93 mbar). (c) Height

profiles of the sample along the blue lines in (a) and (b). We can see that the tapping mode AFM scanning before oxygen plasma treatment has no influence on the formation of PGO.

#### 10. Substrate dependency of creating pores in GO using oxygen plasma treatment.

In practical applications of porous GO nano-sheets, GO is usually composited with other materials. Thus, the dependency of substrates needs to be studied. We found that pores are formed when GO is deposited on various substrate. This indicates that our method also applies when GO is deposited in other substrate for practical applications.

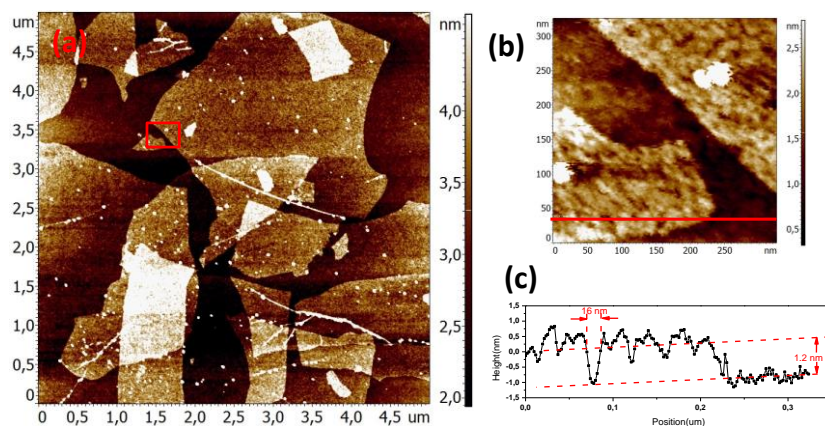


Fig S10.1 (a) AFM height morphology of hydrated GO/PDADMAC/Si sample after treatment with an oxygen plasma for 12 sec. at a pressure of  $1500 \pm 100$  mTorr ( $2.0 \pm 0.1$  mbar). (b) AFM height morphology of the area marked with red box in (a). (c) Height profile of the sample along the red line in (b).

As shown in Fig S4, a hydrated GO/PDADMAC/Si sample is prepared (the sample is not dried in the oven), after treated with oxygen plasma for 12 sec., pores are formed on GO surface. The pore size and distribution are similar with the dried sample as shown in Figure 3.1.

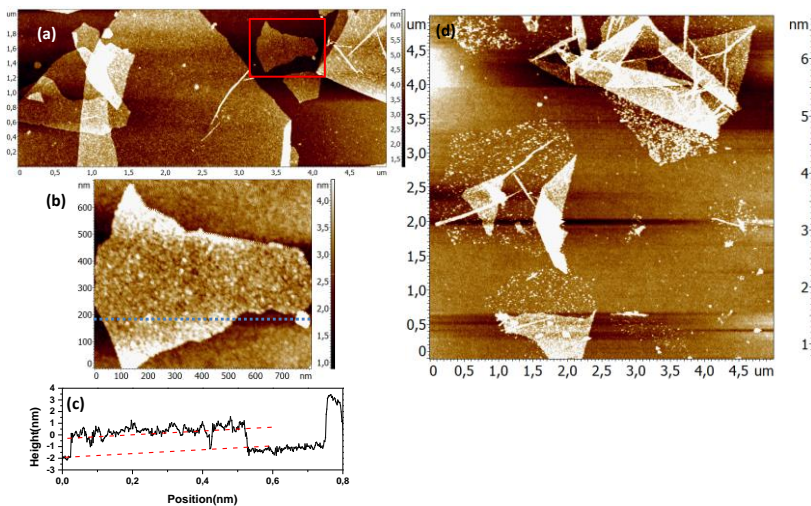


Fig S10.2 (a) AFM height morphology of dried GO/PEI/Si sample after treated with oxygen plasma for 12 sec. at a pressure of  $1500 \pm 100$  mTorr ( $2.0 \pm 0.1$  mbar). (b) AFM height morphology of the area marked with red box in (a). (c) Height profile of the sample along the blue line in (b). (d) AFM height morphology of dried GO/PEI/Si sample after treatment with oxygen plasma for 18 sec. at a pressure of  $1500 \pm 100$  mTorr ( $2.0 \pm 0.1$  mbar).

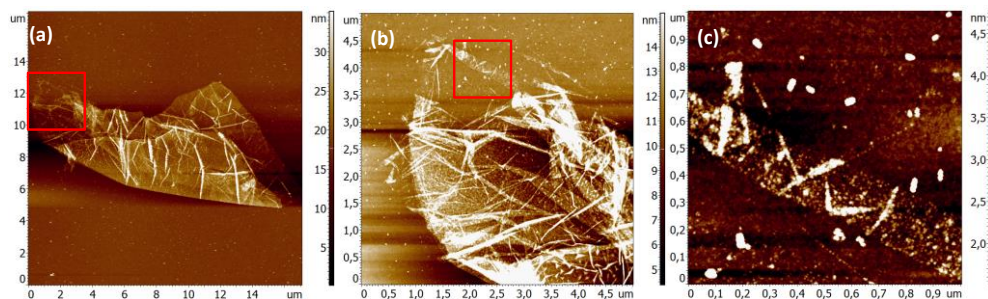


Fig S10.2 (a) AFM height morphology of dried GO/Si sample after treated with oxygen plasma for 30 sec. at a pressure of  $1500 \pm 100$  mTorr ( $2.0 \pm 0.1$  mbar). (b) AFM height morphology of the area marked with red box in (a). (c) AFM height morphology of the area marked with red box in (b). We can see that GO deposited on Si is also etched by oxygen plasma. Herein, we can also see that on pure Si wafer, only big flakes are left and the

number density is low. Thus, we choose to study on GO/PADAMAC/Si sample, as we have discussed at the beginning of our paper.

## 11. Reference

- [1] D. R. Dreyer, S. Park, C. W. Bielawski, R. S. Ruoff, *Chem. Soc. Rev.* 2010, 39, 228; K. A. Mkhoyan, A. W. Contryman, J. Silcox, D. A. Stewart, G. Eda, C. Mattevi, S. Miller, M. Chhowalla, *Nano lett.* 2009, 9, 1058.
- [2] L. Chu, A. V. Korobko, A. Cao, S. Sachdeva, Z. Liu, L. C. de Smet, E. J. Sudhölter, S. J. Picken, N. A. M. Besseling, *Adv. Mater. Interfaces* 2017, 4, 1600495.
- [3] Q. Guan, B. Norder, L. Chu, N. A. Besseling, S. J. Picken, T. J. Dingemans, *Macromolecules* 2016, 49, 8549.





# **Calibrating Lateral Force Mode AFM and Measurement of the Lateral Spring Constant**

# **4**

---

The contents of this chapter are based on :  
Chu, L.; Bus, M.; Besseling, N. A. M, Calibrating lateral force AFM and measurement of the lateral spring constant, Manuscript submitted.

### Abstract

The calibration of lateral force mode AFM (LFM) is not a straightforward process. The current methods are all laborious and might damages the probe, and sometimes probe modifications are needed. This hampers the accurate measurement of absolute values in the lateral forces AFM, an important tool in modern nanotechnology, biology and molecular science. In this chapter, we propose and demonstrate a novel and simple method to solve these problems. This method can be applied on typical commercially available AFM systems.

## 4.1 Introduction

Precise measurement of friction forces at the nanoscale is important, for both fundamental understanding and for practical applications, *e.g.* lubrication in micro(nano)-electro-mechanical systems (MEMS&NEMS).<sup>[1]</sup> Since the 1960s, various instruments including the surface force apparatus (SFA), the atomic force microscope (AFM), and the quartz crystal microbalance (QCM) have been applied to study friction at the micro- to nanoscale.<sup>[1, 2]</sup> Lateral force mode AFM (LFM), which measures the ultra-small lateral forces (varying from nN to  $\mu\text{N}$ ) between the AFM tip and the sample surface, is the most popular method in this field since it is applicable under a range of conditions.<sup>[1]</sup> A problem encountered with LFM, and as opposed to AFM normal force measurements, is that LFM is not readily calibrated. This hampers the accurate measurement of absolute values for the lateral forces.<sup>[3]</sup> We propose here a new method for determining the lateral spring constant of the probe, and calibrating the LFM. The method does not damage the probe or needs probe modification. This method can be applied to typical commercially available AFM systems.

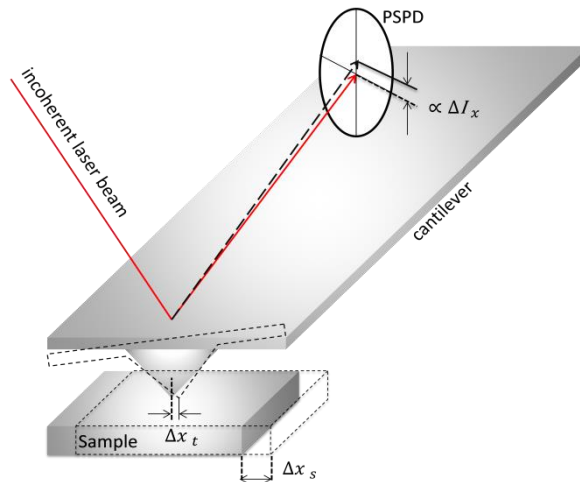


Figure 4.1. Schematic drawing of the LFM system.

Figure 4.1 shows a schematic drawing of the LFM system. The drawing is not to scale, as the actual length, width and tip height of the probe is typically  $100 - 400 \mu\text{m}$ ,  $30 - 60 \mu\text{m}$ , and  $5 - 15 \mu\text{m}$ , respectively. The distance between the probe and the position-sensitive photo detector (PSPD) is much larger than that is shown in the drawing, whereas the lateral displacement  $\Delta x_s$  of the piezo scanner and the mounted sample mounted is only  $6.102 \text{ nm}$  at maximum in the experiments described in this chapter. As the sample moves laterally by a distance  $\Delta x_s$ , the tip only displaces laterally by  $\Delta x_t$  with respect to its neutral position, as it is ‘dragged along’ by the sample. As a result the cantilever gets twisted, and exerts a lateral force on the sample, as expressed by eq. 1. The displaced positions of the sample and the tip are indicated by the dashed contours in Figure 4.1. In the sketch,  $\Delta x_t < \Delta x_s$ , which implies that a slip over a distance  $\Delta x_t - \Delta x_s$  has occurred. The sample is displaced laterally always with respect to the neutral tip position by a piezo scanner on which the sample is mounted.

For not too large lateral tip displacements  $\Delta x_t$ , the lateral force  $F_x$  exerted by the tip on the sample surface (the lateral forces on the tip and sample are identical, but with opposite signs), due to twist of the cantilever, is proportional to  $\Delta x_t$ :<sup>1</sup>

$$F_x = -K_x \Delta x_t \quad (1)$$

where the proportionality constant  $K_x$  is the lateral spring constant. So, to derive the force from a certain tip displacement, one needs to know the lateral spring constant  $K_x$ . As for the normal forces measurement, the ‘thermal-noise method’ seems a convenient way to determine the spring constant.<sup>[4]</sup> This method obtains the spring constant from the thermal fluctuations of the tip displacement. For a harmonic potential  $U_x = \frac{1}{2}K_x \Delta x_t^2$ , which is consistent with eq. 1, the mean square of the fluctuating tip displacements at thermal equilibrium is given by

$$\overline{\Delta x_t^2} = \frac{k_B T}{K_x} \quad (2)$$

---

<sup>1</sup> Note that, unlike some others, we define  $K_x$  and  $\sigma_x$  as proportionality constants between *tip displacement* and the force, and between *tip displacement* and PSPD signal.  $K_x$  defined in this way is not simply the spring constant of the cantilever, but is determined by the tip height as well. These are the proportionality constants that are actually needed in measurements of e.g. friction forces, and that will be determined by our present method.

where  $T$  is the absolute temperature, and  $k_B$  is the Boltzmann's constant. So, when we know  $\overline{\Delta x_t^2}$  from a measurement of the tip-position fluctuations, we also know the desired spring constant  $K_x$ . As recognised by Hutter et al.,  $\overline{\Delta x_t^2}$  is best determined as the integral of the resonance peak in the power spectrum density (see Supporting information 4), so that the background instrumental noise is subtracted.<sup>[5]</sup> PSD shows the strength of the variations (energy) as a function of frequency. Thus, the intergral of the PSD function equals to the driven energy. This method is used in most of the commercially available AFM instruments. As we discussed in Chapter 1.

However, the problem here is that we cannot directly measure  $\Delta x_t$  values. Rather, we measure the signal of the position-sensitive photodetector (PSPD) (see Figure 4.1)  $\Delta I_x = I_x - I_{x,0}$  where  $I_x$  is the PSPD lateral-signal readout, and  $I_{x,0}$  its mean value when no external forces, e.g. due to interactions with a sample, work on the tip. For PSPD,  $\Delta I_x$  is proportional to the displacement of the laser spot. Thus, for not too large  $\Delta x_t$ , the signal is linear in the tip displacement:<sup>1</sup>

$$\Delta I_x = \sigma_x \Delta x_t \tag{3}$$

where  $\sigma_x$  is the sensitivity coefficient.

With AFM normal-force measurements, the sensitivity coefficient is obtained from the so-called 'constant-compliance' or 'contact' region of a measured dependency of the PSPD signal vs. piezo-displacement (as shown in Chapter 1).<sup>[3, 6]</sup> In this region, the tip displacement follows exactly that of the piezo scanner on which the sample is mounted, and the sensitivity coefficient is simply the slope of the signal vs. piezo-displacement curve. For lateral-force experiments, it has so far not been possible to accurately measure something related to the constant-compliance dependency in normal-force experiments, due to the occurrence of slip of the tip over sample surfaces.

A number of publications have addressed the issue of LFM calibration. Bogdanovic *et. al.*<sup>[7]</sup> measured the torsional spring constant of a tipless cantilever by pushing it against a sharp upwards pointing tip. If the tip contacts the corner of the cantilever, the torsional spring constant can be obtained.<sup>[7]</sup> The obtained accuracy is high, but the method can only be used for tipless cantilevers. Cannara *et. al.* determined the sensitivity, by glueing a colloidal sphere to the probe and pushing the sphere against a wall to get the  $\Delta I_x$  vs.  $\Delta x$  curve.<sup>[8]</sup> Feiler *et. al.* twisted the cantilever by attaching a mass at one side using a glass fiber.<sup>[9]</sup>

These direct ways are accurate but also tedious and laborious, and they require modification of the probe or might introduce damage. Furthermore, in order to obtain the lateral proportionality constant between the force and the actual tip displacement (as in eq. 1), additional tip-height information is needed.<sup>[10]</sup> The lateral spring constant can also be calculated theoretically from the dimensions of the cantilever.<sup>[11]</sup> However, the accuracy obtained is limited due to uncertainties in the dimensions. Thus, in current friction research by using AFM methods, usually forces normalised by an unknown factor, rather than absolute forces are reported.<sup>[12]</sup> This stresses again the importance of calibration in lateral force AFM.<sup>[13]</sup>

Herein, we present a new method to calibrate lateral-force AFM. The method yields directly the proportionality constant between the lateral tip displacement and the lateral force exerted by the tip on the sample, as described in eq. 1. The method does not need further geometrical calculations. Only a clean Si wafer is needed and the method can be applied to typical commercially available AFM instruments.

## 4.2 Materials and methods

A chip of about of 1 cm × 1 cm was cut from a (100) Silicon wafer with a native oxide layer of thickness of about 2 nm and obtained from Sil'Tronix Silicon Technologies. The silicon chip was firstly rinsed with demi-water and ethanol followed by sonication using ethanol and acetone for 5 min., respectively. Oxygen-plasma treatment of a silicon chip was performed for 1 minute at a pressure of 1600 mTorr (2.1 mbar), using a Harrick plasma cleaner (Anadis Instruments). After plasma treatment, the silicon chip was stored in milli-Q water for at least 24 hours to equilibrate.

All the experiments are performed using the lateral-force mode on a SOLVER NEXT AFM instrument from NT-MDT. The standard LFM probe (PPP-LFMR) was bought from NanoAndMore GmbH, with cantilever length of 215 – 235  $\mu\text{m}$ , width of 40 – 55  $\mu\text{m}$ , and a tip height of 10 – 15  $\mu\text{m}$ .

## 4.3 Results and discussions

Figure 4.2.a shows two typical lateral-signal traces for the sliding of an AFM tip with a very low scan speed over a small distance across a silicon surface with its native oxide

layer. The normal load forces are 0 and  $-1$  nN (a negative normal load corresponds to a force pulling the tip from the surface to compensate in part for the experienced adhesion; tip-surface contact is maintained by adhesive interactions, the adhesive force between the tip and sample is about 2 nN). The small (or even negative) normal loads ensure that the tip is not damaged due to wear. We clearly recognise steps originating from the, on average, stepwise motion of the piezo scanner (the typical time of the motion is 0.02 sec.) as shown in Figure 4.2.b. With the current settings, the change of  $\Delta x_s$  from 0 to 6.10 nm in 5.00 s is achieved in 11 steps, which are clearly recognised in these averaged traces as shown in the blue and red lines in Figure 4.2.b, numbered as 1-11. So, each  $\Delta x_p$  step has a magnitude of 0.555 nm (6.10 nm for 11 steps), and the time interval between steps is 0.455 sec. (5.00 s for 11 steps). The magnitudes of the piezo-scanner steps and the time intervals are controlled by the closed-loop settings of the AFM instrument. The black line corresponds to the signal when no slip would occur at the interface between AFM tip and silica surface, so that the tip moves with the sample connected to the piezo scanner ( $\Delta x_t = \Delta x_s$ ). The  $\langle \Delta x_t \rangle$  axis on the right is constructed by realising that over the full 5 sec. the piezo displacement increases from 0 to 6.10 nm (on average), and by taking into account that for the no-slip case  $\Delta x_t = \Delta x_s$ . The vertical distance  $\langle \Delta x_t \rangle - \langle \Delta x_s \rangle$  between a measured trace and the black curve corresponds to the distance that the tip has on average slipped over the sample surface. The slope of the dashed line corresponds to the average scan speed.



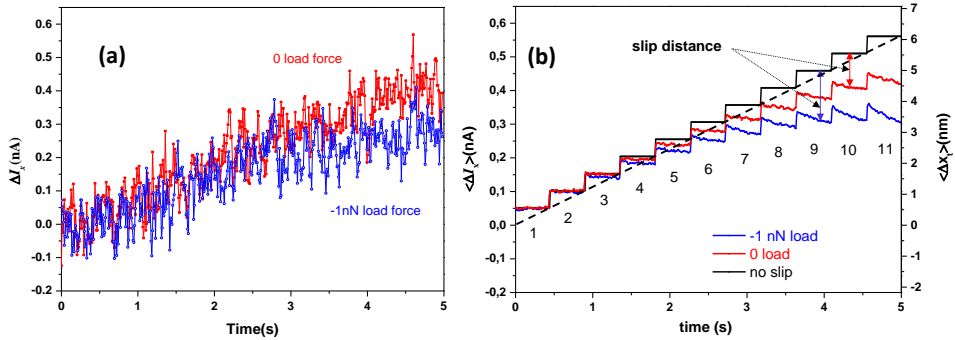


Figure 4.2. (a) The lateral signal  $\Delta I_x$  as a function of time for **single scans** with a range of 0 -6.10 nm. The scan frequency was set at 0.200 Hz, so the duration of a single scan, during which  $\Delta x_s$  varies from 0 to 6.10 nm, is 5.00 s, and the average scan speed is 1.22 nm/s. 512 points are gathered in a single scan. The feedback loop controlling the tip-sample distance was operated very slowly, to avoid any influence on the lateral signals (see Supporting information 2.).<sup>[14]</sup> (b) **Averaged data** of 512 scans at the same normal loads as in (a).

The nanometer-scale displacement of the scanner is realized by the closed-loop X–Y control of the AFM instrument, based on an independent capacitive position sensor,<sup>[15, 16]</sup> as used in most commercially available AFM systems.<sup>[16]</sup> At these low scan speeds, the piezo scanner in fact moves on average in a stepwise fashion, in which after fixed time intervals the target position of the piezo scanner changes to a new value, while the control loop tries to maintain the target position. The noise in Figure 4.2.a is due to noise of the sample position due to this control system (closed-loop X–Y control).

The scan rate here is much lower than is commonly applied for small-scale scanning and imaging. For typical nanoscale mapping much higher scan speeds (e.g. 60 Hz for a 10 nm distance scan) are needed to get a high linear position control.<sup>[17]</sup>

We see from Figure 4.2.a that, apart from the fluctuations, the lateral signal  $\Delta I_x$  initially increases linearly, and levels off later after 2-3 s. For a  $-1$  nN normal load this levelling off becomes noticeable beyond about 2 sec. For a zero normal load, levelling off occurs later and is less pronounced. It is appealing to infer that initially the lateral force  $F_x$  does not exceed the static friction force, so that the signal corresponds to the tip displacement  $\Delta x_t$  following the sample displacement, which equals  $\Delta x_s$ . This would mean that this part of the

trace is analogous to the constant-compliance region in a normal-force analysis, that the tip moves together with the sample. Hence, in principle, the sensitivity  $\sigma_x = \Delta I_x / \Delta x_t$  can be obtained from the initial slope of these traces, taking into account that the  $\Delta x_t$  increases from 0 to 6.102 nm over 5 sec. However, due to the fluctuations, which are of the same order of magnitude as the trend-like change of  $\Delta I_x$ , the relative error would be huge, as shown in Figure 4.1.a. Not using the control loop reduces the fluctuation, but leads to an unacceptable uncertainty in the lateral position (see Supporting information 1).

Figure 4.2.b shows the averaged traces of a large number of scans. We clearly recognise now the steps originating from the, on average, stepwise motion of the piezo scanner, the time interval between steps is 0.455 s. For the cases shown in Figure 4.2, the virtually vertical steps of the averaged signal  $\langle \Delta I_x \rangle$  all have the same magnitude, indicating that during the steps no slip occurs.<sup>2</sup> Hence, the change of the tip's average displacement upon a step,  $\Delta \langle \Delta x_t \rangle$ , equals the change of the average piezo-scanner displacement  $\Delta \langle \Delta x_s \rangle$  upon a step.

During the time intervals between the steps we see either a virtually constant signal, or some decay of the signal. These decays are negligible for the first intervals, but become more pronounced as the signal and hence the lateral force increases. Furthermore, these decays are more pronounced for the -1 nN normal load than for the decays for the zero normal load. These decays are obviously due to slip of the tip over the sample surface, upon which  $\langle \Delta x_t \rangle$  and hence  $\langle \Delta I_x \rangle$  decreases. In fact, these decay curves are averages over many stick-slip type events occurring in the separate scans of which Figure 4.2.b shows the average result. The reason why  $\Delta \langle \Delta x_t \rangle = \Delta \langle \Delta x_s \rangle$  for the vertical steps is that the chance of a stick-slip event occurring exactly during the phase when the average displacement of the piezo scanner changes to a new value, is negligible.

---

<sup>2</sup> That for those cases no slip occurs during the steps, so that the tip follows the sample, is essential for the further argument. There are in fact several observations that indicate that this is indeed true: If slip would occur, increase of the lateral force should increase the slip distance, and the observed step length would decrease. This is not observed. Furthermore, increase of the normal load should reduce slip, and hence increase the observed step lengths. Also this is not observed for this system. We have made tests with 'more slippery' surfaces (gold, graphene), and for those, we do observe such signatures of slip occurring during the steps.

Now we show how to calibrate the lateral spring constant  $K_x$ . As  $\Delta\langle\Delta x_t\rangle = \Delta\langle\Delta x_s\rangle$  for the vertical steps of the averaged signal we can readily calculate the lateral sensitivity coefficient  $\sigma_x$ . First we determine the change of  $\langle\Delta I_x\rangle$  corresponding to a single step of length  $\Delta\langle\Delta x_p\rangle = 0.555$  nm. By taking the average over all steps in the measurement, we find that the signal change for a single step is  $\Delta\langle\Delta I_x\rangle = 0.051 \pm 0.002$  nA. The error is calculated as the standard deviation over these steps. So we calculate the lateral sensitivity coefficient realising that  $\sigma_x = \Delta\langle\Delta I_x\rangle/\Delta\langle\Delta x_s\rangle = (0.051 \pm 0.002)$  nA/0.555 nm =  $0.092 \pm 0.004$  A/m.

The black ‘no-slip trace’ in Figure 4.2.b was constructed using this same  $\Delta\langle\Delta I_x\rangle$  value of 0.051 nA per step. The difference between this constructed no-slip trace and an experimental trace yields the distance that the tip has slipped over the surface (averaged over all scan repeats):  $\langle\Delta x_t\rangle - \langle\Delta x_p\rangle = \sigma_x(\langle\Delta I_x\rangle_{\text{exp}} - \langle\Delta I_x\rangle_{\text{noslip}})$ .

Knowing the lateral sensitivity, the lateral spring constant of the probe, as defined by eq. 1, can be readily determined, e.g. using the thermal-noise method as mentioned above. For the present case, the standard deviation of the lateral signal for the free standing probe (not interacting with any sample), at room temperature ( $T = 299.0$  K), is  $\sqrt{\overline{\Delta I_x^2}} = 1.629$  pA (see Supporting information 4). Hence, the standard deviation of the thermal lateral displacements of the tip is  $\sqrt{\overline{\Delta x_t^2}} = \sqrt{\overline{\Delta I_x^2}}/\sigma_x = 17.70$  pm. With eq. 2 we obtain  $K_x = k_B T/\overline{\Delta x_t^2} = 13.17 \pm 0.98$  N/m. The error is calculated as  $\varepsilon_{\sigma_x} \partial K_x/\partial \sigma_x$ , where  $\varepsilon_{\sigma_x}$  is the standard deviation of the sensitivity coefficient  $\sigma_x$ . Thus,  $F_x = \frac{K_x}{\sigma_x} \Delta I_x = \frac{k_B T}{\Delta I_x^2} \sigma_x \Delta I_x = (143 \pm 6) \Delta I_x$ , the error of the coefficient  $\frac{K_x}{\sigma_x}$  is determined as  $\frac{k_B T}{\Delta I_x^2} \varepsilon_{\sigma_x}$ .

#### 4.4 Conclusions

we proposes and demonstrates a novel method to calibrate the LFM system, by determining the PSPD signal dependency on the tip lateral displacement, which is analogous to the constant-compliance region in normal-force experiments. Only a clean silicon wafer is needed and it works on typical commercial AFM. No damage or modification of the AFM

probe is involved and only a clean silicon wafer is needed. It readily works on typical commercially available AFM systems.

#### 4.5 References

- [1] J. N. Israelachvili, *Intermolecular and surface forces*, Academic press, 2011.
- [2] B. Bhushan, J. N. Israelachvili, U. Landman, *Nature* 1995, 374, 13.
- [3] H.-J. Butt, B. Cappella, M. Kappl, *Surface science reports* 2005, 59, 1.
- [4] H.-J. Butt, M. Jaschke, *Nanotechnology* 1995, 6, 1.
- [5] J. L. Hutter, J. Bechhoefer, *Review of Scientific Instruments* 1993, 64, 1868.
- [6] W. A. Ducker, T. J. Senden, R. M. Pashley, *Nature* 1991, 353, 239.
- [7] G. Bogdanovic, A. Meurk, M. W. Rutland, *Colloids and Surfaces B: Biointerfaces* 2000, 19, 397.
- [8] R. J. Cannara, M. Eglin, R. W. Carpick, *Review of Scientific Instruments* 2006, 77, 053701.
- [9] A. Feiler, P. Attard, I. Larson, *Review of scientific instruments* 2000, 71, 2746.
- [10] H. Wang, M. L. Gee, *Ultramicroscopy* 2014, 136, 193.
- [11] E. Liu, B. Blanpain, J.-P. Celis, *Wear* 1996, 192, 141; C. P. Green, H. Lioe, J. P. Cleveland, R. Proksch, P. Mulvaney, J. E. Sader, *Review of Scientific Instruments* 2004, 75, 1988.
- [12] J. S. Choi, J.-S. Kim, I.-S. Byun, D. H. Lee, M. J. Lee, B. H. Park, C. Lee, D. Yoon, H. Cheong, K. H. Lee, *Science* 2011, 333, 607.
- [13] A. Bylinskii, D. Gangloff, I. Counts, V. Vuletić, *Nature materials* 2016; H. Vinutha, S. Sastry, *Nature Physics* 2016, 12, 578.
- [14] A. Socoliuc, R. Bennewitz, E. Gnecco, E. Meyer, *Physical review letters* 2004, 92, 134301.
- [15] H. Philipp, Google Patents, 2001.
- [16] Wikipedia, 2016.
- [17] B. Bhushan, O. Marti, in *Springer handbook of nanotechnology*, Springer, 2010, 573.

Calibrating lateral force mode AFM and measurement of the lateral spring constant

Supporting information

## 1. Original data

For the present purpose it is necessary to ensure the accuracy of the lateral piezo displacement by using a closed-loop control. Such a closed-loop control, based on an independent capacitive position sensor, is available with most commercially available AFM instruments. In a ‘linear’ scan, using this closed-loop control, the target displacement in fact varies in a step-wise manner, while the feedback loop tries to maintain that target position as closely as possible. As a result, for very slow scans, as applied in the present study, the lateral piezo scanner moves on average stepwise, whereas a single scan exhibits considerable fluctuations due to the control loop, so that the steps are barely recognisable (e.g. main text, Figure 4.2.a). Still, by taking an average over a sufficient number of repeated scans, one can accurately determine the average magnitude of the change of the signal  $\Delta\langle\Delta I_x\rangle$  upon a piezo-scanner step, as shown in Figure 4.2.b of the main text. For cases without slip, the change of the lateral tip displacement equals that of the piezo scanner on which the sample is mounted. Hence the sensitivity coefficient defined by eq. 3 of the main text can be determined as  $\sigma_x = \Delta\langle\Delta I_x\rangle/\Delta\langle\Delta x_s\rangle$ . On the SOLVER NEXT AFM instrument from NT-MDT, used in the present study, the magnitude of the steps can be changed via the control-software user interface.

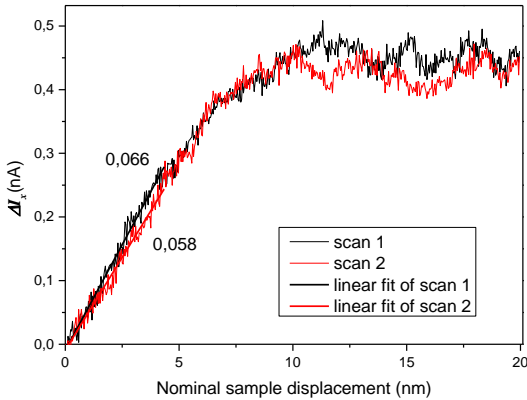


Fig S1. Lateral signal with open-loop control. The scan range was 20 nm and the scan rate was 0.2 Hz. We can see that with open-loop control, the noise of the signal is much smaller than with the closed loop control. However, the ‘nominal sample displacement’ assumes a

constant sample speed. It is known that there are always deviations from this constant speed, especially at the beginning and at the end of a scan. This would lead to systematic errors in the determination of the sensitivity coefficient from the initial slope of curves like these. Hence, to ensure accurate control of the lateral position, the control loop based on a capacitive position sensor is essential for the present purpose.

Some typical examples of images produced by the standard NT-MDT software (Nova Px 3.2.5), as a result of the slow scanning experiments, are shown in Fig. S2. As the software was not intended for the kind of experiments described in the present letter, the output generated by the standard software can be somewhat confusing at first sight. This is explained further in the caption of Fig. S2.

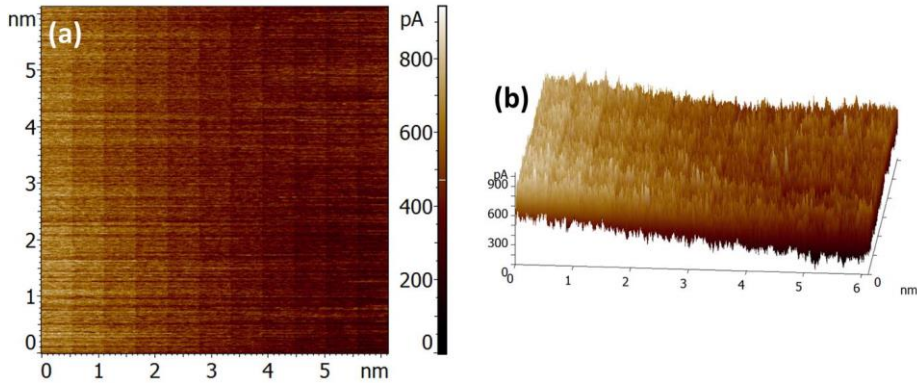


Fig S2. Images generated by the standard NTM-DT software (Nova Px 3.2.5). (a) The scan frequency is 0.2 Hz, and the scan range is set at 10 nm. As a consequence of the chosen step-length setting, the control software sets the true scan range to 6.10 nm, in order to achieve an integer number of steps. The image S2.a represents 512 repeated scans along the same line at a silica surface. The visual pattern reflects the step like law of the averaged signal as shown in Fig. 4.2.b. The horizontal axis, represented by the software as a distance axis, is in fact a false distance axis at this very slow scan rate. The software presumes a linear relation between elapsed time and distance and automatically substitutes the time axis by a distance axis on that basis. In fact, the horizontal axis is a time axis, as in Fig. 4.2 of the main text. Also the vertical distance axis is not a true distance axis. Rather than a distance, the scan-repeat number varies in the vertical direction. By plotting all 512 repeat scans together, the step-wise pattern becomes visually recognisable as vertical bands. (b) 3D representation of (a). These images represent the same experimental data as used in Fig. 4.2 (-1 nN load force) of the main text.

## 2. Influence of the feedback loop in the normal direction

As mentioned in ref. <sup>[1]</sup>, details of the control settings for the normal cantilever deflection, which controls the normal load, is relevant for the success of lateral-force measurements. The voltage on the piezo scanner for the vertical displacement of the cantilever base is controlled by a (proportional–integral–derivative) PID control algorithm fed by the difference between the target cantilever deflection and the actual cantilever deflection, as measured by the normal signal of the PSD. In order to minimise the influence of this feedback on the measurement of the lateral forces, the proportional gain and the differential



gain were set to 0, and the integral gain to a small value, in order to make the feedback very slow. Fig. S3 shows some examples and tests for some different values of this integral gain parameter. Large negative values of the signal  $I_x$  correspond to large lateral forces. We found that when the value of the integral-gain parameter for the normal direction is larger than 0.3, a regular oscillatory signal is recorded for the lateral direction. When the integral gain parameter is reduced to 0.1, the signal trace exhibits a decreasing trend, which indicates an increasing lateral force. There are however fluctuations, as discussed in the main text. When the integral gain is decreased further, no further change to the signal traces is detected. With all experiments of the present letter, the integral-gain parameter for the normal cantilever deflection was set at 0.01.

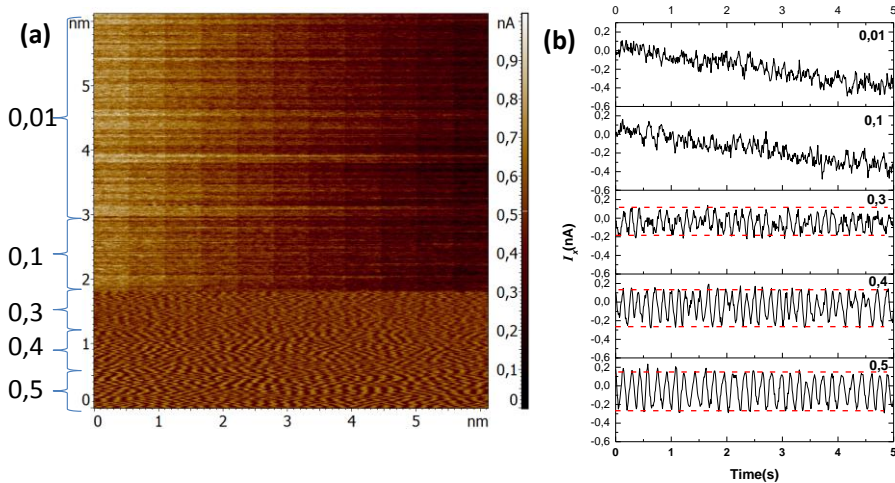


Fig S3. Tests of the influence of the feedback loop controlling the normal cantilever deflection, by varying the integral-gain value, keeping the proportional and differential gains at 0. (a) Repeated scans at 0 normal load as in Fig. S1.a and b, and in Figure 4.2. The integral gain is varied from 0.5 to 0.01 (values are indicated on the left of the image). (b) typical single-scan profiles for the different values of the integral gain.

### 3. LFM calibration based on the dimensions of the setup

A typical calibration method that is sometimes used in AFM lateral force studies is based on the dimensions of the setup:<sup>[2]</sup>

$$F_x = \frac{l^2 K_z}{4l_{tip}LB} \Delta I_x$$

where  $F_x$  is the frictional force and  $I_x$  is the lateral signal of the position-sensitive photo detector (PSPD). Furthermore,  $l$  is the length of the cantilever,  $l_{tip}$  is the height of the tip,  $L$  is the optical arm, which is the optical distance between the backside of the cantilever and the PSPD, which is 35 mm for our instrument.  $K_z$  is the normal spring constant, which can, in principle be calculated from the probe dimensions and the modulus  $E$  of the cantilever material:

$$K_z = \frac{Ewt^3}{4l^3}$$

where  $w$  is the width, and  $t$  the thickness of the cantilever.<sup>[3]</sup> In practice, this thickness is not perfectly homogeneous and difficult to determine. Rather than calculating  $K_z$  from the probe dimensions like this, it is more accurate to really measure it using the thermal-tune method.<sup>[4]</sup> The normal spring constant of the cantilever used in the present study was determined in this way as  $K_z = 0.18$  N/m. Parameter  $B = dI_x/db$ , where  $b$  is the lateral laser spot displacement on the PSPD. Thus,  $B$  can be determined as

$$B = \frac{\Delta I_x}{\Delta \eta \cos \theta}$$

Where  $\theta$  is the slope angle of the laser reflected by the cantilever ( $20^\circ$  for our instrument). The ratio  $\Delta I_x/\Delta \eta$ , where  $\eta$  is the displacement of the PSPD, is obtained from the measured calibration curve shown in Fig. S4 as  $0.0703$  nA/ $\mu\text{m}$ , so  $B = 0.0748$  nA/ $\mu\text{m}$ .

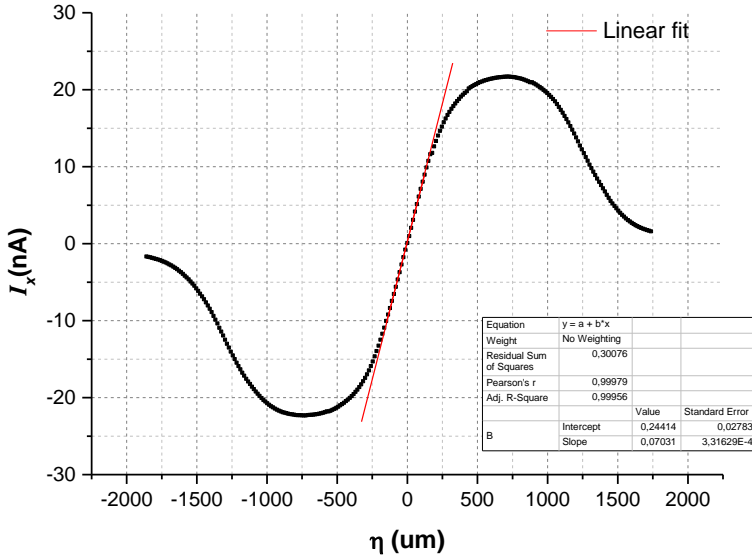


Fig S4. Determination of the sensitivity of the PSPD with respect to laser-spot displacement. Keeping the laser at a fixed position, the PSPD is moved in the lateral direction, and the lateral signal is recorded.  $\eta$  is the lateral displacement of the PSPD.

By using the values for the probe provided by the producer,<sup>[5]</sup>  $l = 225 \text{ } \mu\text{m}$ ,  $l_{tip} = 12 \text{ } \mu\text{m}$ , the LFM system is calibrated as:  $F_x/\Delta I_x \approx 72 \text{ nN/nA}$ .

Using the direct calibration method introduced in our present letter, we find that rather  $F_x/\Delta I_x = 14.2 \pm 0.6 \text{ nN/nA}$ . This demonstrates that the calculation based on the on the system dimensions yields a result that is of the right order of magnitude, but that is not very accurate.

#### 4. Determination of $\overline{\Delta x_t^2}$

To determine the  $\overline{\Delta x_t^2}$  due to thermal fluctuations, in principle we could directly use the measured lateral fluctuations of the  $\Delta I_x^2$  and the sensitivity  $\sigma_x$ . However, this would not be accurate since the measured  $\Delta I_x^2$  includes contributions due to normal cantilever fluctuations (see Fig. S4) and noise from the instrument, which can never be avoided. As recognised by Hutter et al.,<sup>[6]</sup> in the context of the determination of the normal spring

constant from the normal thermal fluctuations, it is much better to calculate the mean square thermal fluctuations as the integral of the resonance peak of the of the power spectrum density (PSD) of the thermal fluctuations. None of the other noise sources is likely to have a peak at this frequency. Thus, they only add a background to the response, and perhaps to some peaks at other frequencies that can be discarded in the integration.

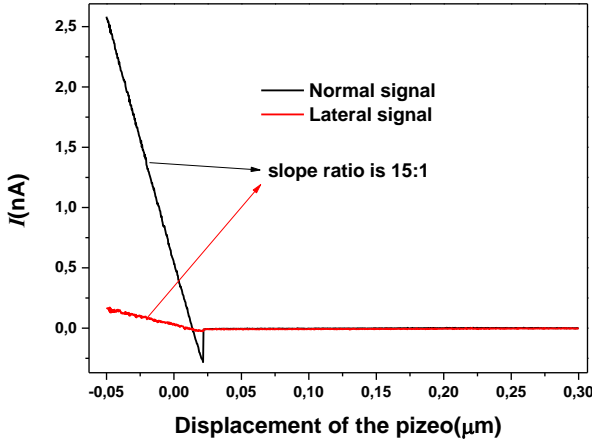


Fig S5. Measured dependencies of both the normal signal  $I_z$  and the lateral signal  $I_x$  upon variation of the normal displacement  $\Delta z$  of a hard surface. We see that the lateral signal has some sensitivity to the normal cantilever deflection. The ratio of the slopes of  $I_x$  vs.  $\Delta z$  and of  $I_z$  vs.  $\Delta z$  in the constant compliance region is 1:15.

In order to enable the acquisition of the high frequency fluctuations using our AFM setup, the lateral signal of the freely fluctuating cantilever is recorded via a synchronous detector (SD). This is available on most commercial AFM systems. Its use for the analysis of thermal cantilever fluctuations was suggested before in the context of the thermal noise method for the normal spring constant.<sup>[7, 8]</sup> The SD shifts the frequency spectrum of the signal to lower values, posing less stringent requirements on the fastness of the measuring system.<sup>3</sup> The data acquisition system records a time series of  $N = 1024$  signal values over a time segment  $t$ , with regular time intervals  $\Delta t = t/N$  (so, the sample frequency is  $f_s = \Delta t^{-1} = N/t$ ). This series of data points is fed through a fast Fourier transform (FFT)

<sup>3</sup> The spectra in figs. S6 and S7 are ‘corrected back’ for this shift due to the SD.

algorithm to yield the FFT spectrum  $F(f)$ , a software option that is available on most commercial AFM systems. The frequency resolution ( $=$  the frequency bin width) is  $f_{res} = f_s/N = \tau^{-1}$ . The maximal frequency that is probed in this way is the Nyquist frequency  $f_{Ny} = f_s/2$ , so one should ensure that this exceeds the frequency range that one is interested in. Fig. S6 shows the FFT spectra both for the normal-signal fluctuations and for the lateral-signal fluctuations. The resonance frequency in the normal direction is 31.7 kHz and the resonance frequency in lateral direction is 298.6 kHz. This is determined from the spectrum of a ‘mechanically driven’ cantilever.

The *PSD* is determined as

$$PSD = F(f)^2 / f_s.$$

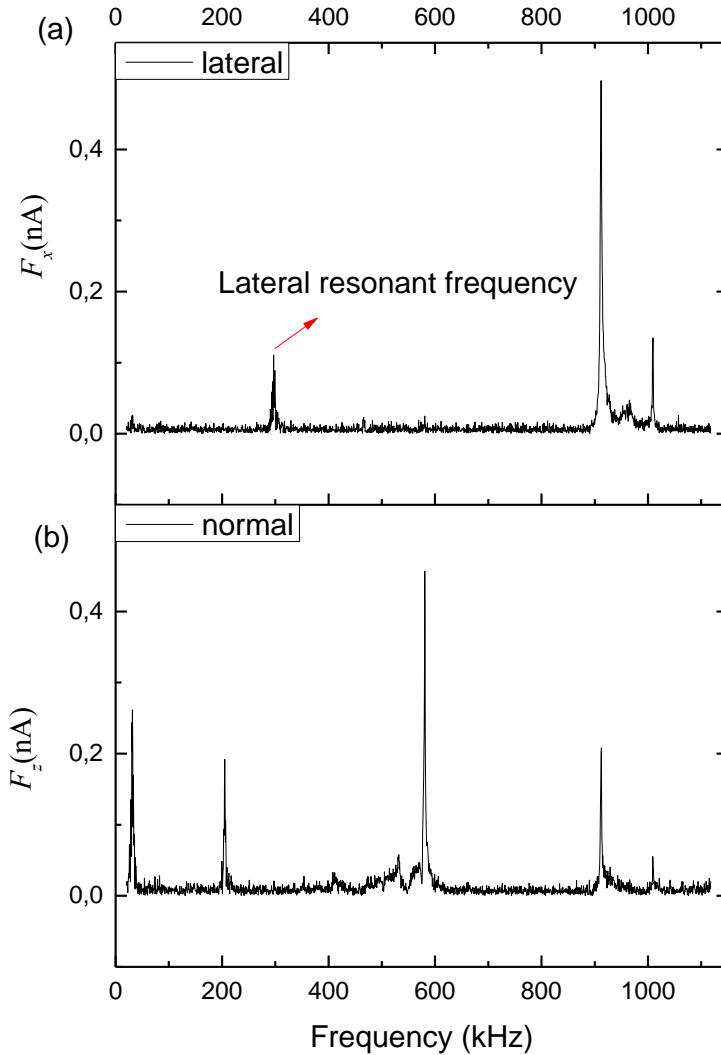


Fig S6. Determination of the lateral resonance frequency. (a) is the FFT spectrum of the lateral signal, and (b) is the power spectrum of the normal signal over a range of 20 Hz – 1.5 MHz. Three lateral response peaks are clearly recognised. At  $\sim 900$  kHz and  $\sim 1000$  kHz we observe peaks in the lateral as well as in the normal signals. We find that the peak in the lateral signal around 298.6 kHz corresponds to the lateral resonance frequency.

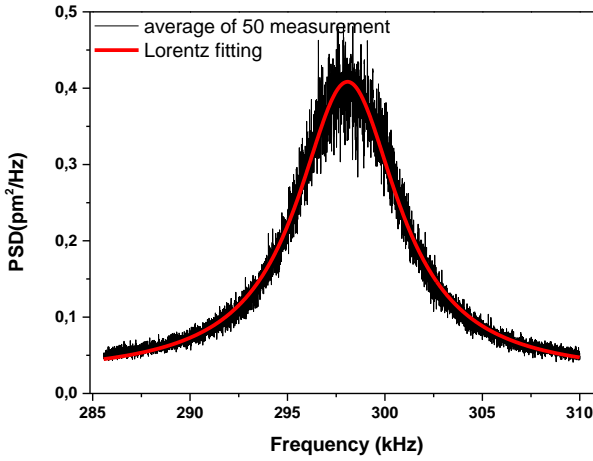


Fig S7. PSD of the lateral thermal tip fluctuations  $\Delta x_t$  around the lateral resonance frequency. The lateral PSD signal  $\Delta I_x$  was converted to lateral tip displacement  $\Delta x_t$  using the lateral sensitivity coefficient obtained in the main text. The black line shows the average of 50 measurements and the red curve is the Lorentz fitting.

As usually observed as well with normal cantilever fluctuations, the power spectrum density of the lateral fluctuations has a Lorentzian line shape (see Fig. S7). By fitting the power spectrum at the resonant frequency using a Lorentzian line shape,  $\overline{\Delta x_t^2}$  (or  $\overline{\Delta I_x^2}$ ) can be determined as its integral.<sup>[6, 7]</sup> In our case,  $\overline{\Delta I_x^2}$  is determined as  $26.50 \text{ pA}^2$ , thus  $\overline{\Delta x_t^2}$  is determined as  $(3.2 \pm 0.1) * 10^{-21} \text{ m}^2$  as shown in Fig. S7. The error is determined by  $\frac{\overline{\Delta I_x^2}}{\sigma_x^3} \varepsilon_{\sigma_x}$ .

## 5. References

- [1] A. Socoliuc, R. Bennewitz, E. Gnecco, E. Meyer, Physical review letters 2004, 92, 134301.
- [2] Q. Li, T. E. Tullis, D. Goldsby, R. W. Carpick, Nature 2011, 480, 233.

- [3] E. Tocha, H. Schönherr, G. J. Vancso, *Langmuir* 2006, 22, 2340; M. Reguzzoni, M. Ferrario, S. Zapperi, M. C. Righi, *Proceedings of the National Academy of Sciences* 2010, 107, 1311.
- [4] Y. Liu, I. Szlufarska, *Physical review letters* 2012, 109, 186102.
- [5] O. Braun, I. Barel, M. Urbakh, *Physical review letters* 2009, 103, 194301.
- [6] P. Bak, C. Tang, K. Wiesenfeld, *Physical review letters* 1987, 59, 381.
- [7] I. Malovichko, *Bulletin of the Russian Academy of Sciences: Physics* 2013, 77, 972.
- [8] K. C. Neuman, A. Nagy, *Nature methods* 2008, 5, 491.





# **AFM Study of Lubrication of Graphene Oxide by Water**

# **5**

---

The contents of this chapter are based on :  
Chu, L.; Korobko, A. V.; Besseling, N. A. M, AFM study of lubrication by water of the Graphene oxide surface,  
Manuscript submitted.

### Abstract

We present results from AFM-lateral force experiments demonstrating that the graphene oxide (GO) surface can be effectively lubricated by a few layer of water molecules. The hydrophilicity, atomically flat and non-swelling nature of GO enables to bind a 2-4 nm thick hydration film, which allows for efficient lubrication. This rather unique property may lead to new applications of GO, such as nano-mechanical devices and surface coatings for use in (aqueous) biomedical systems, where oil-based lubrication is not desired.

## 5.1 Introduction

Friction between solid surfaces, and the reduction of friction by lubrication are ubiquitous phenomena. They are relevant in fields as diverse as geology and environmental science, biology, mechanical engineering and nanotechnology.<sup>[1]</sup> Moreover, control of friction is crucial in many technological applications. Friction depends on surface properties such as interfacial adhesion, roughness, chemical heterogeneity, and stiffness, and on the presence of intermediate additives ('lubricants').<sup>[2]</sup>

Lubricants in technological applications are usually oil-based, as most metal and polymer surfaces are lipophilic.<sup>[3]</sup> However, achieving lubrication in an aqueous environment is becoming increasingly urgent, *e.g.* for nanotechnology, and in bio-medical applications.<sup>[4]</sup> In living systems, effective water-based lubrication has developed over thousands of years of natural selection, *e.g.* in the bone joints, the aqueous lubricant layers are stabilized by polyelectrolytes based on an osmotic mechanism.<sup>[4]</sup> Usually, water-based lubrication is achieved by means of additives, *e.g.* colloidal particles to the aqueous fluid.<sup>[5]</sup> Such additives are prohibited in the above mentioned applications. Creating artificial surfaces for which water itself acts as a lubricant, without any further additions, is challenging. A nice illustration of water itself acting as a lubricant is the ant-eating pitcher plant.<sup>[6]</sup> When the rim of their pitfall traps gets wet, a super-lubricating water film forms, causing ants to slide to their doom.

Our theory (by N.A.M. Besseling) of hydration forces between surfaces predicts that if the main effect of a surface is to influence the orientational distribution in adjoining water layers, the interfacial force due to the presence of the adsorbed water layers will be repulsive and efficient lubrication by water occurs.<sup>[7]</sup> On the contrary, if the predominant effect of the surface is to influence the local density of the adjoining water layers, the interfacial force will be attractive and no water lubrication occurs.<sup>[7]</sup> Thus, to render water an effective lubricant, the surface needs to be hydrophilic in order to bind a hydration film, and it needs to be atomically smooth, to effectively influence the orientation of the interfacial water and to avoid any direct contact between solid protrusions. Thus, only a limited number of surfaces are readily lubricated by only water, including some kind of hydrophilic and atomically flat ceramics, and mica.<sup>[8]</sup> For practical applications, surface coatings that can lead to lubrication by water are needed. There is only one example of water lubrication surface coating described in literature by Briscoe et al.<sup>[9]</sup> They found that

the friction, between two sliding mica surfaces, both bearing surfactant monolayers, decreased significantly by the presence of water. This was explained by a shift of the slip plane from the interface where the apolar tails meet, to the interface between the surfactants and the mica substrate. Due to the water film formed at this interface, the local friction reduces. However, this observation cannot be readily translated into an approach to design a stable surface or a surface coating for water lubrication. Contemplating on what materials may be suitable candidates for such a desired coating, graphene oxide (GO) seems to satisfy the needed requirements. This is because of its atomically flat nature and hydrophilic surface<sup>[10]</sup> In addition, (as is discussed in the supporting information, section II) GO can be applied as a stable coating to various artificial surfaces. Recent research has reported that the friction between steel balls decreases in the presence of a GO coating on these balls<sup>[11]</sup> <sup>[12, 13]</sup> and also if GO was added to the aqueous medium<sup>[14]</sup>. This confirms our hypothesis that GO may be a suitable candidate for coating to induce lubrication by water. However, in these macroscale experiments, the contributions of GO to water lubrication are regarded as a protecting layer to avoid direct contact between solid protrusions.<sup>[13]</sup> In order to demonstrate that the GO surface itself is lubricated by water, more work needs to be done which is focused on the nanoscale.

GO, known for already 150 years, has resurged recently, as intermediate to fabricate graphene and graphene derivatives.<sup>[15, 16]</sup> Although GO has been applied in various areas as a replacement of *e.g.* surfactants or poly-electrolytes,<sup>[16]</sup> it is regarded not as unique as graphene, which compound has more distinctive electrical and mechanical properties.<sup>[17]</sup> However, GO does have certain unique features that can distinguish itself from other 2D materials: GO is quite hydrophilic due to the present polar moieties formed during the oxidation of the graphite precursor<sup>[15, 18]</sup> The compound is also nearly atomically flat, owing to the present graphene domains<sup>[18, 19]</sup> The rigid covalent structure avoids swelling in water, in contrast to the properties of hydrophilic polymers. These properties make that on GO a stable and oriented hydration layer can be formed, which may contribute to repulsive interfacial forces, and in that way to lubrication by water.

In order to test this expectation, we have investigated by lateral force microscopy (LFM) the friction forces between both dry and hydrated GO and a silicon surface carrying a thin native oxide layer. As substrate we coated a chip from a silicon wafer (with its natural oxide layer) by means of a layer-by-layer strategy.<sup>[20]</sup> First, it was coated with a layer of the

cationic polyelectrolyte poly(diallyldimethylammonium chloride) (PDADMAC). Then, GO, which is predominantly anionic, was deposited on top of the adsorbed PDADMAC layer. The tip on the cantilever was made of silicon with a thin native oxide layer.

## **5.2 Experimental Section**

### **5.2.1 Chemicals and materials**

Graphene oxide (GO), synthesized using Hummer's method, was purchased from Graphene Supermarket. A stable dispersion of 0.5 g GO in 1 L Milli-Q water was prepared using ultrasonication for 1 h (USC-TH ultrasonic bath, VWR Scientific). The dispersion was then centrifuged at 4000 rpm for 1 h, using a Megafuge 2.0R centrifuge from Heraeus Instruments with a rotor radius of 20 cm. The supernatant was decanted and used for the sample preparation. Poly(diallyldimethylammonium chloride) (PDADMAC,  $M_w = 200\sim 350$  kg/mol) was purchased from Sigma-Aldrich and used as received. A 0.1 g/L aqueous solution of PDADMAC was prepared using milli-Q water. A chip of about of 1 cm  $\times$  1 cm was cut from a (100) Silicon wafer (from Sil'Tronix Silicon Technologies) with a native oxide layer of about 2 nm. The silicon chip was firstly rinsed with demi-water and ethanol followed by sonication in ethanol and acetone for 5 min., respectively. Plasma treatments of samples were performed with oxygen plasma for 1 min. at a pressure of 1600 mTorr (2.1 mbar)(Harrick plasma cleaner, Anadis Instruments). After plasma treatment, the silicon wafer was stored in milli-Q water for subsequent sample preparation.

### **5.2.2 Sample preparation**

The Si surface (with its native oxide layer) was coated with a monolayer of PDADMAC by dipping the Si chip in an aqueous PDADMAC solution (0.1 g/L) for 15 min. The sample was then rinsed in Milli-Q water for 5 min to remove any non-adsorbed PDADMAC. Subsequent coating by GO was done by immersing the sample for 15 min in the aqueous GO dispersion prepared as described above. To remove any excess of GO, the sample was dipped in Milli-Q water for 5 min. Due to the present dissociated carboxylic acid groups, GO is negatively charged and adsorbs readily on the positively charged PDADMAC polymer. All these modification steps were done whilst the solution was stirred.

After deposition, the sample was dried at 70 °C for 3 h. in oven and then exposed to air in the closed NT-MDT Solver Next AFM cell with a relative humidity of about 60% at room temperature for 14 days to get equilibrium.

### 5.2.3 Instrumentation and methods

A SOLVER NEXT AFM instrument from NT-MDT was used in all AFM experiments.

A PPP-LFMR silicon tip purchased from NanoAndMore, with nominal value for the tip radius of 7 nm (guaranteed < 10 nm) and a nominal spring constant of 0.2 N/m was used for the tapping mode and lateral force mode measurements. The actual value of the normal spring constant  $k_n$  was measured using the thermal noise method,<sup>[21]</sup> and found to be 0.086 N/m. The standard tapping-mode height images and the lateral-force images were all scanned with a rate of 1.5  $\mu\text{m/s}$ .

For lateral force mode AFM, the lateral force  $F_x$  acting along the moving direction is proportional to the measured lateral signal  $\Delta I_x$  (as detected by the photodiode, and measured in units of pico Ampere (pA) via<sup>[22]</sup>

$$F_x = \frac{l^2}{4l_{\text{tip}}SBC} \Delta I_x$$

where, the rectangular cantilever has a length  $l$ , a width  $w$ , and a thickness  $t$ , ending with a tip having a height measured from the cantilever of  $l_{\text{tip}}$ .  $S$  is the optical arm length, which is the distance between the mirror (at the back of the cantilever) and the photodiode.  $B$  is the calibration constant of the optical detection system.<sup>[22]</sup>  $1/c$  characterizes the cantilever stiffness (0.086 N/m) and it is related to the cantilever dimensions as

$$c = \frac{4l^3}{Ewt^3}$$

where  $E$  is the Young's modulus of the cantilever material. For our system,

$$F_x [\text{pN}] \approx 11 \Delta I_x$$

### 5.3 Results and discussions

Before the AFM measurements were performed, the sample was equilibrated in a closed cell at a relative humidity of about 60% for 2 weeks. Figure 5.1 shows the morphology of the PDADMAC/GO-coated sample as obtained by tapping mode AFM. GO flakes are

clearly recognizable. In the images of Figure 5.1.a and b they appear as relatively bright patches with a thickness of about 1.5 nm. In Figure 5.1.a, which is scanned using the tapping mode, we observe bright spots with heights in the order of 2-4 nm, and sub-micrometer lateral sizes. These occur both on GO and on PDADMAC. During tapping-mode scanning, the interaction force between the AFM tip and the sample is normal to the sample surface.

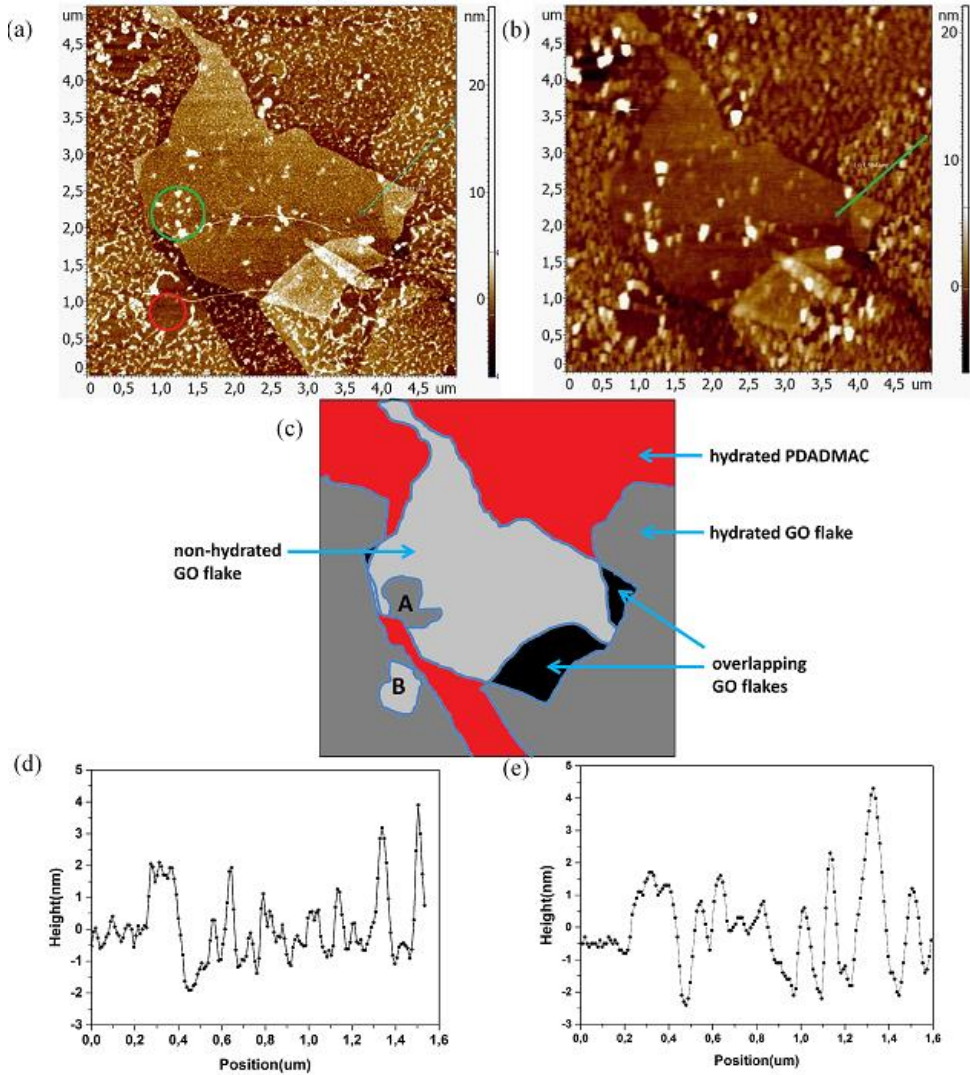




**Figure 5.1.** (a) Tapping-mode-AFM height image of a PDADMAC/GO-coated Si/SiO<sub>2</sub> wafer, measured after 14 days of equilibration in air, at a relative humidity of about 60%. Different colors indicate different heights. (b) Height image of the same area as (a), scanned using lateral-force-mode AFM. The load force is set at -0.15 nN, which is about half of the detachment force. (c) Schematic drawing of the different patches on the sample surface, as shown in (a) and (b). The red area indicates hydrated PDADMAC not covered by GO. Dry GO, hydrated GO, and overlapping GO patches are clearly recognizable and colored light gray, dark gray, and black, respectively. The area marked by A indicates a hydrated GO patch amidst dry GO, (the area marked with a green circle in (a)). The area marked by B indicates a dry GO patch amidst hydrated GO (the area marked with a red circle in (a)). (d) Height profile along the green line in the image, obtained by Tapping-mode-AFM. (e) Height profile along the green line in the image, obtained by lateral-force-mode AFM.

In lateral-force AFM, as the tip is dragged across the surface, there is a force component parallel to the sample surface as well. We found that during the lateral-force measurements these bright spots deformed, indicating that they are liquid. As the sample is hydrophilic and equilibrated in humid air, it is reasonable to assume that the spots correspond to patches of physically adsorbed water. These noncontiguous water spots are likely due to the fact that the GO we used is not totally oxidized. As proved in chapter 3, the GO surface is composed by graphene domains and GO domains, the graphene areas are hydrophobic, and the GO domains are hydrophilic. The observed noncontiguous water spots are therefore consistent with our results described in chapter 3. Three patches are clearly distinguishable, as schematically indicated in Figure 5.1.c, One is the PDADMAC/GO-coated patch (in the middle, indicated in in Figure 5.1.c by light gray), the second patch is a hydrated PDADMAC/GO area (bottom, left and right, indicated in Figure 5.1.c by dark gray), and the third area is hydrated PDADMAC (top, and middle of bottom, indicated in Figure 5.1.c by red). The discontinuous hydration film is formed both on (uncovered) PDADMAC as well as on areas covered by GO. At the hydrated GO patch, some non-hydrated spots are also clearly recognized (marked by the red circle), these reflect the areas that graphene domains. *Vice versa*, for the ‘dry’ GO area some patches are hydrated, as marked by the green circle in Figure 5.1.a.

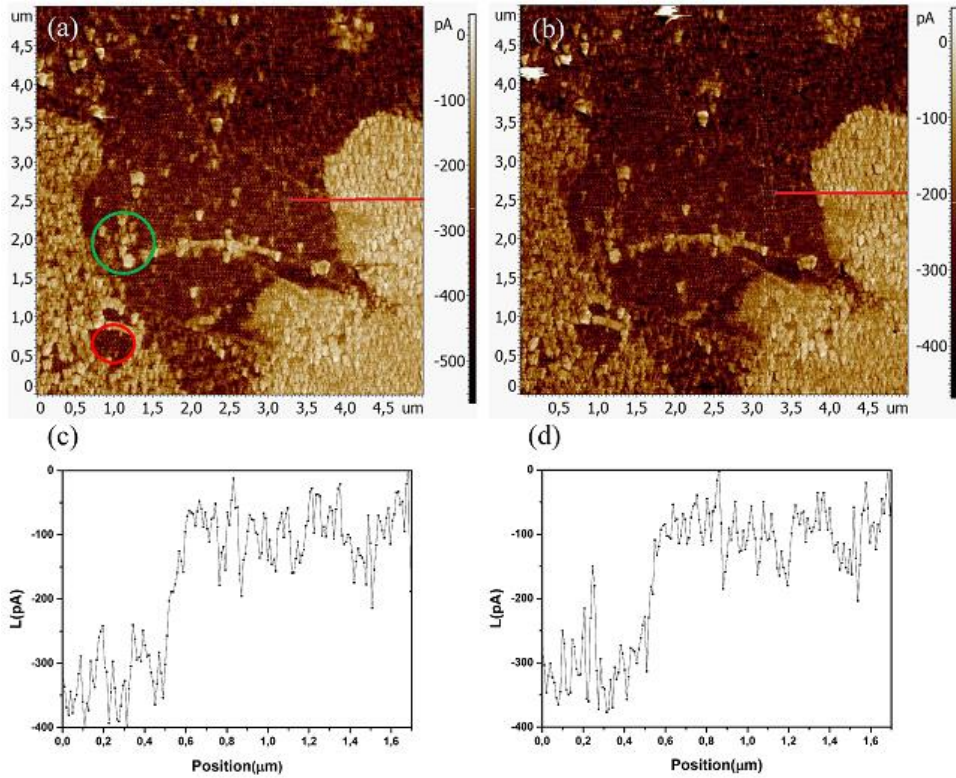


**Figure 5.2.** Frictional-force image on the PDADMAC/GO-coated Si/SiO<sub>2</sub> wafer at the same area as depicted in Figure 5.1, obtained by lateral-force-mode AFM. The scanning direction is from left to right. The frictional signal  $L$  is proportional to the friction force, as discussed in the experimental section. In (a) and (c) the normal-load force is  $-0.15$  nN and in (b) and (d) the normal-load force is  $0$  nN. (c) and (d) show the profiles of the frictional force signal along the trajectory indicated by the red lines in (a) and (b). The encircled areas are the same as in Figure 5.1.a. The green circle in (a) encloses a patch of hydrated GO, and the red circle encloses a patch of non-hydrated GO.

In Figure 5.2 is shown the frictional-force image on the GO-coated sample at the same area as depicted in Figure 5.1, obtained using lateral-force-mode AFM. The lateral-force signal  $L$  is proportional to the frictional force  $F_L$  (see the Experimental Section);  $L = 0$  implies no friction. Figure 5.2.a shows lateral-force signal when the applied normal load force is  $-0.15$  nN. At this negative load force, the attractive tip-substrate contact is preserved as it corresponds to about half of the adhesive force, these very small forces are chosen in order

to maintain the water islands structure. In Figure 5.2.b is shown the lateral-force signal  $L$  when the normal load force is 0 nN. Figure 5.2.c and 2.d show the profiles of the lateral-force signal along the red line of Figure 5.2.a and 5.2.b, with a normal load force of -0.15 nN and 0 nN, respectively. In the lateral force images: the brighter the color, the smaller the lateral force. Dry PDADMAC/GO-coated area and hydrated PDADMAC/GO-coated area are clearly distinguishable from the frictional force signal image. For dry GO,  $\Delta I_x$  is about  $-350$  pA, while at GO covered by a hydration film, the  $\Delta I_x$  decreases to about  $-100$  pA. Herein, a negative sign refers to friction force with a direction opposite from the interfacial shear direction. The similar magnitude of  $\Delta I_x$  in Figure 5.2.a and 5.2.b, corresponding to normal load forces of -0.15 nN and 0 nN respectively, can be explained that at the nanoscale friction behaves non-linear. Different from macro scale tribology, at the nano scale friction is still observed even when a negative load force is applied. This is attributed to adhesive Van der Waals forces. Even at a negative load, the contact between tip and surface remains, due to a deformation of the surface. This is typical for nanoscale investigations. For common macroscopic surfaces such Van der Waals forces are usually negligible, as the experienced contact area is very small, compared to the geometric area, due to the surface roughness. In order to mimic the conditions during practical applications, where the interfacial adhesion forces act as the normal load force, the normal load force in our work was set to a level comparable to the adhesion force.

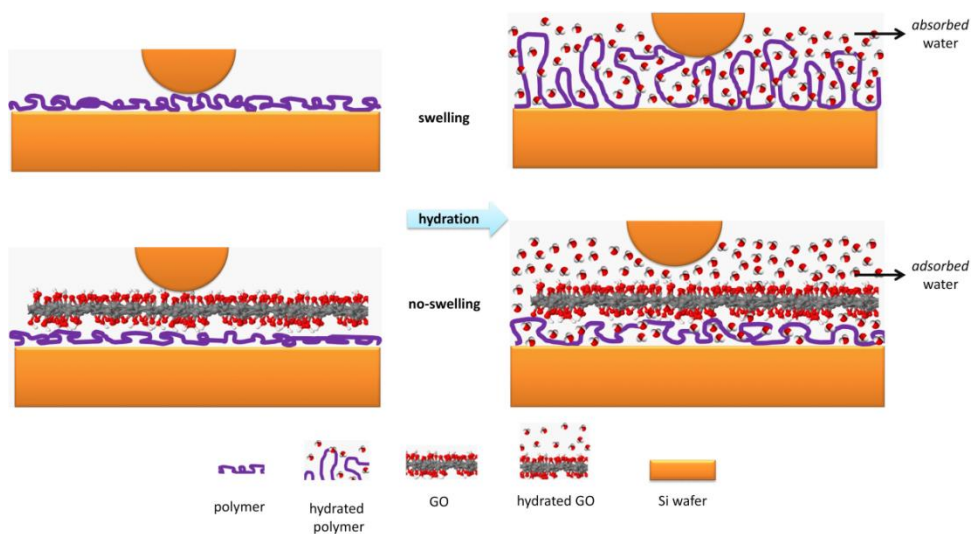


**Figure 5.3.** Schematic drawing of the friction between an AFM tip and some differently coated surfaces. Left panels illustrate dry surfaces, and right panels hydrated ones. Top panels illustrate surfaces covered by just an adsorbed layer of PDADMAC, bottom ones represent surfaces where GO is adsorbed on top of the PDADMAC layer.

As illustrated in Figure 5.3, in the presence of water, GO can *adsorb* a thin water film at its surface, due to the present hydrophilic GO domains. The orientation of the water molecules will be influenced by the oriented surface hydrophilic moieties. Like most of the other 2D materials, such as graphene and MoS<sub>2</sub>, GO has a two-dimensional covalently bonded structure with a high degree of bonding (inherited from the original graphene structure). This structure does not allow for swelling, and any shape deformation as happens with adsorbed polymer layers (for the formation of protruding loops and tails).<sup>[23]</sup> As a result, the local density of the hydration film does not change. In this situation, the interfacial force between AFM tip and GO will be repulsive due to the presence of the 2-4 nm thick oriented hydration layer,<sup>[7]</sup> and lubrication by water occurs. For uncovered and hydrated PDADMAC surfaces the induced swelling of the polymers will change the local density of the hydration film, leading to attractive interfacial forces and no lubrication.

## 5.4 Conclusions

Using lateral-force AFM with a Si/SiO<sub>2</sub> tip on hydrated and non-hydrated GO surfaces, covering PDADMAC modified silicon wafers, we have proven the lubrication by the presence of an oriented water layer on top of the GO material. At constant local density of the water, the oriented water molecules contribute to a repulsive interfacial force. This was expected from the theory of hydration forces between surfaces as developed by Besseling.<sup>[7]</sup>

## 5.5 References

- [1] F. P. Bowden, D. Tabor, *The friction and lubrication of solids*, Vol. 1, Oxford university press, 2001.
- [2] M. Urbakh, J. Klafter, D. Gourdon, J. Israelachvili, *Nature* 2004, 430, 525.
- [3] F. Bowden, J. Gregory, D. Tabor, *Nature* 1945, 156, 97; H. E. Sliney, *Tribology International* 1982, 15, 303.
- [4] S. Sanchez, A. A. Solovev, Y. Mei, O. G. Schmidt, *Journal of the American Chemical Society* 2010, 132, 13144; D. S. Jones, C. P. Garvin, S. P. Gorman, *Biomaterials* 2004, 25, 1421. V. C. Mow, A. Ratcliffe, S. L. Woo, *Biomechanics of diarthrodial joints*, Vol. 1, Springer Science & Business Media, 2012.
- [5] B. A. Omotowa, B. S. Phillips, J. S. Zabinski, J. n. M. Shreeve, *Inorganic chemistry* 2004, 43, 5466.
- [6] U. Bauer, M. Scharmann, J. Skepper, W. Federle, *Proceedings of the Royal Society of London B: Biological Sciences* 2013, 280, 20122569; *PhysicsWorld1'sChannel*, Online video clip. YouTube. 2010.
- [7] N. Besseling, *Langmuir* 1997, 13, 2113.
- [8] H. Yamakiri, S. Sasaki, T. Kurita, N. Kasashima, *Tribology International* 2011, 44, 579.
- [9] W. H. Briscoe, S. Titmuss, F. Tiberg, R. K. Thomas, D. J. McGillivray, J. Klein, *Nature* 2006, 444, 191.
- [10] B. Konkena, S. Vasudevan, *The journal of physical chemistry letters* 2012, 3, 867.
- [11] H.-J. Kim, D.-E. Kim, *Scientific reports* 2015, 5.
- [12] H. J. Kim, D. G. Shin, D.-E. Kim, *International Journal of Precision Engineering and Manufacturing-Green Technology* 2016, 3, 91.

- [13] Y. Zhou, J. Dahl, R. Carlson, H. Liang, *Carbon* 2015, 86, 132.
- [14] H. Kinoshita, Y. Nishina, A. A. Alias, M. Fujii, *Carbon* 2014, 66, 720.
- [15] D. R. Dreyer, S. Park, C. W. Bielawski, R. S. Ruoff, *Chemical Society Reviews* 2010, 39, 228.
- [16] J. Kim, L. J. Cote, J. Huang, *Accounts of Chemical Research* 2012, 45, 1356.
- [17] K. Novoselov, A. K. Geim, S. Morozov, D. Jiang, M. Katsnelson, I. Grigorieva, S. Dubonos, A. Firsov, *nature* 2005, 438, 197.
- [18] K. Erickson, R. Erni, Z. Lee, N. Alem, W. Gannett, A. Zettl, *Advanced Materials* 2010, 22, 4467.
- [19] S. Pei, H.-M. Cheng, *Carbon* 2012, 50, 3210.
- [20] G. Decher, J. Schlenoff, G. Pacchioni, S. Valeri, Wiley Online Library; N. I. Kovtyukhova, P. J. Ollivier, B. R. Martin, T. E. Mallouk, S. A. Chizhik, E. V. Buzaneva, A. D. Gorchinskiy, *Chemistry of Materials* 1999, 11, 771.
- [21] R. Levy, M. Maaloum, *Nanotechnology* 2002, 13, 33.
- [22] NT-MDT, <http://www.ntmdt.com/spm-basics/view/cantilever>.
- [23] R. Nair, H. Wu, P. Jayaram, I. Grigorieva, A. Geim, *Science* 2012, 335, 442.
- [24] X. Zhang, J. Yin, C. Peng, W. Hu, Z. Zhu, W. Li, C. Fan, Q. Huang, *Carbon* 2011, 49, 986.

## AFM study of lubrication of Graphene oxide surface by water

### Supporting Information

## 1. Similar sandwich structures of GO and a surfactant bilayer

As mentioned in the main text, Wuge et al <sup>[1]</sup> found that boundary lubrication of water occurs, between two sliding mica surfaces bearing surfactant monolayers with a certain amount of water. The key factor is here the hydrophilic/hydrophobic/hydrophilic sandwich structure, composed by the polar surfactant heads/ apolar surfactant tails/ polar surfactant heads. Upon addition of some water, the friction is reduced considerably. This is explained by a shift of the slip plane from the hydrophobic surfactant tails to the layer between mica and the layer of hydrophilic surfactant head groups. This is only possible because of the nearly atomically smooth nature of both the mica and the surfactant head group layer. From this point of view, GO has a structure similar to the surfactant bilayer. GO has an atomically smooth sandwich structure, the inside part is composed by single layer of covalent bonded carbon atoms, and the outside layers are composed of polar groups. Due to the polar moieties formed upon the oxidation of graphite from which it is produced,<sup>[2]</sup> GO is quite hydrophilic. This part is similar to the polar headgroups of the surfactants bilayer, able to bind water. The inside covalent bonded carbon network is similar to the apolar tails of the surfactant bilayer. The difference between these two similar structures is that GO has a rigid covalent bonded inner structure, which makes it strong and independent of the surroundings e.g. the absence of two atomically smooth mica surfaces. For surfactant bilayers, the structure is not as stable as GO and this limits its practical applications. This also indicates the possibility of making different artificial surfaces lubricated by water, by coating with GO.

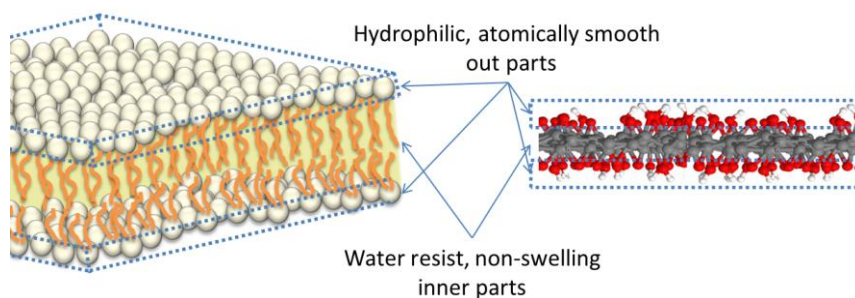


Figure S1 Schematic drawing of the similarity of a surfactant bilayer and GO.

## 2. Stability of polycation/GO coating on a silica surface



PDADMAC was firstly coated onto Si wafer using dipping method. GO was then spin coated onto Si/PDADMAC. As shown in Figure 5.2, GO can be well coated on polycation PDADMAC modified Si/SiO<sub>2</sub>. The coating has an ultra-strong stability even under high ionic strength conditions (3M NaCl) and mechanical forces (tape treatment) . As shown in Figure 5.1, after sonication in water, ethanol and aqueous 3 M NaCl for 5 min., the surface is still fully covered by GO. This layer-by-layer approach to fabricate GO coatings is applicable for a large variety of substrates.

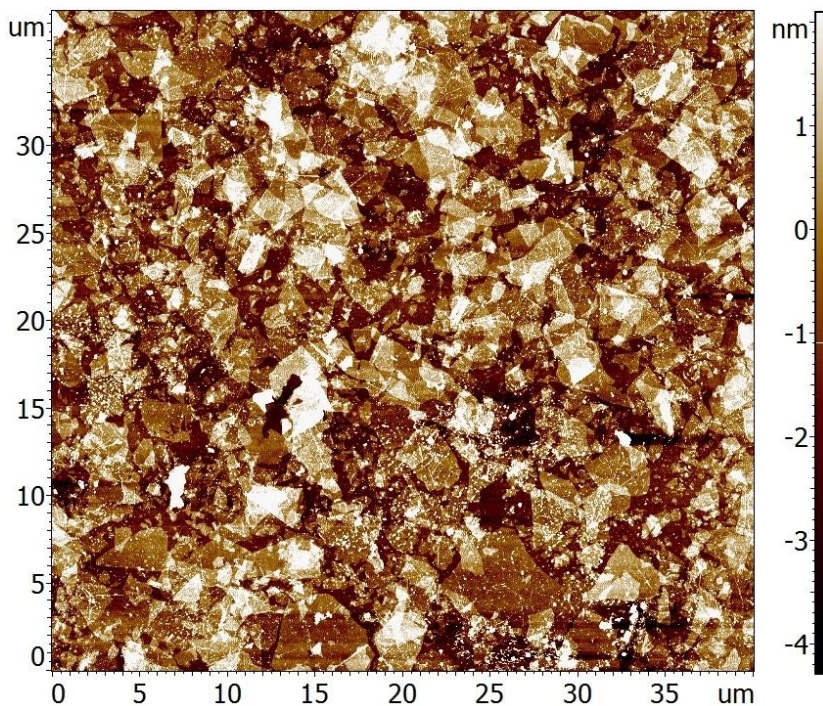


Fig S2 Surface morphology of a GO coated surface on PDADMAC modified Si/SiO<sub>2</sub> wafer , as studied using tapping mode AFM.

### 3. References

- [1] W. H. Briscoe, S. Titmuss, F. Tiberg, R. K. Thomas, D. J. McGillivray, J. Klein, *Nature* 2006, 444, 191.
- [2] D. R. Dreyer, S. Park, C. W. Bielawski, R. S. Ruoff, *Chemical Society Reviews* 2010, 39, 228.





**Atomic origin of the onset of slip  
of frictional motion at single  
asperity contact**

6

**Abstract:**

Continuous hold-relax-hold (HRH) single asperity (SA) experiments are performed to study the dynamics at the onset of the frictional motion (known as ‘slip’). This slip behaviour can be found in everyday processes and is dominant in various fields, varying from fracture, tribology to even earthquakes. Current investigations are focused on macroscale, since macroscale contacts can be regarded as many-body system composed by multiple SA contacts. In this chapter, we show the first report that describes the dynamics of the slip between a silicon AFM tip and silicon wafer at SA contact. It is found that the force relaxation at the onset of the slip can be described by a stretched exponential followed by a single exponential law. Our results show the existence of multiple length and time scales at SA contact, which originate from multiple atomic interactions at a SA contact. At current stage, this chapter mainly focuses on the experimental results of the transition from stick to slip at single asperity contacts and preliminary mathematical analysis. The model to describe this phenomenon is still under construct.

## **6.1 Introduction**

Static friction forces are larger than dynamic friction forces.<sup>[1]</sup> At the onset of all frictional motions therefore slip occurs. This slip behaviour can be found in everyday processes and is dominant for proper fundamental understandings in various fields, e.g. earthquakes,<sup>[2]</sup> tribology,<sup>[3]</sup> and fracture.<sup>[4]</sup> A lot of attention has been paid to understand this onset of slip.<sup>[5-7]</sup> Recent investigations show that at a macroscale contact, this slip can be described by a rupture mechanism.<sup>[8]</sup> The onset of the slip is preceded by detachment fronts, with different speed and length scales, and starts at the contact trailing edge and extends across the whole contact.<sup>[8]</sup> This rupture mechanism is further proved by experimental results from Jay Fineberg et al.<sup>[5, 6, 9]</sup> These detachment fronts are classified into three different types: slow, sub-Rayleigh and super-shear ruptures, according to their speed and length scales. The dominance of these types of detachment fronts depends on the normal load forces.<sup>[5, 6, 9]</sup> When the normal load force is very small, the super-shear ruptures, which means a fast slip under small shear force, are dominant. For large normal load forces, the slow ruptures, which indicates a slower slip and larger shear force, are dominant.<sup>[6]</sup> This rupture mechanism is built up by assuming that the macroscale contacts between two rough surfaces are composed by multiple single asperity (SA) contacts.<sup>[8]</sup> A SA contact indicates that only mutual atomic contacts play a role. However, what happens at the onset of a SA contact frictional motion has until now not experimentally studied. Recently, SA friction experiments using atomic force microscopy (AFM) proved that the frictional aging behaviour at SA contacts follows the same law as multiple-contact at macroscale.<sup>[10]</sup> This is probably due to the fact that SA contacts can be regarded as multiple-contact of atomic interactions. This is physically analogous to the description of macroscale contacts.<sup>[10, 11]</sup> It indicates the onset of slip of a SA contact frictional motion is also dominated by ruptures with different time and length scales.

## 6.2 Results and discussions

### 6.2.1 Description of the continuous hold-relax-hold (HRH) SA experiments

Herein, we use a continuous hold-relax-hold (HRH) experiments to study the transition from stick to slip at SA contact using atomic force microscopy (AFM). Figure 6.1 shows the schematic drawing of the continuous HRH-SA system. A silicon AFM tip and a silicon wafer both with native oxidized layers are used. This is a model system for various relevant friction studies e.g. earthquakes.<sup>[10]</sup> As shown in Figure 6.1, the scanner with the installed silicon wafer moves step-wise, in each step, the sample moves by  $\Delta x_s'$  in a time period of  $t_{\Delta x}$ , then the sample is held at this position for a time period of  $\Delta t$  ( $\Delta t \gg t_{\Delta x}$ ). The sample displacement  $\Delta x_s = n\Delta x_s'$ , where  $n$  is the number of steps. In the schematic drawing, the sample displacement  $\Delta x_s$  is represented as black solid line corresponding to the left vertical axis. When the AFM tip contacts with the sample surface under certain normal load forces, in the beginning the tip movement follows the sample, and the cantilever twists. This is a consequence of the mutual interfacial friction force. The twist force of the cantilever is equal to the interfacial friction force between tip and sample, but has opposite sign. As shown in Figure 6.1, in the first steps (e.g. steps 1-2), the tip sticks to the sample and moves with the sample. Thus, the tip displacement  $\Delta x_t = \Delta x_s$ . Using AFM, we measure the lateral signal from the position-sensitive photodetector (PSPD)  $\Delta I_x = I_x - I_{x,0}$  where  $I_x$  is the PSPD readout, and  $I_{x,0}$  is the value when in the absence of a lateral force. As discussed in Chapter 3, for a not too large  $\Delta x_t$ , the lateral signal is linear in the tip displacement,  $\Delta I_x = \sigma_x \Delta x_t$ , where  $\sigma_x$  is the lateral sensitivity coefficient. The lateral signal records the position of the tip, as shown on the right vertical axis in Figure 6.1. In the first 2 steps, for each  $\Delta x_s'$ ,  $\Delta I_x$  changes by  $\Delta I_{x'}$  and obviously,  $\Delta I_{x'} = \sigma_x \Delta x_s'$ . We denote this as the '**stick region**' (white region in Figure 6.1). In the schematic drawing,  $\Delta I_x$  is represented as a dashed red line, and corresponds to the right vertical axis. After the third step in the drawing, the cantilever twist force is comparable to the maximum static friction force, and a further twist of the cantilever may lead to slip of the tip. This slip is recorded by the drop of the lateral force signals  $\Delta I_x$ .

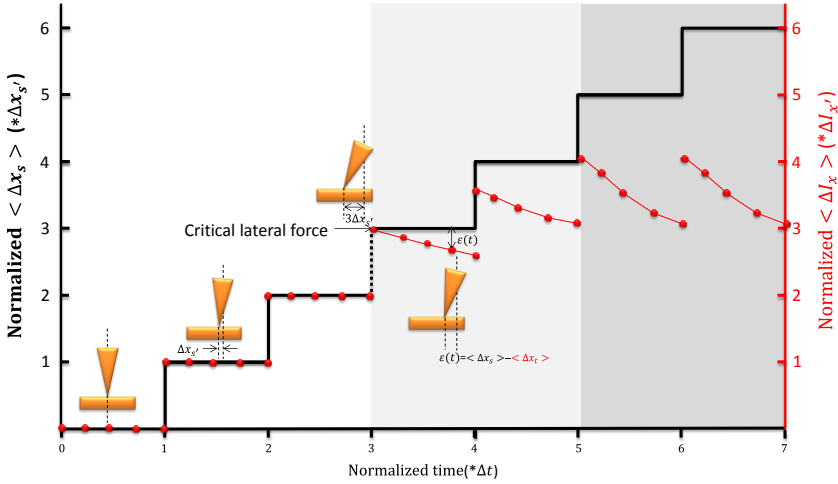


**Figure 6.1.** Schematic drawing of the designed continuous hold-relax-hold single asperity (HRH-SA) experimental system.  $\overline{\Delta x_s}$  corresponds to the averaged position of the silicon wafer (the black solid line),  $\overline{\Delta I_x}$  corresponds to the averaged position of the AFM tip (the dashed red line).

We need to notice that the dashed line represents the averaged tip position of many recorded traces. In each repeated trace, when the AFM tip is contact with the sample surface under a certain drive force (twist force of the cantilever,  $\propto \Delta I_x$ ), at certain time, detachment of the contact may happen. This slip is represented as drop of  $\Delta I_x$ . As we discussed above, the detachment at SA contacts may also be classified into different types of ruptures, with different speed and length scales.

Thus, by repeating a large number of traces, slips with a range of length and time scales are all observed and this different scale slip occurs with different possibilities. The averaged decays of all these traces, which is the consequence of possibility distribution are expected to follow a stretched exponential law, since such a description is widely used to describe empirically the relaxation in disordered systems,<sup>[12]</sup> This is the ‘**transition region**’ and indicated in light grey in Figure 6.1.

After enough steps, this bend-slip behaviour will become similar (or ‘repeated’), as shown in the dark area of the drawing. In this stage, the tip slips back to its starting position during



each time interval  $\Delta t$ . This is called the ‘**repeated slip region**’ and is indicated in grey in Figure 6.1.

During each scan, at certain time  $t$  the slip distance of the tip is  $\varepsilon_i(t)$ , where  $i$  varies from 1 to  $N$ , and  $N$  is the total number of scans. Herein,  $\varepsilon(t)$  is defined as the averaged total slip distance between the tip and the sample,  $\varepsilon(t) = \frac{\sum_1^N \varepsilon_i(t)}{N}$ . As shown in the Figure 6.1,  $\varepsilon(t) = \langle \Delta x_s \rangle - \langle \Delta x_t \rangle$ , where  $\langle \Delta x_s \rangle$  and  $\langle \Delta x_t \rangle$  are the averaged displacements of  $N$  scans. Obviously, at stick conditions,  $\varepsilon(t) = 0$  and at the repeated slip region conditions,  $\varepsilon(t) \propto vt$ , where  $v$  is the average speed of the sample. How precisely  $\varepsilon(t)$  changes from 0 to linear increasing, is an interesting issue that gives the physical picture of a shearing interface from static to dynamic movement. As schematically shown in the red curves during the normalized time 3-7, the decay rate of  $\langle \Delta I_t \rangle$ , which is  $\frac{\partial \langle \Delta I_t \rangle}{\partial t}$  describes the relaxation rate of a AFM tip at contact with a silica surface.

Experimentally, the step-like movement of the sample in this continuous HRH-SA experiments is realized by making use of the closed loop control of the AFM scanner. For almost all modern AFM instruments, the linearity of the sample movement is precisely controlled by a closed loop controller, which is known as proportional–integral–derivative (PID controller).<sup>[13]</sup> During the scan, a capacitive position sensor detects the displacement of the scanner by a certain interval  $\Delta x'$ , and simultaneously corrects the sample displacement to the target position. To realize the linear movement, there is a minimum scan rate, which is  $v_{min} = \Delta x' / t_{\Delta x'}$ , where  $t_{\Delta x'}$  is the time in which the scanner reaches the target position. In this case, the displacement of the sample is corrected, while the waiting time between each correction is zero and, in this way, the linearity of the displacement is realized. Obviously, when the scan rate is set much lower than  $v_{min}$ , the scanner will move step-wise, since the waiting time is enlarged.

## 2.2 Experimental results and analysis

In Figure 6.2 the HRH experimental results are shown with various normal load forces (called as Case 1). In Figures 6.2a, c, e, and g, the normal load forces are -0.5 nN, 0 nN, 0.5 nN and 1 nN, respectively. In Figure 6.2 a, c, e, and g, the blue lines are the averaged lateral signal  $\Delta I_x$  of 1024 scans as a function of time. The range of each single scan is 12.9 nm.

The scan frequency was set at 0.200 Hz, so the duration of a single scan, during which  $\Delta x_s$  varies from 0 to 12.9 nm, is 5.00 s, and the average scan speed is 2.58 nm/s. 1024 points are gathered in a single scan. The feedback loop controlling the tip-sample distance was operated very slowly, to avoid any influence on the lateral signals. The black line corresponds to the theoretical signal when no slip would occur at the interface between AFM tip and silica surface, so that the tip moves with the sample connected to the piezo scanner ( $\Delta x_t = \Delta x_s$ ).

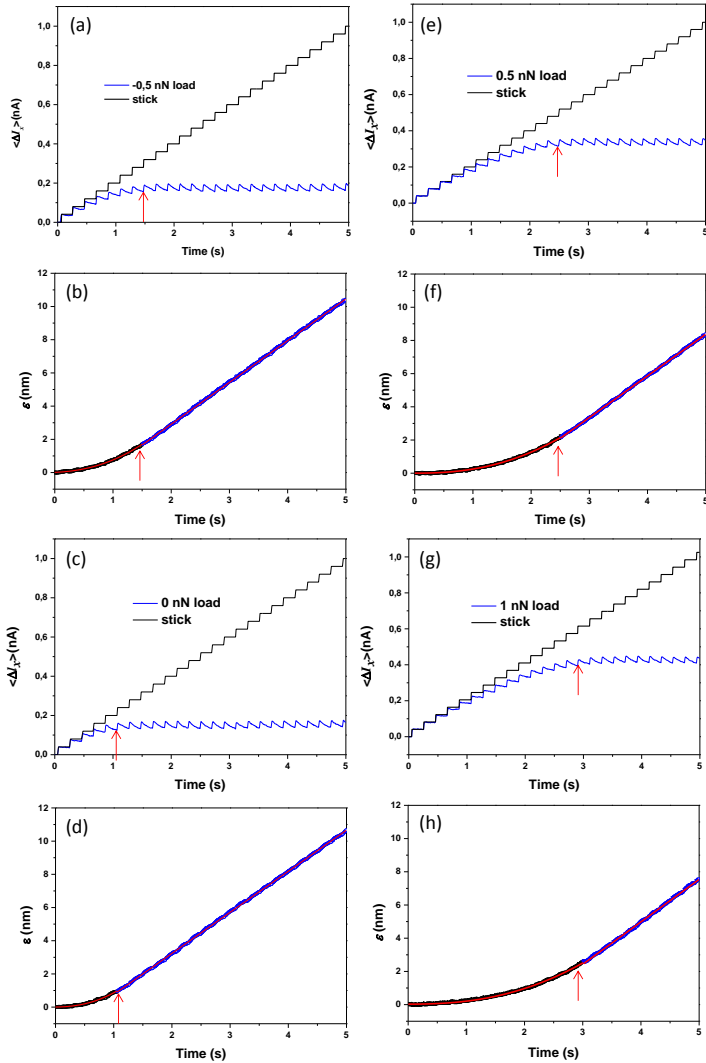


**Figure 6.2.** Experimental results of the performed HRH SA experiments. (a) The blue line is the averaged lateral signal  $\Delta I_x$  of 1024 scans as a function of time. The normal load force is  $-0.5$  nN. A negative normal load corresponds to a force pulling the tip from the surface; tip-surface contact is maintained by adhesive interactions. (b)  $\varepsilon(t) = \langle \Delta x_s \rangle - \langle \Delta x_t \rangle$  as a function of time.  $\varepsilon$  is fit as a power law and linear with time in transition region and repeated slip region, respectively. (c, d), (e, f) and (g, h) are the results when the normal load force are 0, 0.5, 1 nN, respectively. In this experiment, the relative humidity (RH) is fixed at 40% and the temperature is  $25.9$  °C. The RH and temperature is measured by the inner sensor of the AFM instrument.

The step-like response is clearly recognised as shown in the blue line of Figures 6.2a, c, e, and g. We clearly recognise steps originating from the, on average, stepwise motion of the piezo scanner, corresponding to the black lines in Figures 6.2a, c, e, and g. With the current settings, the change of  $\Delta x_s$  from 0 to 12.9 nm in 5.00 s is achieved in 25 steps, which are clearly recognised in these averaged stepwise traces. So, each step has a magnitude of  $\Delta x' = 0.516$  nm, and the time interval between steps is 0.200 seconds. For each  $\Delta x'$ ,  $\Delta I_x$  changes by  $\Delta I_{x'} = 0.040 \pm 0.002$  nA.

In Figures 6.2a, c, e, and g, the stick region is all recognised in the first few steps. In this region, the blue line, which corresponds to the average position of the AFM tip, overlaps with the black line, which corresponds to the average position of the sample. After certain steps, this two lines separate with each other, indicating the occurrence of slip between the AFM tip and the sample. This is the ‘transition region’, the occurrence of this region depends on the normal load force. For larger normal load force, the ‘transition region’ comes later (more interfacial frictional force).

After certain steps, the averaged slip behaviour becomes similar (‘repeated’). Further displacement of the sample leads to further displacement of the AFM tip, but the tip will slip back to its starting position during each time interval  $\Delta t$ . The transition from the ‘transition region’ and to the ‘repeated slip region’ is indicated by red arrows. As an example in Figure 6.2g (the normal load force is  $+1$  nN), during the first three steps, the tip follows the movement of the sample. The slip starts from the fourth step, at the beginning the relaxation rate is slow. When the twist force becomes larger, the relaxation rate becomes faster. After fourteen steps, the twist force has become larger than the maximum static friction force and the relaxation becomes similar in the following steps. All these

experimental observations are consistent with our expectation and the three different friction regions are all observed. With the lateral sensitivity (defined the same as in Chapter 4, the change of  $\langle \Delta I_x \rangle$  corresponding to unit displacement of the AFM tip), we can easily get the total interfacial displacement  $\varepsilon(t) = \langle \Delta x_s \rangle - \langle \Delta x_t \rangle$  as a function of time, as shown in Figures 6.2b, d, f and h.

As indicated above, how  $\varepsilon(t)$  changes from 0 to a linear increasing regime is an interesting issue that gives the physical picture of a shearing interface from static to dynamic. Herein, we found that in the repeated slip region,  $\varepsilon(t)$  increases linearly with time. It indicates the relative velocity between the AFM tip and sample becomes constant. In the transition region,  $\varepsilon(t)$  vs time is well fitted by a power law as  $\varepsilon \propto At^b$ .

The parameter  $b$  is found to be  $\sim 2.35$ . A repeated experiment was performed, under the application of a different scan rate, scan range, AFM tip (same probe type but a different one) and ambient conditions (humidity and temperature), and this parameter is found to be independent of these parameters (the experimental details, see the repeated experiments denoted Case 2, as shown in chapter 4). Figure 6.3a summarizes the value of parameter  $b$  in all the experiments. However, the physical origin why the average motion of a shearing interface from static to dynamic follows a power law with a power of 2.35 is still not clear. As shown in Figure 6.3b, the maximum static friction force increases with larger normal load force, which is consistent with the well-known friction law.

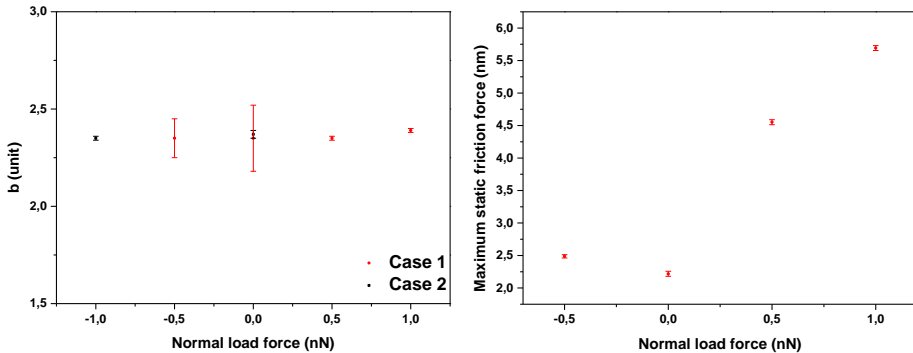


**Figure 6.3.** (a) Value of  $b$  in all these experiments (Case 1 is the experiment shown in Figure 6.2 and Case 2 is the repeated experiment with different parameters as shown in Chapter 4). (b) Maximum static friction force at different normal load force in Case 1.

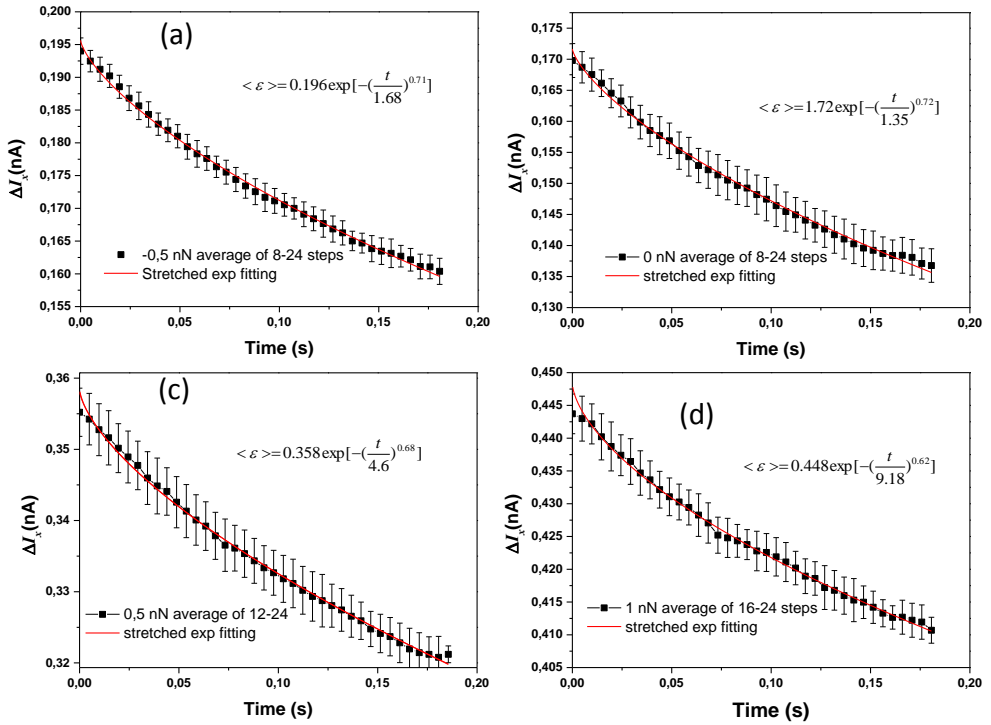


**Figure 6.4.** Average of all these relaxation in the ‘repeated slip region’. The dash black lines are averaged relaxation of the tip,  $\langle \Delta I_x \rangle$  vs time, in the ‘repeated slip region’. The solid red lines are the stretched exponential fitting of the  $\langle \Delta I_x \rangle$  vs time curves. (a) at normal load force -0.5 nN, from step 8-24. (b) at normal load force 0 nN, from step 8-24. (c) at normal load force 0.5 nN, from step 12-24. (d) at normal load force 1.0 nN, from step 16-24.

Now we will discuss about the slip behaviour of the two surfaces at contact. In the ‘repeated slip region’, the tip relaxes to its starting position during the time interval of that step. For each step, the tip slip behaviour is more or less similar. In Figure 6.4 the averaged tip relaxation during the steps in the ‘repeated slip region’ are plotted as a function of time. As we discussed above, when  $\Delta I_x \ll l_{tip}$ , where  $l_{tip}$  is the height of the tip ( $\sim 10 \mu\text{m}$ ),  $\Delta I_x \propto f_x$ , where  $f_x$  is the twist force of the cantilever. Thus, Figure 6.4 also describes the force relaxation of a silicon tip when shearing with a silica surface. This is highly relevant, not only here, but also in the understanding of friction related to for instance earthquakes.

Slip will occur if the interfacial force exceeds the maximum static friction force. The relaxation of the tip follows a stretched exponential law (Figure 6.4) given by:

$$\Delta I_x = \Delta I_m \exp\left[-\left(\frac{t}{\tau}\right)^b\right], \quad (1)$$

where  $\Delta I_m$  is the maximum lateral signal,  $b$  is the stretched exponential law parameter varying from 0 to 1,<sup>[14]</sup> and  $\tau$  is the relaxation time. With increasing normal load forces,  $b$  becomes far less than 1, which indicates a broader variation of length and time scales. This clearly demonstrates our made assumption that at SA conditions the contact between tip and surface can be regarded as multiple-contact of atomic interactions. The onset of slip of a SA contact frictional motion can be described successfully by a similar physical law as applied for macroscale contacts. If this is the case, at the beginning of the twist, slips of the tip should be dominated by detachments with different length scales. Thus, the stretched exponential law by fitting the ‘repeated slip region’, should not describe the slip behaviour at very small twist forces.

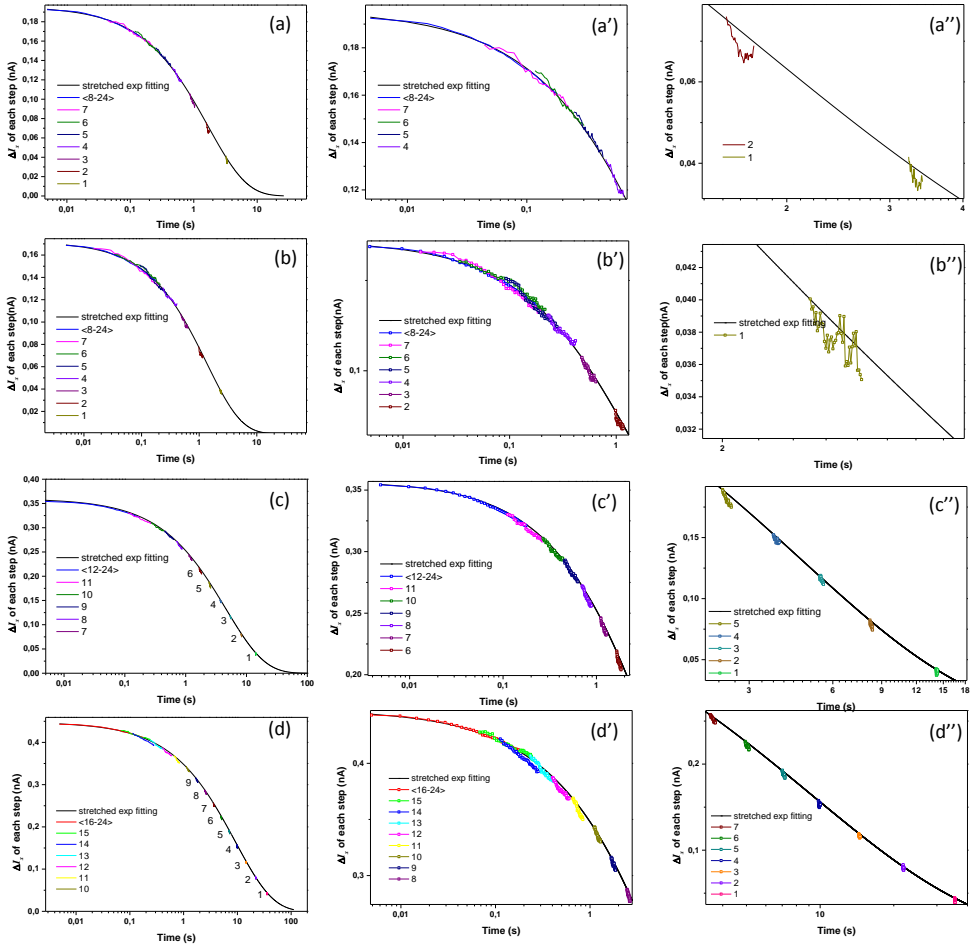


**Figure 6.5.** The measured  $\Delta I_x$  vs time of all these 24 steps are plotted. Stretched exponential law fitting is used as shown in equation (1). Stretched exponential law fittings are plotted with solid black lines. (a)-(d) are under different normal load forces,  $-0.5$  nN,  $0$ ,  $+0.5$  nN and  $+1$  nN, respectively. Note that when there is a gap of  $\Delta I_x$  between adjacent steps, the real time is not known. In this fitting, the initial time of these steps (e.g. 1-3 steps in a and 1-8 steps in c) is determined according to the  $\Delta I_x$  values. More details about the fitting are shown in (a')-(d') and (a'')-(d''), respectively.

Now we check if the tip relaxation behaviour at different lateral force can be described by a same stretched exponential law. As shown in Figure 6.5, we plot all these decay of the tip using a stretched exponential law fitting. The black lines are the stretched exponential

fitting according to equation 1. The measured  $\Delta I_x$  vs time curves of all these 24 steps are plotted. As shown in Figure 6.5 (a'-d'), the stretched exponential law fits the relaxation when the twist force is large, and indeed, it does not fit the 'tails' of the relaxation as shown in Figure 6.5 (a''-d''), when the twist force of the cantilever is very small. In Figure 6.6,  $\Delta I_x$  of each step is plotted logarithmically. All the red lines, which are the single exponential fitting of the steps, are now parallel. This indicates the 'tails' of the relaxation follows more like a single exponential law, which means in this region, the slips are dominated by detachment with more or less the same length and time scales.

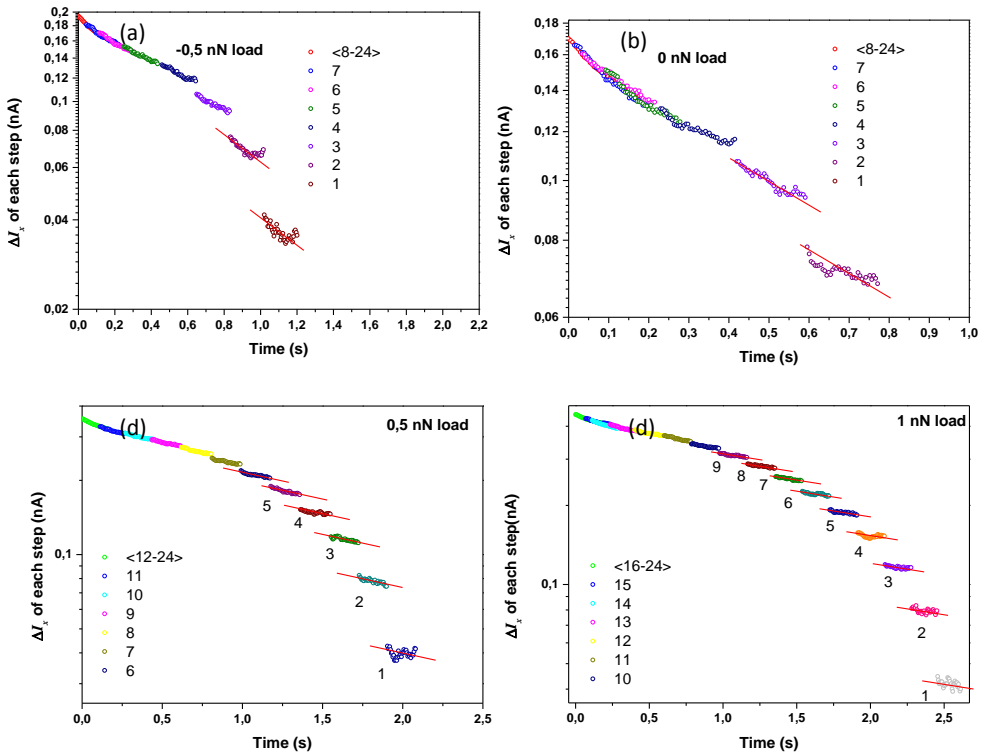


**Figure 6.6.** The measured  $\Delta I_x$  vs time of all these 24 steps are plotted. Single exponential law fitting is used. Single exponential law fittings are plotted with solid red lines. (a)-(d) are under different normal load forces,  $-0.5$  nN,  $0$ ,  $0.5$  nN and  $1$  nN, respectively. The red lines are parallel in each graph.

Stretched exponential relaxation indicates the existence of a dynamic heterogeneity and a variation of relaxation times.<sup>[15]</sup> In our experiments, the silicon wafer surface is covered by



a thin native oxide layer. This layer is atomically rough and amorphous, and at contact, there are multiple atomic interaction pairs which are non-homogeneous. During the slip, these atomic contacts have different relaxation times. At small twist forces a single exponential law describes well our observed slip behaviour .

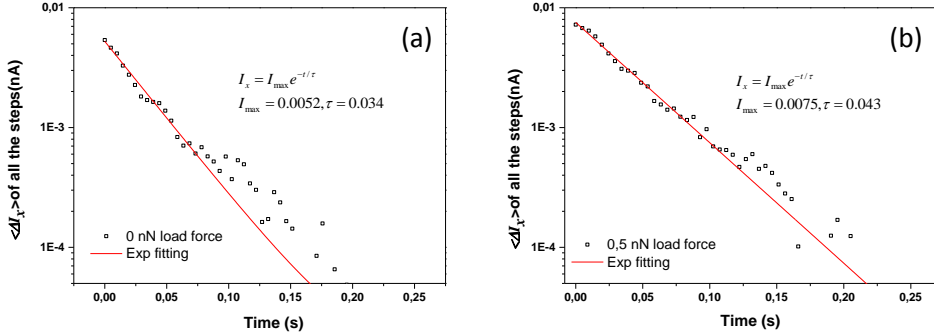


**Figure 6.7.** Force relaxation curve on mica surface. (a) the normal load force is 0 nN. (b) the normal load force is +0.5 nN. The red lines show the exponential fitting of the data.

To further demonstrate the applicability of our model, continuous HRH-SA experiments were performed on mica surfaces, which is atomically flat. Figure 6.7 shows the force relaxation curves under 0 nN and +0.5 nN load forces. All the experimental parameters were kept constant compared to the previous experiments on silica surfaces. Due to the atomic flatness the friction force is reduced by one order of magnitude at SA contact. The relaxation of the tip is well described by a single exponential law:

$$\Delta I_x = \Delta I_{max} e^{-t/\tau} \quad (2)$$

Where,  $\Delta I_{max}$  is the maximum lateral signal which is proportional to friction force, and  $\tau$  is the relaxation time. This confirms our hypothesis that the stretched exponential relaxation of slip at SA contact is relevant with the atomic structure of the surface. When the load force becomes larger,  $I_{max}$  also increases. Compared with silica surface, the relaxation time on mica surface is lower.

### 6.3 Conclusion

Using continuous HRH-SA experiments, the onset of the frictional slip between an AFM tip and a silicon surface (with native oxidized layer) is fully described with a sub-angstrom resolution. In the continuous HRH-SA experiments, the sample surface moves stepwise and

the slip behaviour of the contact AFM tip is studied. Three regions are expected during the onset of the frictional slip of the AFM tip, which are ‘stick’, ‘transition’ and ‘repeated slip’ regions. It is demonstrated that these slip behaviours can be described by stretched exponential law at larger twist forces and single exponential law at smaller twist forces. This indicates the existence of multiple length and time scales of the detachment at SA contact, we attribute this to the fact that SA contact can be regarded as multiple-contact of atomic interactions. This indicates the onset of the frictional slip at atomic scale can also be described by the same model as we do at macroscale. This may help to understand the dynamics of the slip at atomic scale, in a more quantitatively and more physically based way.

#### **6.4 Materials and methods**

A chip of about of 1 cm × 1 cm was cut from a (100) Silicon wafer with a native oxide layer of about 2 nm (obtained from Sil’Tronix Silicon Technologies). The silicon chip was firstly rinsed with demi-water and ethanol followed by sonication using ethanol and acetone for 5 min., respectively. Oxygen-plasma treatment of a silicon chip was performed for 1 min at a pressure of 1600 mTorr (XX Pa), using a Harrick plasma cleaner (Anadis Instruments). After plasma treatment, the silicon chip was stored in milli-Q water for at least 24 hours to equilibrate before the experiments started.

All the experiments are performed using the lateral-force mode on a SOLVER NEXT AFM instrument from NT-MDT. The standard LFM probe (PPP-LFMR) was bought from NanoAndMore GmbH, with cantilever length of 215 – 235  $\mu\text{m}$ , width of 40 – 55  $\mu\text{m}$ , and a tip height of 10 – 15  $\mu\text{m}$ .

#### **6.5 References**

- [1] H. Olsson, K. J. Åström, C. C. De Wit, M. Gäfvert, P. Lischinsky, *European journal of control* 1998, 4, 176.
- [2] Z. Olami, H. J. S. Feder, K. Christensen, *Physical Review Letters* 1992, 68, 1244; W. Brace, J. Byerlee, *science* 1966, 153, 990; P. Bak, C. Tang, *Journal of Geophysical Research: Solid Earth* 1989, 94, 15635.
- [3] I. M. Hutchings, P. Shipway, 1992; G. Stachowiak, A. W. Batchelor, *Engineering tribology*, Butterworth-Heinemann, 2013.

- [4] A. Rosakis, O. Samudrala, D. Coker, *Science* 1999, 284, 1337; B. Budiansky, J. W. Hutchinson, A. G. Evans, *Journal of the Mechanics and Physics of Solids* 1986, 34, 167.
- [5] S. M. Rubinstein, G. Cohen, J. Fineberg, *Nature* 2004, 430, 1005.
- [6] O. Ben-David, G. Cohen, J. Fineberg, *Science* 2010, 330, 211.
- [7] M. Reguzzoni, M. Ferrario, S. Zapperi, M. C. Righi, *Proceedings of the National Academy of Sciences* 2010, 107, 1311.
- [8] O. Braun, I. Barel, M. Urbakh, *Physical review letters* 2009, 103, 194301.
- [9] E. Bayart, I. Svetlizky, J. Fineberg, *Nature Physics* 2016, 12, 166.
- [10] Q. Li, T. E. Tullis, D. Goldsby, R. W. Carpick, *Nature* 2011, 480, 233.
- [11] Y. Liu, I. Szlufarska, *Physical review letters* 2012, 109, 186102.
- [12] Wikipedia; J. Klafter, M. F. Shlesinger, *Proceedings of the National Academy of Sciences* 1986, 83, 848.
- [13] W. Knobon, N. Besseling, M. C. Stuart, *Physical review letters* 2006, 97, 068301.
- [14] Wikipedia, Stretched exponential function. doi:[https://en.wikipedia.org/wiki/Stretched\\_exponential\\_function](https://en.wikipedia.org/wiki/Stretched_exponential_function) 2017.
- [15] D. Johnston, *Stretched Exponential Relaxation*. 2006.

## Summary

Atomic Force Microscopy (AFM) can not only image the topography of surfaces at atomic resolution, but can also measure accurately the different interaction forces, like repulsive, adhesive and lateral existing between an AFM tip and the sample surface. Based on AFM, various extended techniques have been developed such as colloidal probe AFM, single molecule AFM, bio-AFM, Kelvin probe AFM and lateral force AFM (LFM). Together, these make AFM a powerful tool to study the properties of surfaces and interfaces, which is of great importance for many different disciplines, e.g. surface chemistry, polymer chemistry and physics, solid-state physics, cell biology and medicine.

In this thesis, we performed various fundamental studies focused on the surface and interface of silicon/silicon oxide (silica) and graphene oxide (GO), both are important materials in science and technology. Silicon surfaces with its native silicon oxide layer is a widely used also a model surface. GO is an important 2D material, which has multi-faces and applications, e.g. surfactant, diblock copolymer, colloids.

Chapter 2 reports a new method to determine experimentally the Hamaker constant between GO and silica. This constant quantifies the strength of the mutual Van der Waals (VdWs) forces. Atomically thin 2D GO was used as nanometre-scale spacer with sub-nm accuracy to control the interfacial distance between GO and silica. However, using such a physical spacer introduces additional interactions, for instance, electrostatic forces and capillary forces, obscuring the interactions of interest, which is the VdWs force between GO and AFM tip. We demonstrate that these contributions can be completely eliminated by effectively mimicking the use of a 'vacuum spacer'. Vacuum acts as a spacer and only VdWs forces between GO and silica contributes to the interaction force.

Chapter 3 describes a novel method to fabricate porous graphene oxide (PGO) from GO exposure to oxygen air plasma. The GO material comprises of graphene domains and the more polar, hydroxylated domains. When exposed to oxygen air plasma, the different GO domains show different reactivity. This method is  $10^2$  - $10^3$  more fast than thermal etching procedures. The development of the porosity with exposure time was studied by AFM. Surprisingly, we found that the development of pores is influenced by the tapping mode AFM scanning using a Si tip. It stalls the growth of pores upon further plasma exposure at a level that coincides with the fraction of  $sp^2$  carbons (corresponds to the

graphene domains) in the GO starting material. We have demonstrated here for the first time that AFM is used as a tool for local mechano-chemistry.

In Chapter 4 we proposed and demonstrated a novel method to calibrate accurately the lateral force mode AFM (LFM). LFM, which is able to detect the ultra-small lateral forces  $O$  (in the nN to  $\mu$ N range) between the AFM tip and the sample surface. Calibration in LFM is not obvious. Current methods are laborious, may damage the probe or modifications of the probe are needed. This hampers the measurement of accurate absolute values for the lateral forces. In our method, no damage or modification of the AFM probe is involved and only a clean silicon wafer is needed. It readily works on typical commercially available AFM systems.

In Chapter 5 the results from LFM force experiments are described demonstrating that GO surfaces can be effectively lubricated by only a few layer of water molecules. The hydrophilicity, its atomically flat structure and non-swelling nature, enables GO to bind a 2-4 nm thick hydration film allowing for efficient lubrication by water. This rather unique property may certainly lead to new applications of GO, such as aqueous nano-mechanical devices and surface coatings in biomedical systems, where lubrication domains and lubricating additives are often prohibited.

In Chapter 6, using continuous HRH-SA experiments, the onset of the frictional slip between an AFM tip and a silicon surface (with native oxidized layer) is fully described with a sub-angstrom resolution. In the continuous HRH-SA experiments, the sample surface moves stepwise and the slip behaviour of the contact AFM tip is studied. Three regions are expected during the onset of the frictional slip of the AFM tip, which are 'stick', 'transition' and 'repeated slip' regions. It is demonstrated that these slip behaviours can be described by stretched exponential law at larger twist forces and single exponential law at smaller twist forces. This indicates the existence of multiple length and time scales of the detachment at SA contact, we attribute this to the fact that SA contact can be regarded as multiple-contact of atomic interactions. This indicates the onset of the frictional slip at atomic scale can also be described by the same model as we do at macroscale. This may help to understand the dynamics of the slip at atomic scale, in a more quantitatively and more physically based way.

## Samenvatting

Atomaire Kracht Microscopie (AFM) kan niet alleen de topografie van oppervlakken meten met atomaire resolutie, maar kan ook nauwkeurig de verschillende interactiekrachten meten, zoals respulsieve, adhesieve en laterale krachten die bestaan tussen de AFM tip en het sample oppervlak. Gebaseerd op AFM zijn diverse toegevoegde technieken ontwikkeld, zoals colloïd tip AFM, AFM op een enkel molecuul, bio-AFM, Kelvin Probe AFM en laterale kracht AFM (LFM). Samen maken deze technieken AFM tot een krachtig instrument om de eigenschappen van oppervlakken te bestuderen, wat belangrijk is voor veel verschillende disciplines, zoals oppervlaktechemie, polymeerchemie en –natuurkunde, solid state natuurkunde, celbiologie en medische wetenschap.

In deze dissertatie hebben we verschillende fundamentele studies uitgevoerd met een focus op het oppervlak en grensvlak van silicium/siliciumoxide (silica) en grafeenoxide (GO). Beide zijn belangrijke materialen voor wetenschap en technologie. Silicium oppervlakken met hun natuurlijke siliciumoxide laag worden breed toegepast als modeloppervlak. GO is een belangrijke 2D material met verschillende facetten en applicaties zoals surfactanten, diblock copolymeren en colloïden.

Hoofdstuk 2 beschrijft een nieuwe method om experimenteel de Hamaker constant te bepalen tussen GO en silica. Deze constante kwantificeert de sterkte van de gezamenlijke Van der Waals (VdWs) krachten. Atomair dun 2D GO is gebruikt als een nanometer-schaal spacer met sub nanometer nauwkeurigheid om de afstand tussen de oppervlakken van GO en silica te regelen. Echter, als gebruik wordt gemaakt van een fysieke spacer worden meer interacties veroorzaakt, bijvoorbeeld electrostatische krachten en capillairkrachten die zo de interacties verhullen die juist onderzocht worden, zijnde de VdWs krachten tussen GO en de AFM tip. We laten zien dat deze bijdragen compleet kunnen worden geëlimineerd door het effectief namaken van het gebruik van een ‘vacuüm spacer’. Vacuüm akteert als een spacer en alleen VdW krachten tussen GO en silica dragen bij aan de interactiekracht.

Hoofdstuk 3 beschrijft een nieuwe method om poreuze grafeenoxide (PGO) te maken door GO bloot te stellen aan een zuurstof-lucht plasma. Het GO material bestaat uit grafeendomeinen en meer polaire gehydroxyleerde domeinen. Na blootstelling aan een zuurstof-lucht plasma laten de verschillende GO domeinen verschillende reactiviteit zien. Deze method is  $10^2$ - $10^3$  keer sneller dan thermische etsprocessen. De ontwikkeling van de

porositeit als functie van de blootstellingstijd is onderzocht met AFM. Tot onze verassing vonden we dat de ontwikkeling van de poriën wordt beïnvloed door de tapping mode AFM scanning waarbij gebruik wordt gemaakt van een silicium tip. Het hindert de groei van poriën bij verdere blootstelling aan plasma tot een niveau dat het samenvalt met de fractie aan  $sp^2$  koolstof atomen (corresponderend met de grafeendomeinen) in het GO startmateriaal. We hebben hier voor het eerst aangetoond dat AFM is gebruikt als een instrument voor mechano-chemie.

In hoofdstuk 4 stellen wij voor en demonstreren wij een nieuwe methode om de laterale kracht AFM (LFM) methode te calibreren. LFM is in staat de ultrakleine laterale kracht  $O$  te meten (op de nN tot  $\mu$ N schaal) tussen de AFM tip en het sampleoppervlak. Kalibratie in LFM is niet trivial. De bestaande methoden zijn arbeidsintensief, beschadigen mogelijk de tip of tipmodificaties zijn nodig. Dit hinder de meting van nauwkeurige absolute waarden voor de laterale krachten. In onze methode is er geen beschadiging of modificatie nodig en slechts een schone silicium wafer is nodig. Het is meteen te gebruiken op algemeen commercieel verkrijgbare AFM systemen.

In hoofdstuk 5 worden de resultaten beschreven van LFM krachtmetingen die laten zien dat GO oppervlakken effectief gesmeerd kunnen worden door slechts enkele lagen watermoleculen. In welke mate GO hydrofiel is, zijn atomair vlakke structuur en niet zwellende natuur zorgt er voor dat GO een 2 tot 4 nm dikke waterlaag kan binden waardoor het efficiënt kan worden gesmeerd door water. Deze tamelijk unieke eigenschap zal zeker leiden tot nieuwe applicaties voor GO, zoals water gebaseerde nano-mechanische instrumenten en oppervlaktecoatings in biomedische systemen waar domeinen voor smering of toevoegingen voor smering vaak niet worden toegestaan.

In hoofdstuk 6 wordt de aanzet van de frictie-slip tussen een AFM tip en een siliciumoppervlak (met natuurlijke geoxideerde laag) volledig beschreven met sub-angstrom resolutie, gebruik makend van continue HRH-SA experimenten. Bij deze continue HRH-SA experimenten beweegt het sampleoppervlak stapsgewijs waarbij het slipgedrag van de contact AFM tip wordt bestudeerd. Er worden drie regio's verwacht tijdens de aanzet van een frictieslip van de AFM tip, zijnde 'plak', 'transitie' en 'herhaalde slip' regio's. Het is bewezen dat deze slip gedragingen kunnen worden beschreven door oprerekte exponentiële wetten bij grotere torsiekrachten en enkelvoudige exponentiële wetten bij kleinere torsiekrachten. Dit geeft het bestaan aan van meervoudige lengte en

tijdschalen van het loskomen van het SA contact. Wij schrijven dit toe aan het feit dat SA contact kan worden beschouwd als meervoudig contact van atomaire interacties. Dit geeft aan dat de aanzet van de frictieslip op atomaire schaal ook kan worden beschreven door hetzelfde model als we gebruiken bij de macroschaal. Dit helpt mogelijk de dynamica te begrijpen van de slip op atomaire schaal op een meer kwantitatieve en meer natuurkundig gebaseerde manier.





## ACKNOWLEDGEMENTS

- I would like to acknowledge my supervisors Prof. Dr. Ernst J. R. Sudhölter, Prof. S.J. Picken and Dr. N.A.M. Besseling. You gave me the opportunity to work as a PhD researcher and also I learned a lot from all of you, how to think and work as a scientist and collaborate with colleges. Sincere acknowledgement from inside of my heart gives to Klaas, for your guidance and supervision during the four years.
- I thank Dr. A.V. Korobko for helping me with the interpretations of the experimental results. It is really nice to work with you. I thank the kind help and valuable technical support from the technicians in OMI and ASM. Marcel Bus, your expertise with AFM is definitely essential for this thesis, also thank you for help me translate the summary. I am grateful to Duco Bosma for your patience and kind help with the instruments.
- I would like to express my sincere acknowledgement to our collaborators, Dr. Murali Ghatkesar from 3ME, Dr. Danqing Liu and prof.dr. D.J. (Dick) Broer from TU/e.
- I would like to acknowledge all the members of OMI, Aldo, Daniela, Hamid, Laura, Liza, Louis, Lukasz, Mohammad, Naveen, Rajeev, Stijn, Sumit, Wolter and all the master and bachelor students, for creating such a nice working atmosphere, and I will always remember the happy time with you.
- I wish to deeply thank those guys that contribute to my volleyball career in Delft. Bart Boshuizen, my special acknowledgement to you for introducing me to your team, also I am grateful to all these members in HS 12 and HS 10 of Kratos'08.
- My sincerely acknowledgement gives to my Chinese friends in TUDelft, for your help with my research and family. Zhen Liu, Anping Cao, and Zheng Cao from OMI group, I had my best PhD time, when us four were all in the group. Ming Ma and Meixia Shan, we came from the same group in China and we knew each other well very long time ago. Xiaohui Sun, Zihan Tan, Jianping Wang, Jinyu Tang, Runhai Feng, my lovely flatmates, I enjoy all the time we have together. Xiaohui, far more than that, we came together initially and achieved enormously together. Jicheng Feng, Kai Zhang, Wuyuan Zhang and Yunlong Yu, you came here earlier than me and helped me numerously, I highly appreciate that. I am

grateful to my dear friends, Kai Liu, Lei Xie, Min Wang, Quan Pan, Riming Wang, Xinyuan Mao, Yiming Wang, Yixiao Wang and Yujie Zhao.

- I thank my wife, Mei He and our lovely daughter Yunlin Chu. I thank my parents and my elder sister Min Chu for always encouraging me and standing behind me. I love you all.

2017-12

Liangyong Chu(褚良永)

## Curriculum Vitae

**Liangyong Chu**

Born on April 14, 1989

In Shandong, China

2006.9-2010.7

Bachelor of Science in Materials Physics, College of Science, China University of Petroleum, Qingdao city, China. Thesis title: *Molecular Dynamics simulation of Graphene/Silicon Nanowires composites.*

2010.9-2013.7

Master of Science in Applied Physics, College of Science, China University of Petroleum, Qingdao city, China. Thesis title: *Fabrication of Graphene/ poly (vinylidene fluoride) composites with high dielectric properties.*

2013.9-2017.9

PhD candidate in Organic Materials & Interface (OMI) group, Chemical Engineering, Delft

## LIST OF PUBLICATIONS

### Publications

1. **Chu, L.;** Korobko, A. V.; Cao, A.; Sachdeva, S.; Liu, Z.; de Smet, L. C.; Sudhölter, E. J.; Picken, S. J.; Besseling, N. A. M, Mimicking an Atomically Thin “Vacuum Spacer” to Measure the Hamaker Constant between Graphene Oxide and Silica. *Advanced Materials Interfaces* 2017.
2. Guan, Q.; Norder, B.; **Chu, L.;** Besseling, N. A. M; Picken, S. J.; Dingemans, T. J., All-Aromatic (AB) n-Multiblock Copolymers via Simple One-Step Melt Condensation Chemistry. *Macromolecules* 2016, 49, 8549-8562.
3. **Chu, L.;** Korobko, A. V.; Bus, M.; Besseling, N. A. M, Fast and Controlled Fabrication of Porous Graphene Oxide: Application of AFM Tapping for Mechano-chemistry, *Manuscript submitted*.
4. **Chu, L.;** Bus, M.; Besseling, N. A. M, Calibrating lateral force AFM and measurement of the lateral spring constant, *Manuscript submitted*.
5. **Chu, L.;** Korobko, A. V.; Besseling, N. A. M, AFM study of lubrication by water of the Graphene oxide surface, *Manuscript submitted*.
6. **Chu, L.;** Korobko, A. V.; Besseling, N. A. M, Force relaxation of the onset of slip at single asperity contact, *Manuscript submitted*.
7. **Chu, L.;** Xue, Q.; Sun, J.; Xia, F.; Xing, W.; Xia, D.; Dong, M., Porous graphene sandwich/poly (vinylidene fluoride) composites with high dielectric properties. *Composites Science and Technology* 2013, 86, 70-75.
8. **Chu, L.;** Xue, Q.; Zhang, T.; Ling, C., Fabrication of carbon nanoscrolls from monolayer graphene controlled by p-doped silicon nanowires: a md simulation study. *The Journal of Physical Chemistry C* 2011, 115, 15217-15224.
9. Lei, T.; Xue, Q.; **Chu, L.;** Han, Z.; Sun, J.; Xia, F.; Zhang, Z.; Guo, Q., Excellent dielectric properties of polymer composites based on core-shell structured carbon/silica nanohybrid. *Applied Physics Letters* 2013, 103, 012902.
10. Ling, C.; Xue, Q.; **Chu, L.;** Jing, N.; Zhou, X., Radial collapse of carbon nanotubes without and with Stone–Wales defects under hydrostatic pressure. *RSC Advances* 2012, 2, 12182-12189.

11. Sun, J.; Xue, Q.; **Chu, L.**; Guo, Q.; Lei, T.; Xia, F.; Zhang, Z., Ultra-high dielectric constant of poly (vinylidene fluoride) composites filled with hydroxyl modified graphite powders. *Polymer Composites* 2016, 37, 327-333.
12. Xia, D.; Xue, Q.; Zhang, T.; **Chu, L.**; Dong, M., Carbon/Silicon Heterojunction Formed by Inserting Carbon Nanotubes into Silicon Nanotubes: Molecular Dynamics Simulations. *The Journal of Physical Chemistry C* 2012, 116, 23181-23187.
13. Xue, Q.; Jing, N.; **Chu, L.**; Ling, C.; Zhang, H., Release of encapsulated molecules from carbon nanotubes using a displacing method: a MD simulation study. *RSC Advances* 2012, 2, 6913-6920.